Imperial College London

Ultrafast Dynamics of Relativistic Laser Plasma Interactions

Matthew J. V. Streeter

September 2013

Submitted in partial fulfilment of the requirements for the degree of
Doctor of Philosophy of Imperial College London

Department of Physics
Imperial College London
Prince Consort Road
London SW7 2BZ

Declaration

I hereby certify that the material of this thesis, which I now submit for the award of Doctor of Philosophy, is entirely my own work unless otherwise cited or acknowledged within the body of text.

Matthew James Victor Streeter

Monday 24$^{\text{th}}$ March, 2014

Copyright

The copyright of this thesis rests with the author and is made available under a Creative Commons Attribution Non-Commercial No Derivatives licence. Researchers are free to copy, distribute or transmit the thesis on the condition that they attribute it, that they do not use it for commercial purposes and that they do not alter, transform or build upon it. For any reuse or redistribution, researchers must make clear to others the licence terms of this work

Role of the Author

The experiments that are described in this thesis were carried out by a team of scientists, students and technical staff using facilities established by the Central Laser Facility at the Rutherford Appleton Laboratory in Oxfordshire, UK. The author was involved in the planning, set-up and analysis phases of each experiment, with particular focus on diagnostics which lead to the results presented in this thesis.

All the data and analysis presented is the work of the author except for target transmissivity and forward harmonic data, which was provided by a colleague. The author also performed and analysed the PIC simulations that are included in chapters 4-6, making use of the OSIRIS and EPOCH codes.

Acknowledgements

The nature of the work carried out for this thesis is very collaborative and could not have been successful without the huge efforts of some wonderful people at Imperial College and at other institutions around the world. Particular thanks are due to my supervisor, Professor Zulfikar Najmudin, for the constant encouragement and expert guidance that has elevated the standard of my work far beyond what it would otherwise have been. Equally crucial have been the contributions of Stuart Mangles and Jörg Schreiber who have been constant sources of inspiration and have helped to make sense of all the experiments. Also, thank you to Bucker Dangor and Peter Norreys for always asking difficult questions and providing words of wisdom.

Day to day life on experiments has only been possible due to the wonderful people I have had the pleasure of working with. These include, but are not restricted to, Nick, Stefan, Sabrina, Nelson, George, Kris, Juffalo, Jon, Mike, Andreas, Hiro, Digger, Tom, Dan, Steve, Peta, Nicola, Rob(s) plus too many to more to mention!

Life at Imperial College has been a pleasure, and Plasma Football, pub evenings (and lunchtimes), tea breaks and days in the office has always felt like a great way to spend time. Thanks to my office mates for the relaxed atmosphere and in particular to Ed for co-inventing FROGed!

Thank you Charlie for agreeing to the 'bad plan' and for generally being wonderful and making my life immeasurably richer. Also, thank you for rooting out hundreds of typos and incomprehensible sentences for me!

I would like to dedicate this thesis to my family for their incredible strength and always being there to teach me how to be a better person. Also for my father. I think about you always.

Abstract

This thesis documents the experimental and theoretical investigation of laser pulse evolution in relativistic laser-plasma interactions for plasma-wakefield acceleration and ion acceleration experiments.

Power amplification of the Astra Gemini laser in a plasma was observed, with the compression of an initially 55 fs, 180 TW pulse down to 14 fs, with a peak power of 320 TW. This was achieved in a laser-driven plasma wakefield operating just below the self-injection threshold density for a propagation distance of 15 mm. Self-guiding of the laser pulse was observed, while pulse depletion was characterised as a function of density and propagation distance, showing that the pulse evolution scales equally with both. These measurements displayed good agreement with a depletion model based on pulse front etching. Particle-in-cell simulations were seen to closely reproduce the experimental results, which were concluded to be predominantly dependent on the longitudinal properties of the laser and wakefield. The simulations also revealed a new wakefield instability that is driven by the far red-shifted component of the laser pulse.

In the case of high-contrast solid-density interactions, oscillations of the front surface of the plasma were seen to result in the generation of the second harmonic of the driving laser for a p-polarised interaction. Conversion efficiencies of $22(\pm 8)\%$ into the second harmonic were measured, while the total plasma reflectivity into the first and second harmonics remained relatively constant at 65% over the intensity range of 10^{17}–10^{21} Wcm^{-2}.

For normal incidence interactions with sub-micron thickness foils, the cycle-averaged surface motion was measured using a FROG diagnostic. Targets of a few nanometers in thickness underwent an acceleration away from the laser, but the measured surface velocities did not match the expected hole-boring velocities or the measured ion energies, due to the thermal expansion of the plasma. 2D simulations revealed that studying target motion in this way is affected by the scale length of the plasma and photon acceleration that can occur in the tenuous plasma in front of the laser-reflecting surface.

Contents

List of Figures

List of Tables

Chapter 1

Introduction

The interaction of ultra-high intensity lasers with matter is characterised by huge energy densities for a very short period of time. The extreme states of matter achieved in these interactions do not occur anywhere else on earth, but are rather more like the interior of stars. This makes it possible to study astrophysical phenomena in a laboratory, adding new insight to phenomena that, otherwise, are either only observable with telescopes or not at all. In recreating these conditions, it is also possible to trigger fusion reactions, such as those that power the sun. Tailoring these interactions in other ways has lead to potential applications such as,

- Laser-driven particle accelerators [Esarey09],
- X-ray/gamma sources [Gibbon96, Corde13],
- Probing the behaviour of hot-dense matter [Koenig95, Da Silva97].

The development of these applications requires a great amount of experimental, theoretical and computation work to understand and control the critical processes. In particular, accurate and meaningful experimental diagnostics are necessary to provide theoretical insight and test physical predictions.

The main focus of this thesis is the diagnosis of laser-driven particle accelerators by monitoring the effects of the interaction on the driving laser pulse itself. This can provide crucial information about the time-resolved dynamics of the interactions, which in turn improves the understanding of how to control and optimise the acceleration mechanisms. Diagnosis is a particular challenge of these interactions, because of the ultrafast timescales involved. In addition, the interaction can modify the laser in ways that are useful for secondary applications, including changes to the laser spectrum, which allows further interactions with different laser wavelengths, and the temporal compression of the laser, enabling interactions with higher peak-power pulses.

1.1 Particle accelerators

Charged particles can be accelerated to high energies by the application of strong electric fields. Either static or oscillating fields can be used and the geometry of the accelerator can be linear or circular in nature. Circular accelerators, such as cyclotrons and synchrotrons, benefit from having the particles traverse the same accelerating regions many times, picking up more energy with each circuit. However, forcing charged particles to travel in circular paths causes them to lose some of their energy in the form of synchrotron radiation [Elder47]. This is of particular importance to electron accelerators, as they radiate a large amount of energy at comparably modest energies. Protons, and heavier particles, radiate less for a given energy, and so they have become favoured for particle accelerators designed to explore high energy particle physics. However, due to the greater mass of these particles, they are much harder to steer at high energies. Therefore, to increase the maximum achievable energy of the particles, bigger and bigger machines must be built, currently culminating in the 26.6 km diameter Large Hadron Collider (LHC) at CERN, which accelerates protons up to 8 TeV. Linear accelerators (linacs) are also used, but as the acceleration length is fixed by the length of the machine, the resultant particle energies are limited by the accelerating field strength and the length of the accelerator. The longest current linac, the Stanford Linear Accelerator at the SLAC Linear Accelerator Laboratory, is 3.2 km in length and can achieve electron energies of $\sim$ 50 GeV.

Particle accelerators are used for a huge range of applications. These include particle physics, such as the recent high profile search for the Higgs boson [ATLAS12], particle scattering experiments for atomic physics [Rutherford11], x-ray generation for studying the structure of semi-conductors [Fewster03] and bio-medical imaging [Momose96, Neutze00], and proton beam cancer therapy [Levin05]. All these applications have different requirements for the particle beam, in terms of the energy of the particles, the number of particles, the duration of the particle bunch, the transverse size of the particle bunch or the quality of the spectrum, but generally these requirements are only met by large building-scale machines which are very costly to build and operate. The size and expense of these machines also limit their accessibility in terms of how much beam time is available to teams that wish to use them, but also in transport costs. A particular example of this is the use of x-ray sources to scan images buried beneath the surface of expensive paintings. This was done in 2008 to reveal an older painting beneath van Gogh's 'Patch of grass' (see figure **1.1**) at the Doris III synchrotron radiation source at DESY in Hamburg [Dik08]. Although using the machine itself was expensive, it also caused considerable problems and anxiety transporting the priceless piece of art from the Netherlands to the accelerator. A huge reduction in the scale of such radiation sources would be required to enable them to be located in the basements of large museums, but this would allow many more paintings to be analysed at a fraction of the cost.

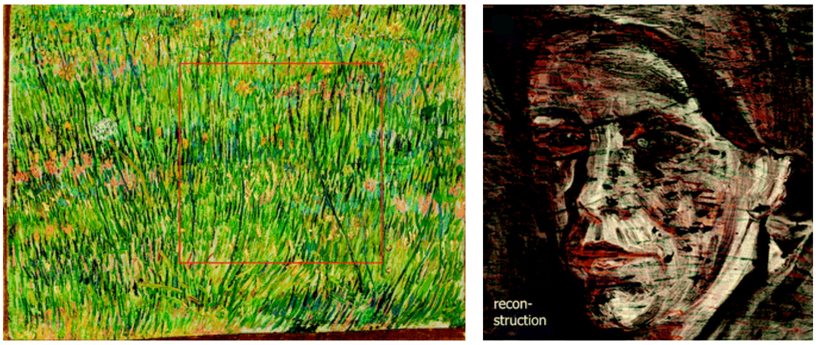

(a) (b)

Figure 1.1: (a) Vincent van Gogh's "Patch of grass" and (b) a computer reconstruction of an older painting hidden beneath. The data for the reconstruction was taken using x-ray fluorescence at the DORIS III synchrotron at DESY. Adapted with permission from [Dik08]. Copyright 2008 American Chemical Society.

To achieve higher particle energies, accelerators must increase in size, or the accelerating field must be increased from the current level of about 20 MVm^{-1}. Therefore, research to develop acceleration mechanisms that can increase the accelerating gradients and reduce the size and material cost of accelerators will allow great advances to be made and allow more widespread use of the machines. Conventional methods of generating these fields are limited by the breakdown of the materials that make up the accelerator. This breakdown creates a plasma, by ionising the cavity walls and the near-vacuum inside the cavity. This adversely affects the acceleration process and also damages the machine. However, an accelerator designed to work as a plasma could overcome this limit and allow much higher accelerating forces.

1.2 Plasma

Plasma is created when the electrons gain enough energy to escape the force binding them to the atoms. Once freed, the electrons and ions form a 'soup' of charged particles which are able to move around independently of each other but still influence each other via the electromagnetic force. Applying an external field to a plasma will also influence the motion of these particles and can set up charge imbalances. If the field is then removed the electrostatic force will attract the opposite charges together to regain neutrality. However, at the point at which the particles return to a uniform charge neutral distribution, the particles inevitably have some velocity and overshoot the equilibrium position and begin to oscillate around it. This leads to charge density waves which propagate through the plasma, driven by the electromagnetic interaction of the particles. As the electrons are much less massive than the atomic nuclei, they move much more readily and dictate the changes in the plasma. The slower ions are then coerced into following the electrons by the attractive electric force.

Inducing large perturbations to the plasma density with an external field can set up large fields within the plasma. These fields can then be used to accelerate charged particles to high energies. A very effective way of achieving this is to use a laser pulse, focused to a high energy density, which constitutes an intense electromagnetic field. Lasers also offer a way to create the plasma, as the fields are capable of rapidly ionising any material. Emission from a laser ionised plasma can be see in figure **1.2**.

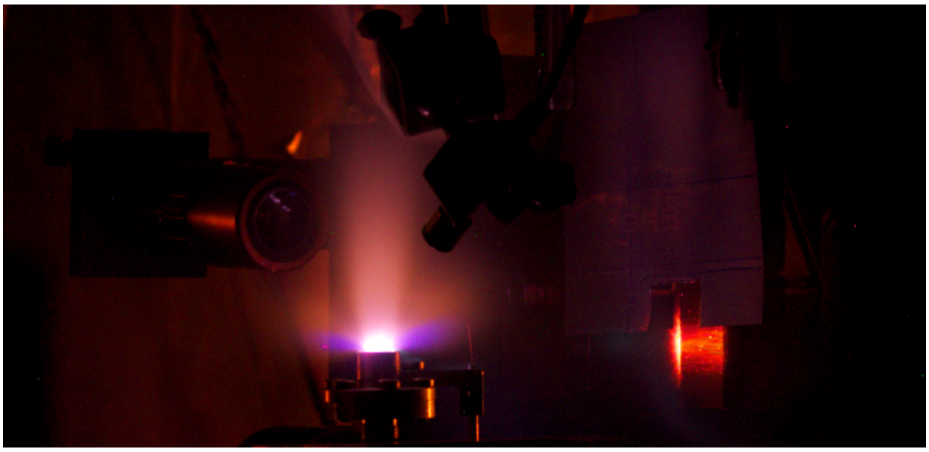

Figure 1.2: Photo of a plume of helium gas at the moment a high-intensity laser pulse is fired into it from left to right. The bright emission near the centre is emission from a plasma. Most of the laser energy continues through the plasma and is seen scattering off a magnet towards the right of the image.

1.3 Lasers

The development of lasers has been driven by scientific interest in compressing as much energy as possible into as small a volume as possible. This means not only being able to focus the laser light to a small spot, but also requires that it has a short pulse duration. By squeezing all the energy of the laser into a pulse that is a tiny fraction of a second in duration, the laser is capable of producing astounding peak powers. A university scale laser in 2013 may have just a few joules of energy in each pulse (the energy gained by a bag of flour dropping from the kitchen table). But with a pulse length of 50 femtoseconds (less time than it takes light to travel the thickness of this paper), the peak power is of the order of 100 TW. By comparison, a modern coal fired power station can produce 1–4 GW, but does so almost constantly.

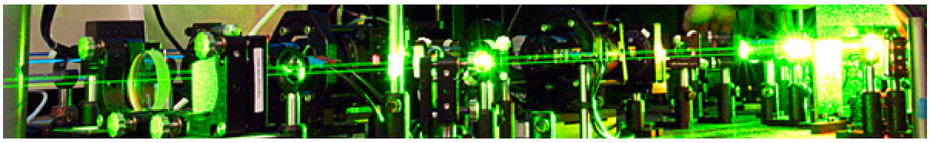

Figure 1.3: Photo of part of the Astra Gemini laser system.

With highly-focusable, massively-powerful lasers pulses, extremely high intensities can be reached. This is one of the main characteristics in any laser-matter interaction as it determines the strength of the electromagnetic field and, therefore which processes occur. When the electric field of the focused laser becomes equivalent to the interatomic bonds of a material, it modifies the material properties as it propagates. This can have an effect on the laser pulse, as the refractive index of the material is temporally and spatially varying. This is the basis for the field of nonlinear optics and leads to processes such as frequency mixing (generating new wavelengths), self-focusing and self-phase modulation [Agrawal01]. Once the laser field becomes comparable to the binding energy between the electron and the atomic nucleus, rapid ionisation of the material occurs. The resultant plasma can then absorb laser energy via the interaction of the electromagnetic field with the freed electrons. Once the laser intensity is large enough to accelerate electrons to an appreciable fraction of the speed of light then the system becomes relativistic, which further changes the nature of the interaction. Such lasers, referred to as having relativistic intensities, are now being used to investigate laser-driven plasma accelerators, which have the potential to improve upon existing particle accelerator technology and allow the reduction in size and cost of accelerators, as well as potentially leading to higher energy machines in the future.

1.4 Laser-driven plasma wakefield accelerator

The ideal particle accelerator has a large longitudinal electric field which co-moves with the particle. Therefore, the accelerating structure must move at close to the vacuum speed of light in order to keep up with a relativistic electron. This is achieved in conventional accelerators by using oscillating electric fields that are matched to the particle trajectories, such that the particles always experience an accelerating force. However, an intense laser propagating in a tenuous plasma naturally generates a longitudinal electric field which moves at close to the speed of light, therefore ideally suited to the acceleration of relativistic particles.

The accelerating structure, pictured in figure **1.4**, is created by the ponderomotive force of the laser. This force expels electrons in a plasma from regions of high laser intensity, resulting in the formation of an ion cavity at the centre of the laser pulse. After the laser has propagated onwards, the repulsive force is no longer present and the electrostatic force attracts the expelled electrons back to the centre of the ion cavity. As the electrons regain their equilibrium positions, they overshoot and then continue to oscillate in the wake of the laser. Along the central axis of the laser, the electron density varies above and below

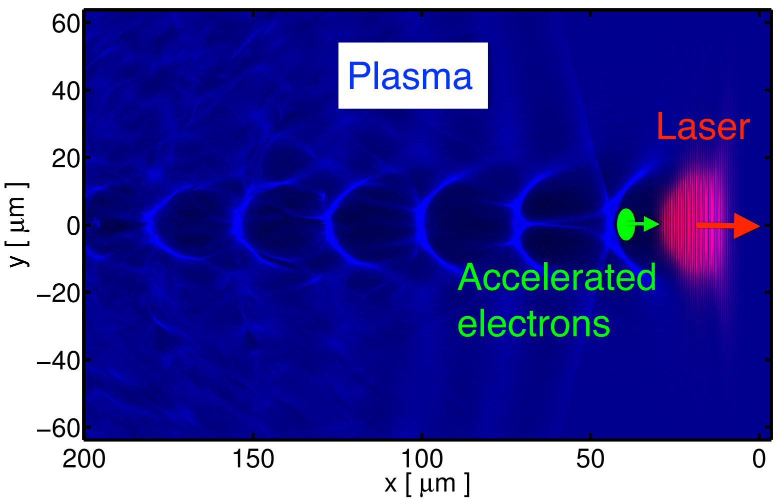

Figure 1.4: An image of a plasma wave set up by the passage of an intense laser pulse. The wave is able to accelerate electrons in the direction in the laser propagation direction.

the background density, generating longitudinal electrostatic fields. Any electrons in the rear half of an ion cavity will experience a forward acceleration, and if they are moving forward at near the speed of light they will keep pace with the laser and continue to be accelerated as long as the accelerating structure is maintained. The accelerating fields can be in excess of 100 GVm^{-1}, more than 1000 times larger than achievable by conventional particle accelerator technology. With the successful application of a plasma accelerator, the electron energy of a kilometer-scale linac could be achieved in a meter-scale plasma.

This mechanism of electron acceleration was first proposed in 1979 by Tajima and Dawson [Tajima79] and was then experimentally demonstrated in 1993 by Clayton et al. [Clayton93]. The first experiments relied on the beating of two laser pulses of different frequencies together to generate the plasma wave, accelerating externally injected electron beams [Joshi84, Clayton93, Everett94]. With the development of chirped pulse amplification in lasers (CPA) [Strickland85], higher intensities ($> 10^{18}$ W cm^2) and shorter pulses (< 1 ps) allowed for the resonant generation of plasma waves [Andreev92] of sufficient strength to accelerate electrons from the plasma itself [Modena95]. More recent experimental work has demonstrated acceleration of electrons with low energy spreads ($<$ 3%) [Mangles04, Geddes04, Faure04] and GeV particle energies [Karsch07, Kneip09, Clayton10, Lu11].

Several physical challenges must be overcome for a practical meter-scale laser-driven plasma wakefield to be constructed. Firstly, to achieve acceleration lengths on the order of a meter, the laser must remain focused over this distance. Typically, a laser will diverge over a millimetre of propagation, so some mechanism of channelling the laser must be developed. Such a mechanism will inevitably be based on 'plasma-optics' as no other material can exist at such high laser intensities. This can be achieved by creating a transverse density profile, such as in a capillary [Zigler96, Butler02, Osterhoff08, Rowlands-Rees08] or pre-expanded ion channel [Geddes05], or by using the non-linear optical properties of the laser, i.e. self-focusing due to the radial intensity profile of the laser [Sprangle92]. Also, although the accelerating structure is travelling at very close to the speed of light, eventually the particle will begin to overtake the laser and move out of the accelerating region of the wakefield. This is known as dephasing and limits the maximum attainable electron energy. However, this may be overcome by fine tuning the plasma density profile [Pukhov08] or by using multiple stages [Lu07]. Additionally, the acceleration length is limited by the depletion of the laser energy, as it generates the plasma wakefield. Therefore, minimising the rate of depletion is important to maximising the accelerated electron energy.

As well as generating an electron beam, plasma wakefields can also cause electron beams to oscillate, producing x-ray radiation. This is known as betatron radiation [Rousse04, Kneip08], and is capable of producing high quality x-ray images due to the small size of the source and short pulse duration.

1.5 Solid target interactions

Solid density plasmas are opaque to visible/infra-red laser wavelengths and so when a laser interacts with an initially solid target, a large amount of energy is reflected. At the laser-plasma boundary, energy is absorbed by electrons via the electromagnetic field of the laser. These highly energetic electrons expand away from the heavier ions, and electrostatic fields are set up, which subsequently accelerate the ions. Some electrons can become relativistic and escape the plasma but are generally emitted in all directions and so are not comparable to conventional electron beam sources. However, depending on the target geometry, the ions can be emitted in a more beam-like profile. For a flat target, the direction of the accelerating field is mostly away from the plane of the target, resulting in front and rear surface ion beams being generated [Clark00, Snavely00, Wilks01]. The radiation pressure of the laser may also drive an electrostatic shock into the target which is also capable of producing ion beams in the laser-forward direction [Wilks92, Silva04, Wei04, Gibbon05a, Macchi05, Palmer11, Haberberger11]. For ultra-thin targets it is even possible for the laser to begin to push the entire target, like a light-sail [Marx66], resulting in a narrow energy spread [Esirkepov04, Robinson08]. Figure **1.5** illustrates the interaction of a laser with a thin foil target, resulting in an ion beam accelerated predominantly in the laser propagation direction.

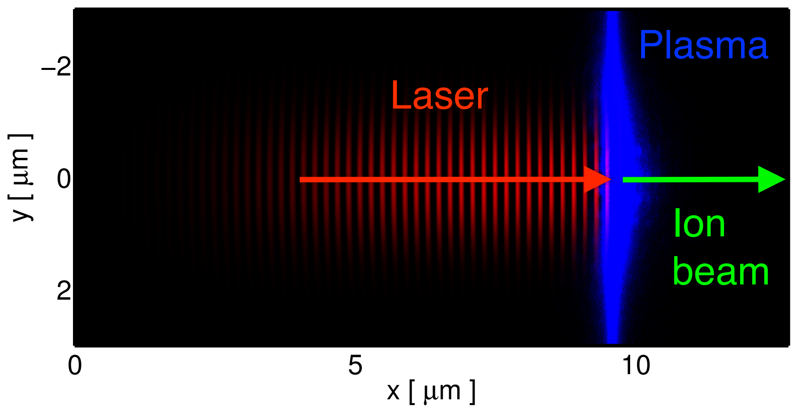

Figure 1.5: An intense laser interacting with a thin foil target. An ion beam can be generated in the forward direction.

Solid target interactions can also be used to generate harmonics of the driving beam. This can occur as the laser field sets up an oscillating electron current on the target surface which couples to the electromagnetic oscillations to generate new frequencies in the reflected pulse. This is a potentially useful source of short pulses of high-frequency light [Giulietti89, Linde95, Gibbon96, Lichters96, Norreys96, Plaja98, Tarasevitch00] and also a useful diagnostic of the target conditions.

1.6 Diagnosis of laser-plasma interaction dynamics

By measuring the effect of a laser-plasma interaction on the driving laser pulse, it is possible to diagnose some of the interaction properties. The laser pulse energy, spectrum, and spatial and temporal profiles can all be modified by the plasma properties, and therefore serve as useful diagnostics. For laser-wakefield experiments, the longitudinal refractive index profile of the plasma modifies the pulse power profile and spectrum. With a good understanding of these processes, characterising the transmitted laser can be used to reveal the structure of the wakefield. Also, as laser depletion limits the maximum possible electron energy, it is important to determine how the laser energy absorption depends on plasma density and propagation distance. This, combined with a measurement of the guided laser spot size, determines whether a large laser intensity has been maintained throughout the interaction length.

For solid target interactions, the reflected laser contains information of the laser-plasma boundary dynamics. Oscillations on the front surface, driven by the laser field, result in spectral modification of the reflected laser pulse, leading to harmonic generation. This reflecting surface can also move in a non-oscillatory manner, due to the radiation pressure of the laser and the thermal expansion of the plasma, causing a Doppler shift to be observed in the reflected laser pulse. Therefore, measurement of the reflected laser spectrum as a function of time can reveal the dynamics of the laser plasma interaction.

1.7 Thesis outline

This thesis contains, experimental, theoretical and computational exploration of high-intensity, ultra-short-pulse laser plasma interactions with tenuous and solid density plasmas. Chapters 2 and 3 contain the theoretical background and research methods relevant to the work detailed in chapters 4–6. Chapter 7 summarises the main results and explores some ideas for future work which could build on this research.

The three chapters containing the experimental work of this thesis are:

4. **Non-Linear Plasma Optics in a GeV Laser Wakefield Accelerator:** The laser pulse evolution in a laser-driven wakefield accelerator is studied through diagnosis of the transmitted laser pulse, spatially and temporally.

5. **Reflectivity of Relativistic Plasma Surfaces and Second Harmonic Generation:** The fundamental and second harmonic energy fractions are measured in the laser pulse after reflection from a solid-density plasma. These results are compared to theoretical models and computer simulations to reveal the surface dynamics of the interactions.

6. **Temporally Resolved Measurements of the Laser-Plasma Boundary Motion in Solid-Density Plasma Interactions:** The reflected laser pulse is used to characterise the motion of the laser-plasma boundary in the interaction of laser pulses with nanometer-scale targets.

Chapter 2

Theory

2.1 Lasers

The most powerful lasers are capable of producing > 100 TW pulses, focusable to intensities $> 10^{20}$ Wcm^{-2}. Such enormous intensities result in huge electric ($\mathbf{E}$) and magnetic ($\mathbf{B}$) fields, as quantified by the Poynting vector, which in a vacuum is

$$\mathbf{S} = \frac{1}{\mu_0}\mathbf{E} \times \mathbf{B} \ , \tag{2.1.1}$$

where μ_0 is the permeability of free-space. The magnitude of the time averaged Poynting vector $|\langle \mathbf{S} \rangle|$ is equivalent to the intensity. For an infinite plane wave propagating in the $\hat{\mathbf{k}}$ direction, with an angular frequency of ω_0 and an electric field amplitude of E_0, the electromagnetic fields and the Poynting vector at a fixed point are,

$$\mathbf{E} = \hat{\mathbf{i}}\, E_0 \sin(\omega_0 t) \ , \quad \mathbf{B} = \hat{\mathbf{j}}\, \frac{E_0}{c} \sin(\omega_0 t) \ , \quad \mathbf{S} = \hat{\mathbf{k}}\, c\epsilon_0 E_0^2 \sin^2(\omega_0 t) \ ,$$

where t is time, c is the speed of light in a vacuum, ϵ_0 is the permittivity of free-space and $\hat{\mathbf{i}}$, $\hat{\mathbf{j}}$ and $\hat{\mathbf{k}}$ are unit vectors in the three spatial directions. Therefore,

$$I = |\langle \mathbf{S} \rangle| = \begin{cases} c\epsilon_0 E_0^2/2 & \text{Linear polarisation,} \\ c\epsilon_0 E_0^2 & \text{Circular polarisation.} \end{cases} \tag{2.1.2}$$

For intensities $I > 10^{20}$ W/cm^2, the peak electric field can exceed 10^{14} Vm^{-1}, which rapidly ionises any matter in the focal region and accelerates the freed electrons to relativistic velocities. An electron (mass m_e, charge e and velocity $\mathbf{v}$) in the laser electromagnetic field experiences the Lorentz force as,

$$\frac{\mathrm{d}\mathbf{p}}{\mathrm{d}t} = -e\left(\mathbf{E} + \mathbf{v} \times \mathbf{B}\right) \ ,$$

where $\mathbf{p}$ is the electron momentum. Assuming $|\mathbf{v}| \ll c$, the velocity of the electron is,

$$\gamma m_e v = \frac{eE_0}{\omega_0}\cos(\omega_0 t) + p_0 \ ,$$

where γ is the Lorentz factor and p_0 is a constant of integration, taken to be some initial momentum of the electron. The quantity $a_0 = eE_0/(m_e\omega_0 c)$ is known as the normalised vector potential. For $a_0 \geq 1$, the electron quiver motion becomes relativistic and so the assumption $|\mathbf{v}| \ll c$ is not valid.

2.1.1 Pulse shape and phase

The time-varying electric field of a linearly polarised laser pulse can be written down as the product of the intensity envelope and the rapidly oscillating field component as,

$$E(t) = \sqrt{\frac{I(t)}{c\epsilon_0}}\exp\left[i(\omega_0 t + \Phi(t))\right] \ , \tag{2.1.3}$$

where $I(t)$ is the intensity of the laser pulse as a function of time, i is the imaginary unit, ω_0 is the angular frequency of the laser, and $\Phi(t)$ is the additional phase term which describes how the rapid oscillations vary in time. The instantaneous frequency of the pulse is given by,

$$\omega(t) = \omega_0 + \frac{\mathrm{d}\Phi(t)}{\mathrm{d}t} \ . \tag{2.1.4}$$

The phase can be expressed as a polynomial function of t, with each term representing a different physical effect. The zeroth term by itself does not contribute to the instantaneous frequency, but instead changes the phase offset between the sine wave and the envelope. This is known as the carrier-envelope phase (CEP) of the pulse, which generally becomes important for laser pulses containing only a few cycles. The first order term shifts the frequency of the electric field oscillations, i.e. $\omega(t) = \omega_0 +$ some constant. The second order term gives rise to a linear change of frequency with time during the pulse. This is known as a linear chirp and is positive when lower frequency components proceed the higher frequencies. Higher order terms result in a more complex relationship between frequency and time, such as quadratic chirp, etc. Figure **2.1** shows $I(t)$ and $\Phi(t)$ for an example pulse. In this case $\Phi(t)$ has a negative gradient at early times and a positive gradient at later times. This indicates that the instantaneous frequency of the pulse is increasing with time, so the pulse has a positive chirp.

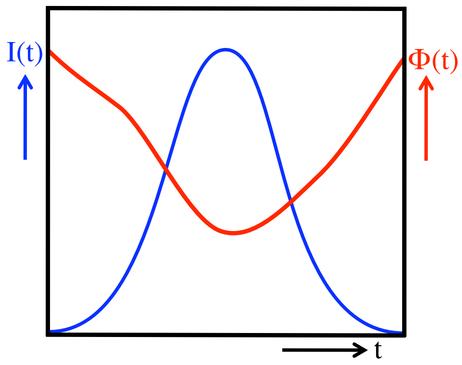

Figure 2.1: Illustration of the temporal intensity and phase for a positively chirped laser pulse.

The electric field can also be represented in frequency space as,

$$\tilde{E}(\omega) = \tilde{E}_0(\omega) \exp\left[i\phi(\omega)\right] \ , \tag{2.1.5}$$

where $\tilde{E}_0(\omega)^2$ is the angular frequency spectrum and $\phi(\omega)$ is the spectral phase. This is related to $E(t)$ by the Fourier transforms:

$$\tilde{E}(\omega) = \int_{-\infty}^{\infty} E(t) \exp\left[-i\omega t\right] \mathrm{d}t \ , \text{ and} \tag{2.1.6}$$

$$E(t) = \frac{1}{2\pi} \int_{-\infty}^{\infty} \tilde{E}(\omega) \exp\left[i\omega t\right] \mathrm{d}\omega \ . \tag{2.1.7}$$

When no second order or higher temporal phase terms are present, and assuming a gaussian pulse shape centred on $t = 0$, equation **2.1.6** can be written as,

$$\tilde{E}(\omega) = \int_{-\infty}^{\infty} E_0 \exp\left[-\frac{\alpha t^2}{2} + i(\omega_0 - \omega)t\right] \mathrm{d}t \ . \tag{2.1.8}$$

This can be solved by completing the square of the exponential, giving the solution,

$$\tilde{E}(\omega) = E_0 \sqrt{\frac{2\pi}{\alpha}} \exp\left[-\frac{(\omega - \omega_0)^2}{2\alpha}\right] \ . \tag{2.1.9}$$

Therefore for a gaussian pulse with no second order or higher phase terms the spectrum is a gaussian centred on ω_0 with zero spectral phase.

Propagating such a pulse through glass, or some other linearly dispersive medium, results in a group delay dispersion (GDD), due to the ω dependence of the refractive index. This gives the pulse a positive chirp, i.e. the frequency of the rapid oscillation of the electric field increases with time. Mathematically this is described by a second order phase term, $\phi(\omega) = -b\omega^2$, for which the temporal pulse shape is now given by,

$$E(t) = \frac{E_0}{2\pi}\sqrt{\frac{2\pi}{\alpha}}\int_{-\infty}^{\infty} \exp\left[-\frac{(\omega-\omega_0)^2}{2\alpha}\right]\exp\left[i(\omega t - b\omega^2)\right]d\omega\ ,$$
$$E(t) = E_0' \exp\left[-\frac{\alpha t^2}{2}\frac{1}{(1+4\alpha^2 b^2)}\right]\exp\left[i\left(\omega_0 t + \frac{\alpha^2 b t^2}{(1+4\alpha^2 b^2)}\right)\right]\ , \tag{2.1.10}$$

where,

$$E_0' = E_0 \frac{1}{\sqrt{1+4\alpha^2 b^2}}\ . \tag{2.1.11}$$

This shows that propagating a pulse with an initially flat phase through glass results in a longer pulse, with a lower peak intensity and a quadratic phase term which is a positive function of t^2. This is shown in figure **2.2**, for an initially 10 fs (FWHM) pulse after propagation through 0, 1 and 2 mm of fused silica. For a negative chirp, where the frequency of the pulse decreases with time, the spectral phase has a $+\omega^2$ term and the temporal phase a $-t^2$ term. A cubic term in the spectral phase corresponds to a quadratic group delay as a function of frequency. This can result in a non-symmetric pulse shape in the time domain.

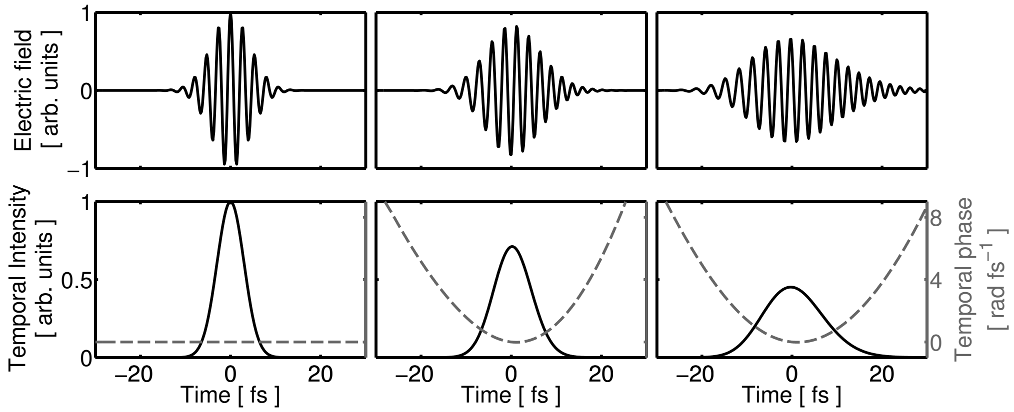

Figure 2.2: An initially 10 fs (FWHM) pulse, with a central wavelength of 800 nm after propagation through (from left to right) 0, 1 and 2 mm of fused silica glass.

2.1.2 Focusing

Focusing an initially collimated laser pulse to a high intensity can be achieved using lenses or concave mirrors. For very high pulse powers, transmission though optics results in pulse lengthening and beam degradation, due to the group velocity dispersion of the optical material and non-linear optical effects. Therefore, concave mirrors are commonly used for high intensity interactions. In particular, parabolic mirrors can achieve perfect focusing of a collimated beam, to a focal spot which is the Fourier transform of the input beam spatial profile. For a uniform circular beam with a flat phase front, the focal spot is described by an Airy disc pattern,

$$I(x) = I_0 \left(\frac{2J_1(x)}{x} \right)^2, \qquad (2.1.12)$$

where J_1 is the first order Bessel function of the first kind, $x = \pi r/(\lambda F)$, r is the lateral position from the centre of focus, λ is the laser wavelength and F is the parabola f/number. The first central peak of equation **2.1.12** is well described by a gaussian function with $r_{\mathrm{FWHM}} = F\lambda$, as shown in figure **2.3**.

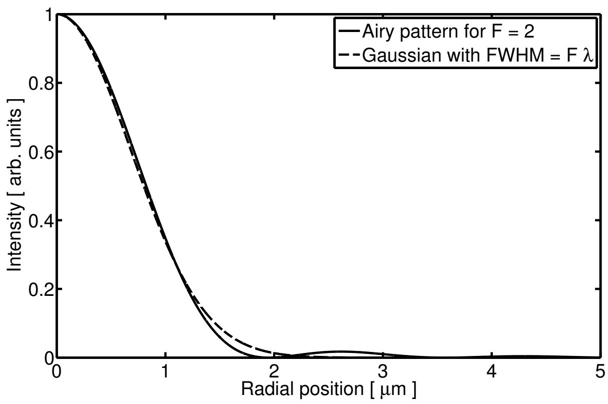

Figure 2.3: Focal spot profile (Airy pattern) for an 800 nm uniform circular laser beam focused by an $f/2$ parabola and a gaussian with a FWHM of $F\lambda$.

The maximum laser intensity increases with decreasing f/number of the focusing beam. In practise it is important to be able to place the target at the focus of the beam, so either an on-axis mirror with a central shadow or, more commonly, an off-axis mirror is used. This places practical limits on the range of viable f/numbers. For a gaussian beam profile, the beam diameter ($1/e^2$) of a focusing beam propagating in the z direction is given by,

$$w(z) = \sigma_r \sqrt{1 + \left(\frac{z}{z_r}\right)^2} , \tag{2.1.13}$$

where σ_r is the beam diameter at the focus (at $z = 0$) and $z_r = \pi {\sigma_r}^2/\lambda$ is the Rayleigh range. Approximating the focusing beam as a gaussian gives the divergence angle of a focal spot as $\Theta_D = \sigma_r/z_r$ [Siegman86].

For non-ideal beams, the maximum achievable laser intensity is reduced, as the laser energy is focused to a larger spot size than in the ideal case. The Strehl ratio (S_r) of a focused pulse is a measure of the peak intensity relative to the Airy function of an ideal circular aperture beam. Another commonly used parameter is M^2, which describes the propagation of the beam through focus compared to the ideal gaussian case,

$$M^2 = \frac{\pi \sigma_r \Theta_D}{\lambda} . \tag{2.1.14}$$

For a gaussian beam $M^2 = 1$, and for real beams $M^2 > 1$. Higher values of M^2 are normally found in higher power lasers, and indicates a reduction in the focusability.

2.1.3 Laser contrast

It is routine in intense laser interactions, with solid-density plasmas, that the majority of the laser pulse interacts directly with the front surface of the target, and energy is then transported into the bulk. For an ultra-intense laser pulse, the plasma is usually formed well in advance of the peak of the laser pulse by pre-pulses or an amplified spontaneous emission (ASE) pedestal generated in the laser amplifiers. This results in an electron density profile $n_e = n_e(x)$, with a scale length $L_\mathrm{p} = \left[\frac{\partial\,(\ln n_e)}{\partial x}\right]^{-1}$, which can be much larger than the laser wavelength [Carroll09, Zepf98, Mackinnon01]. Therefore, the ratio of the intensity of the ASE pedestal to the peak of the pulse is an important parameter, and is known as the laser 'contrast'. It is also important to know the temporal extent of the pedestal, the shape of the rising edge of the main pulse and if there are any significant pre-pulses.

Solid density interactions with thin targets are particularly sensitive to pre-plasma formation. Here, in addition to lengthening the interaction scale length, it can also reduce the peak plasma density of the target, or even destroy the target completely before the arrival of the main pulse [Kaluza04]. Laser absorption mechanisms also differ when the scale length of the plasma is decreased, for example resonance absorption occurs with scale lengths many times the laser wavelength, while vacuum heating only occurs when the scale length is less than the laser wavelength [Santala00]. Laser contrast is therefore of critical importance to laser-plasma interactions.

2.1.4 Nonlinear optics

Until the invention of the laser, all observed optical processes could be explained by linear theory (e.g. absorption, refraction, interference etc). With the high intensities achievable with lasers, the electromagnetic field is strong enough for non-linearities in the material response to become significant. This allows for phenomena such as wave-mixing and self-focusing. This can be described by the macroscopic Maxwell's equations, which include the interaction of electromagnetic fields with matter via the polarisation **P** and the magnetisation **M** terms as follows [Agrawal01],

$$\nabla \cdot \mathbf{D} = \rho \ , \tag{2.1.15a}$$

$$\nabla \cdot \mathbf{B} = 0 \ , \tag{2.1.15b}$$

$$\nabla \times \mathbf{E} = -\frac{\partial \mathbf{B}}{\partial t} \ , \tag{2.1.15c}$$

$$\nabla \times \mathbf{H} = \frac{\partial \mathbf{D}}{\partial t} + \mathbf{J} \ , \tag{2.1.15d}$$

where ρ is the free charge density, $\mathbf{J}$ is the free current density, $\mathbf{D} = \epsilon_0 \mathbf{E} + \mathbf{P}$ and $\mathbf{H} = \mathbf{B}/\mu_0 - \mathbf{M}$. For dielectric, non-magnetic materials the conductivity and magnetisation are negligibly small and the only non-linear term remaining is from the polarisation. Assuming that the material is locally charge neutral everywhere, and that $\mathbf{E}$ varies only in one spatial dimension, then equations **2.1.15a**, **2.1.15c** and **2.1.15d** can be combined into a single expression for non-linear electro-optics,

$$\frac{\partial^2 \mathbf{E}}{\partial z^2} - \frac{1}{c^2}\frac{\partial^2 \mathbf{E}}{\partial t^2} = \mu_0 \frac{\partial^2 \mathbf{P}}{\partial t^2} \ . \tag{2.1.16}$$

P is a function of the driving electric field and the material response to those fields and can be expressed as,

$$P_\alpha(\mathbf{r}, t) = \sum_\beta \chi^{(1)}_{\alpha\beta} E_\beta(\mathbf{r}, t) + \sum_{\beta\gamma} \chi^{(2)}_{\alpha\beta\gamma} E_\beta(\mathbf{r}, t) E_\gamma(\mathbf{r}, t) + \ldots \ , \tag{2.1.17}$$

where $\chi^{(n)}$ is the n^{th} order susceptibility tensor and the indices (α, β and γ) range over the three spatial dimensions. The susceptibility tensors are diagonal for isotropic materials (i.e. gases) so that electric fields applied in one direction result in a polarisation purely in the same direction. At low intensities, the 1^{st} order term dominates and **P** is linearly proportional to the driving electric field. In this case and for an isotropic material $\mathbf{D} = \epsilon\mathbf{E}$, where ϵ is the permittivity of the medium, which reduces equation **2.1.16** to,

$$\frac{\partial^2 \mathbf{E}}{\partial z^2} - \frac{\eta^2}{c^2}\frac{\partial^2 \mathbf{E}}{\partial t^2} = 0 \ , \tag{2.1.18}$$

where η is the refractive index of the medium. Equation **2.1.18** describes the linear response of the medium to the electric field and gives the dispersion relation.

Higher order terms in the polarisation result in the mixing of two or more waves, which can be grouped together as a source term, $\mathbf{P}^{\mathrm{NL}}$,

$$\frac{\partial^2 \mathbf{E}}{\partial z^2} - \frac{\eta^2}{c^2}\frac{\partial^2 \mathbf{E}}{\partial t^2} = \mu_0 \frac{\partial^2 \mathbf{P}^{\mathrm{NL}}}{\partial t^2} \ . \tag{2.1.19}$$

The second order term of $\mathbf{P}^{\mathrm{NL}}$ leads to second harmonic generation (SHG) and sum frequency generation (SFG), which result in frequencies of $2\omega_1$ and $\omega_1 + \omega_2$ respectively. The third order term, known as the Kerr effect, causes self-focusing and self-phase modulation.

2.1.5 Ionisation

Photo-ionisation of atoms can occur via multi-photon ionisation (MPI), tunnelling ionisation and barrier suppression ionisation (BSI). Collisional ionisation can also occur once the plasma temperature is sufficiently high. In the MPI model an electron absorbs energy from incident photons faster than it can radiate the energy, causing the electron to gain enough energy to escape the atomic bond. This process occurs for laser intensities above 10^{10} Wcm^{-2} [Gibbon05b] but for $I > 10^{15}$ Wcm^{-2} tunnelling ionisation becomes dominant. BSI occurs when the Coulomb barrier is reduced by the laser field such that the electron is no longer bound. The minimum intensity for BSI is known as the appearance intensity [Augst89],

$$I_{\mathrm{app}} = \frac{c\mathcal{E}_b{}^4 \pi^2 \epsilon_0^3}{2e^6 Z^2} \ . \tag{2.1.20}$$

where $\mathcal{E}_b$ is the binding energy for an electron and Z is the number of protons in the nucleus. Table **2.1** gives some examples of binding energies and appearance intensities for ion states expected in this thesis.

At the intensities considered in this thesis it is clear that instantaneous ionisation via BSI occurs well before the peak of the laser pulse. The proportion of ionisation states and the electron densities can be estimated using equation **2.1.20** but other ionisation mechanisms may also have some effect.

Ion	Binding energy [eV]	I_{app} [Wcm^{-2}]
H^{+}	13.6	1.4×10^{14}
He^{+}	24.6	1.5×10^{15}
He^{2+}	54.4	8.8×10^{15}
C^{4+}	64.5	4.3×10^{15}
C^{5+}	392.1	3.8×10^{18}
C^{6+}	490.0	6.4×10^{18}
Al^{11+}	442.0	1.3×10^{18}
Al^{13+}	2304.1	6.7×10^{20}

Table 2.1: Binding energies [Kramida11] and appearance intensities of some ionisation states relevant to experiments in this thesis.

2.2 Particle motion in an electromagnetic field

Starting with the Lorentz force and Maxwell's equations, and assuming a plane wave interacts with a single electron, the transverse and longitudinal momentum components of that electron are given by [Gibbon05b] (full derivation in appendix **A.1**),

$$p_{\perp} = a m_e c \,, \tag{2.2.1}$$

$$p_{\parallel} = \frac{m_e c(1 + a^2 - \alpha^2)}{2\alpha} \,, \tag{2.2.2}$$

where $a = \dfrac{eE_0}{m_e \omega_0 c} \cos\phi$, where $\phi = \omega_0 t - k_0 z$, and α is a constant that comes from integrating the force equation with respect to time. The quantity $-\left(\dfrac{\alpha^2 - 1}{2\alpha}\right) m_e c$ is the longitudinal electron momentum when the transverse momentum is zero.

The Lorentz factor, and velocity components are,

$$\gamma = \frac{a^2 + \alpha^2 + 1}{2\alpha} \,, \tag{2.2.3}$$

$$v_{\perp} = \frac{2\alpha\, a\, c}{a^2 + \alpha^2 + 1} \,, \tag{2.2.4}$$

$$v_{\parallel} = \frac{(1 + a^2 - \alpha^2)\, c}{a^2 + \alpha^2 + 1} \,. \tag{2.2.5}$$

It is possible to set a value of α, for each a_0, which removes any constant drift velocity from the equations of motion, so that the electron oscillates around a fixed average position.

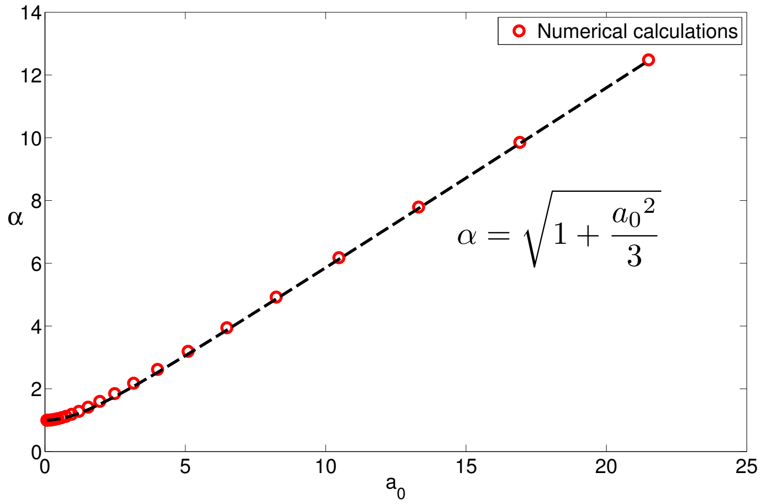

Figure 2.4: Numerically calculated values of α which minimise the electron drift motion and an empirical fit.

2.2.1 Electron heating

When a laser is incident upon a solid density plasma, the time averaged motion of the reflecting surface is small compared to the rapid oscillation of the electrons, i.e. $\langle v_\parallel \rangle \ll c$. To estimate the average energy of electrons in the laser field, the longitudinal drift motion of the electrons is set to zero, i.e. $\langle v_\parallel \rangle = 0$, to determine α. This is easily calculated numerically and the dependence of α on a_0, as shown in figure **2.4**, has an excellent fit to $\alpha = \sqrt{1 + {a_0}^2/3}$, for which the maximum γ in equation **2.2.3** becomes,

$$\gamma = \frac{4{a_0}^2 + 6}{6\sqrt{1 + {a_0}^2/3}} \, . \tag{2.2.6}$$

This differs from other similar work which sets $\langle p_\parallel \rangle = 0$ [Gibbon05b], which gives $\alpha = \sqrt{1 + {a_0}^2/2}$. However, in that case some residual longitudinal drift velocity remains, due to the time-varying nature of γ.

At a sharp density gradient, electrons accelerated by the laser in the forward direction propagate beyond a skin depth and therefore escape the influence of the laser field. This leads to a population of energetic electrons propagating through the target which can heat the bulk plasma. The maximum energy of these electrons is given by $\mathcal{E}_e = (\gamma - 1)m_e c^2$. Assuming that the electrons at the front surface oscillate with $\langle v_\parallel \rangle = 0$ and escape with the maximum γ, given by equation **2.2.6**, the maximum energy of these electrons, for

$a_0 \gg 1$, is,

$$\mathcal{E}_e \simeq \frac{2}{\sqrt{3}} a_0 m_e c^2 \,, \tag{2.2.7}$$

which is in very close agreement with Wilks *et al.* [Wilks92].

2.2.2 Electron trajectories

Solving equations **2.2.3–2.2.5**, with α chosen to remove the particle drift, gives a picture of how an electron moves in a laser field in the frame of reference co-moving with the particle drift velocity. Figure **2.5** shows the particle trajectories for laser fields with $a_0 = 0.1 - 10$. As the a_0 increases, the lateral excursion distance of the electrons increases. Also, the relativistic electron velocity leads to an increase in the effect of the magnetic field component, leading to a large oscillation in longitudinal direction.

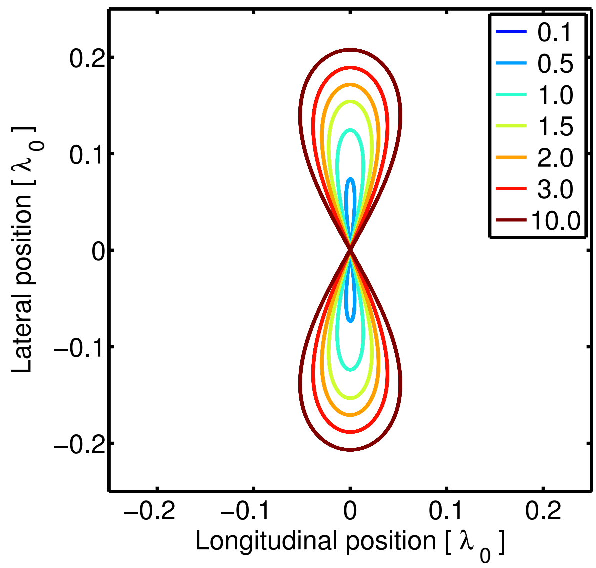

Figure 2.5: Trajectories of a single electron in a laser field with $a_0 = 0.1$–10 (given in the legend) in frame co-moving with the drift velocity.

2.2.3 Ponderomotive force

Over timescales greater than the laser period, the fast oscillation of the electrons largely cancels out. What remains is known as the ponderomotive force [Chen06,Kruer88], which is expressed as the rate of change of momentum of an electron, averaged over the laser cycle. The Lorentz force of a single electron in an electromagnetic wave can be written as (see appendix **A.1**),

$$\frac{\mathrm{d}\mathbf{p}}{\mathrm{d}t} = m_e c \frac{\mathrm{d}\mathbf{a}}{\mathrm{d}t} - m_e c \mathbf{v} \cdot (\nabla \mathbf{a}) \ . \tag{2.2.8}$$

Taking the first order solution for an infinite plane wave, $\mathbf{v} = \frac{\mathbf{p}_\perp}{\gamma m_e} = \frac{\mathbf{a}c}{\gamma}$, equation **2.2.8** becomes,

$$\frac{\mathrm{d}\mathbf{p}}{\mathrm{d}t} = m_e c \frac{\mathrm{d}\mathbf{a}}{\mathrm{d}t} - \frac{m_e c^2}{2\gamma} \nabla \mathbf{a}^2 \ . \tag{2.2.9}$$

Taking the time average over a laser period of equation **2.2.9** and assuming that the laser envelope is constant gives,

$$\mathbf{F}_\mathbf{p} = \left\langle \frac{\mathrm{d}\mathbf{p}}{\mathrm{d}t} \right\rangle = -\frac{m_e c^2}{2 \langle \gamma \rangle} \nabla \left\langle \mathbf{a}^2 \right\rangle \ . \tag{2.2.10}$$

This simplified derivation shows that electrons experience an overall repulsive force from regions of high laser intensity. This result is also recovered in a more rigorous and fully relativistic derivation, given by Quesnel and Mora [Quesnel98].

2.3 Plasma properties

A plasma is defined as a quasi-neutral substance, consisting of positive and negative charged particles, that exhibits collective electromagnetic behaviour. Individual particles interact with each other via their electrostatic fields and through collisions. Particles may also interact with external electromagnetic fields. It is possible to characterise particles in a plasma by the mass and electric charges which define their behaviour. As electrons have the largest charge-to-mass ratios they are much more mobile than the ions and tend to dominate the plasma reaction to electromagnetic fields. Ions can also gain energy through their interactions and collisions with electrons. For a plasma in thermodynamic equilibrium electrons and ions each have a temperature T as defined by the Maxwell-Boltzmann distribution for particles with three degrees of freedom:

$$E_{\mathrm{av}} = \frac{3}{2} k_B T \tag{2.3.1}$$

where k_B is the Boltzmann constant.

For an absorption of 1 J of laser energy into 100 μm diameter spot on a 100 nm aluminium target, the resultant temperature would be ≈ 1.5 keV.

2.3.1 Debye length

The Debye length is a measure of the distance over which the electrostatic field of a particle in a plasma is shielded by neighbouring charges, and is given by [Chen06],

$$\lambda_D = \left(\frac{\epsilon_0 k_B T_e}{n_e e^2}\right)^{\frac{1}{2}} , \tag{2.3.2}$$

where T_e and n_e are the electron temperature and number density respectively.

The number of particles N_D within a sphere with radius λ_D gives a good indication of the collective behaviour of the plasma,

$$N_D = n_e \pi {\lambda_D}^3 = \frac{n_e}{\pi}\left(\frac{\epsilon_0 k_B T_e}{n_e e^2}\right)^{\frac{3}{2}} . \tag{2.3.3}$$

A plasma should have a size which is much greater than the Debye length in order that it is quasi-neutral and N_D should be much greater than unity. For the laser generated plasma defined above $\lambda_D \approx 1$ nm and $N_D \approx 3000$.

2.3.2 Plasma frequency

The plasma frequency is the frequency of the natural oscillation of electrons in a plasma and is given by

$$\omega_{pe} = \left(\frac{n_e e^2}{m_e \epsilon_0}\right)^{\frac{1}{2}} . \tag{2.3.4}$$

For a plasma, any density oscillations are also electromagnetic in nature and so the plasma frequency is critical to laser-plasma interactions. An electromagnetic wave is not able to propagate through a plasma if it has a lower frequency than the plasma frequency (see section 2.3.5).

2.3.3 Plasma dispersion relation

Taking the curl of equation **2.1.15c** and the time derivative of equation **2.1.15d**, for the case of an unmagnetised plasma (with zero bound charge) gives,

$$\nabla \times (\nabla \times \mathbf{E}) = -\nabla \times \frac{\partial \mathbf{B}}{\partial t} , \tag{2.3.5}$$

$$\nabla \times \frac{\partial \mathbf{B}}{\partial t} = -\mu_0 \epsilon_0 \frac{\partial^2 \mathbf{E}}{\partial t^2} + \mu_0 \frac{\partial \mathbf{J}}{\partial t} . \tag{2.3.6}$$

For non-relativistic intensities ($a_0 \ll 1$) and an infinite plane wave, the electric current is caused by the transverse motion of charges,

$$\frac{\partial \mathbf{J}}{\partial t} = -n_e e \frac{\partial \mathbf{v}}{\partial t} = \frac{n_e e^2}{m_e} \mathbf{E} \, . \tag{2.3.7}$$

Combining these equations to eliminate **B** and **J** and evaluating the differentials for a infinite plane wave, $E(t, x) = E_0 \cos(\omega t - kx)$, gives the plasma dispersion relation,

$$\omega^2 = {\omega_p}^2 + k^2 c^2 \, . \tag{2.3.8}$$

2.3.4 Refractive index

The phase velocity of an electromagnetic wave in a plasma is given by

$$v_\phi = \frac{\omega}{k}, \tag{2.3.9}$$

$$v_\phi = c \left(1 - \frac{{\omega_p}^2}{\omega^2}\right)^{-\frac{1}{2}} . \tag{2.3.10}$$

Given the definition of the refractive index, $\eta = c/v_\phi$, the plasma refractive index is therefore,

$$\eta = \left(1 - \frac{{\omega_p}^2}{\omega^2}\right)^{\frac{1}{2}} . \tag{2.3.11}$$

The group velocity of an electromagnetic wave is then given by,

$$v_g = \frac{\partial \omega}{\partial k} \, , \tag{2.3.12}$$

$$v_g = \eta c \, . \tag{2.3.13}$$

2.3.5 Critical density

For laser plasma interactions, the density at which the plasma frequency equals the laser frequency is termed the critical density and is given by,

$$n_c = \frac{\omega_L^2 m_e \epsilon_0}{e^2} \, , \tag{2.3.14}$$

where ω_L is the laser carrier frequency. Interactions with plasma densities below this critical density are called underdense interactions, for which the refractive index of the plasma, given by equation **2.3.11** is real. For $n_e > n_c$ (overdense) the refractive index becomes complex and therefore damps the propagating field, resulting in reflection of the laser pulse.

2.3.6 Transmission and reflection

For an electromagnetic wave propagating in the z direction, the electric field can be written as,

$$E = E_0 \exp\left[i(\omega t - kz)\right] . \tag{2.3.15}$$

Substituting the equation **2.3.8** for k results in

$$E = E_0 \exp\left[i\left(\omega t - \frac{\omega\eta}{c} z\right)\right]. \tag{2.3.16}$$

Taking the partial derivative with respect to z then describes how the wave changes as it propagates through the plasma,

$$\frac{\partial E}{\partial z} = -i\frac{\omega\eta}{c}E . \tag{2.3.17}$$

Equation **2.3.17** shows that when η is real only the phase of the wave changes with propagation distance but any imaginary component of η (for $n_e > n_c$) results in damping of the wave. The distance over which the electric field drops to $1/e$ of the input field is known as the skin depth and is given by

$$\delta_s = \frac{c}{\omega}\left(\frac{n_e}{n_c} - 1\right)^{-\frac{1}{2}} . \tag{2.3.18}$$

2.3.7 Relativistic transparency

For high intensity lasers, the electron oscillation velocity can approach c and the plasma frequency must be modified by the γ factor due to the relativistic mass increase of the electrons. This effectively reduces the plasma frequency and increases the critical density for a fixed wavelength laser pulse. Including this consideration, the refractive index of the plasma can be estimated by

$$\eta = \left(1 - \frac{n_e}{\langle\gamma\rangle\, n_c}\right)^{\frac{1}{2}} . \tag{2.3.19}$$

where n_c is the non-relativistic critical density. The Lorentz factor, averaged over the laser cycle can be expressed as (using equation **2.2.3** with $\alpha = 1$),

$$\langle\gamma\rangle = 1 + \frac{\langle a^2\rangle}{2} = 1 + \frac{{a_0}^2}{4}\ , \quad \text{for linear polarisation.} \tag{2.3.20}$$

Therefore, the skin depth of the plasma is lengthened for large a_0 and the reflecting surface moves due to this effect. The actual a_0 during the interaction may also change due to interaction with the plasma, again changing the effective skin depth of the plasma. A more rigorous expression for η would require consideration of the full plasma effect and the influence of the reflected laser, such as given in [Weng12].

2.4 Over-dense plasma absorption processes

Plasmas for which $\omega_p > \omega_0$ are opaque and so the laser is reflected at the plasma surface. However, the laser always interacts with some volume of the plasma and so some of the energy of the laser pulse is absorbed. Several basic mechanisms exist by which this can occur.

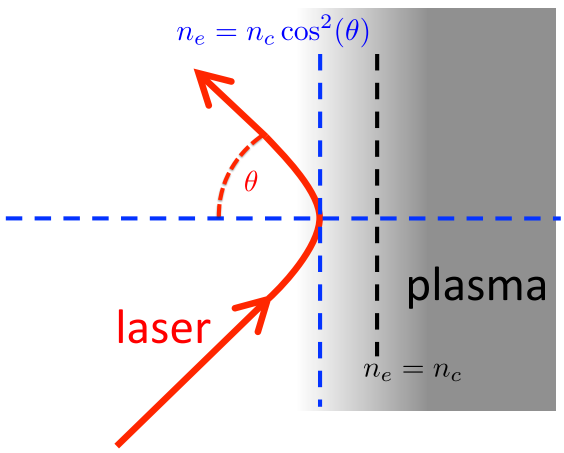

Figure 2.6: For oblique angles of incidence the laser does not propagate to the critical density surface. Instead it is refracted away at the surface with $n_e = \cos^2\theta$.

2.4.1 Resonance absorption

Resonance absorption occurs in solid target interactions for the electric field component which is parallel to the density gradient of the plasma. In this process, electrons oscillate in the electric field and couple to plasma waves in the target. This can transfer energy into the target beyond the region in which the laser field penetrates. Resonance occurs in the region where $n_e = n_c$, where the oscillation of the electrons can be driven by the evanescent electric field. This process requires a relatively large scale length plasma ($L_\mathrm{p} \gg \lambda$), for the generation of plasma waves.

2.4.2 Vacuum heating

For very sharp density gradients electrons are accelerated into the target beyond the penetration depth of the laser within one oscillation of the electric field. This requires that the typical oscillation displacement of the electrons is greater than the scale length of the plasma, i.e. $r_\mathrm{osc} > L_\mathrm{p}$. Therefore, the electron is screened from the electric field before it can reverse direction and does not feel the restoring force. This process generates fast electrons at the target surface that propagate through the target and can transfer energy to plasma which is remote from the laser field.

2.4.3 $\mathbf{J} \times \mathbf{B}$ heating

When the intensity becomes high enough ($> 10^{18}$ Wcm^{-2}), the electrons no longer experience simple harmonic motion as the magnetic field of the laser pulse begins to contribute significantly to the acceleration. For the case of linear polarisation, as the electron moves in the electric field it experiences a $\mathbf{J} \times \mathbf{B}$ force, which deflects the electrons in the propagation direction of the laser. As the transverse electron velocity reverses so does the direction of the $\mathbf{J} \times \mathbf{B}$ force, causing the electron to move in an approximately 'C' shaped trajectory. At the critical surface this can push electrons, at $2\omega_0$, into the plasma beyond the laser field (again for $r_\mathrm{osc} > L_\mathrm{p}$), where they can then travel into the plasma and deposit energy into the target.

2.5 Ion acceleration from solid targets

Interactions of high intensity lasers with solid density plasmas has resulted in ion beams with peak energies of many 10's MeV/nucleon [Snavely00, Clark00]. The laser energy is transferred preferentially to the electrons in a plasma due to their higher charge to mass ratio. Therefore, all ion acceleration mechanisms (at least for $a_0 < 2000$) rely on transfer of energy from the electrons to the ions in some way. The dominant mechanism by which this transfer occurs depends on the laser intensity, the plasma density distribution and the geometry of the interaction.

For a typical planar foil target, the nature of the interaction changes with the changing laser intensity and the expansion and heating of the target. Firstly, the laser rapidly ionises the target and energetic electrons, generated by the ponderomotive force of the laser, expand in all directions. Electrostatic fields are generated at the surfaces which act to confine electrons to the target. Ions are also accelerated by these sheath fields and the target expands. At high laser intensities, the radiation pressure of the laser exerts a significant force on the laser-plasma boundary, which can accelerate this boundary in the laser propagation direction. If the target is thin enough ($< \tau v_{\mathrm{hb}}$), then the hole boring front reaches the back of the target such that a small section of plasma breaks free and is accelerated as a single mass by the radiation pressure of the laser. The plasma in this case is free to expand laterally away from the laser and the density can drop below the relativistic critical density. Then the laser maybe propagate freely through the plasma stopping the radiation pressure acceleration and further heating the electron population.

2.5.1 Sheath acceleration

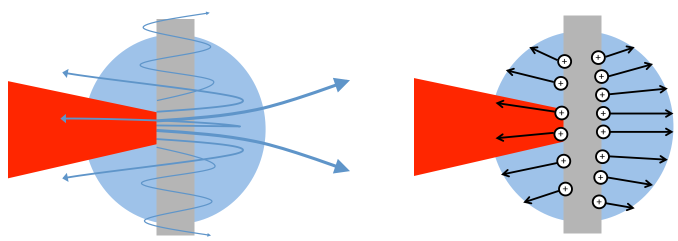

(a) (b)

Figure 2.7: a) Electrons gain energy from the ponderomotive force and are expelled from the laser focus. An electrostatic sheath field is established at the front and rear surfaces of the target. b) Ions are accelerated by the sheath field at the front and rear surface of the target.

Electrons in the focal volume of an intense laser gain an energy approximately equal to the ponderomotive potential (given by the spatial integral of equation **2.2.10**) as $\mathcal{E}_e = mc^2 {a_0}^2/4$. Therefore, for $a_0 > 1$ electrons with $\mathcal{E}_e > 100$ keV are constantly accelerated from the laser focus. The mean free path of electrons of this energy in aluminium is 100s of microns and so they can travel through thin targets and reach the rear surface. At this point they generate a restoring electrostatic force which, along with that set up by other electrons, accelerates the electrons back through the target again.

Depending on the target thickness, this 'recirculation' can occur many times. Due to the planar geometry, the direction of electrostatic sheath fields at both front and rear surfaces is approximately normal to the target surface, leading to a planar acceleration of ions [Snavely00,Clark00,Wilks01,Fuchs05]. Ions are predominantly accelerated from near the target surfaces, which typically have environmental contamination layers. Therefore, as well as the bulk ions from the target material, most experiments also see strongly accelerated hydrogen, carbon and oxygen ions.

To first order, the peak ion energy generated by this mechanism can be calculated as [Mora03],

$$\mathcal{E}_i \simeq 2\left(\frac{n_e k_B T_e}{\epsilon_0}\right)^{\frac{1}{2}}\left(\ln\left[\left(\frac{2}{e}\right)^{\frac{1}{2}}\omega_{pi}t\right]\right)^2 , \tag{2.5.1}$$

where ω_{pi} is the ion plasma frequency, t is the acceleration time, and T_e is the electron temperature. Taking the ponderomotive scaling for T_e (section 2.2.1), gives $\mathcal{E}_i \propto (I_L\lambda)^{\frac{1}{2}}$.

2.5.2 Radiation pressure acceleration

The momentum change of photons when light reflects or is absorbed at a surface causes that surface to accelerate [Marx66]. For the case of a surface at rest with a laser at normal incidence this force is given by,

$$F_{\mathrm{ph}} = \frac{\mathrm{d}p_{\mathrm{ph}}}{\mathrm{d}t} = \frac{I}{c}A(1+R), \tag{2.5.2}$$

where I is the laser intensity, A is the surface area, and R is the reflectivity of the surface. This force acts to push electrons away from the laser, creating an electrostatic potential which accelerates the initially static ions in the laser propagation direction. This electrostatic potential moves through the plasma at a velocity at which the change in momentum of the photons and the plasma ions balance. This velocity is known as the hole-boring velocity [Wilks92], v_{hb}, as it is the rate at which a laser can bore a hole into a plasma surface. In the frame of reference moving at the hole-boring velocity (see figure **2.8**), the rate of change of momentum of the ions in the plasma is (assuming 100% reflection of the ions),

$$\frac{\mathrm{d}p_{\mathrm{i}}}{\mathrm{d}t} = 2n_{\mathrm{i}}m_{\mathrm{i}}A{v_{\mathrm{hb}}}^2 . \tag{2.5.3}$$

Equating equations **2.5.2** and **2.5.3** gives the hole boring velocity as,

$$v_{\mathrm{hb}} = \left(\frac{I\,(1+R)}{2cn_{\mathrm{i}}m_{\mathrm{i}}}\right)^{\frac{1}{2}}, \tag{2.5.4}$$

For a laser with $I = 1\times10^{21}\ \mathrm{W\,cm^{-2}}$ and a solid carbon target then $v_{\mathrm{hb}} \approx 0.01c$. For such parameters the interaction can be accurately treated as non-relativistic so that the derivation of equation **2.5.4** is valid and in this case the resultant accelerated ion energy is,

$$\mathcal{E}_i = \frac{I(1+R)}{cn_i}\,. \tag{2.5.5}$$

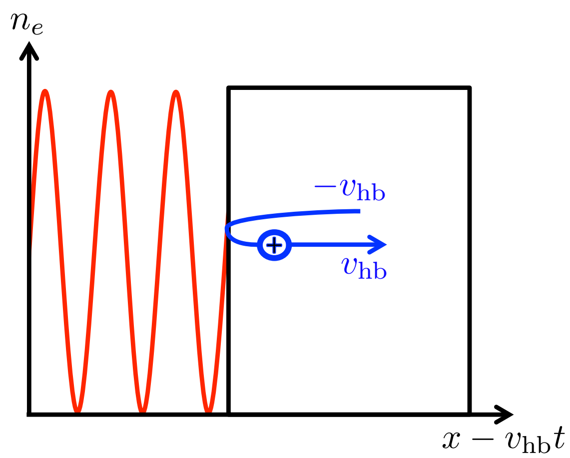

Figure 2.8: The radiation pressure of the laser creates a force in the propagation direction at the laser plasma boundary, which is balanced by the acceleration of the ions in the plasma. The ions reflect from the laser plasma boundary and are accelerated to $2v_{\mathrm{hb}}$.

For multi-species targets the hole-boring velocity is determined by the mass density of the target and all ions are accelerated to the same energy per nucleon. Therefore, high intensity laser pulses and lower density targets increase the maximum energy of the ions produced. For $v_{hb} \sim c$ a fully relativistic derivation is required, and is provided by [Robinson09].

It is also possible for high intensity lasers to drive a non-collisional electrostatic shock that propagates through the target at a few times the ion sound speed [Silva04] and can accelerate background ions in the same ways as hole-boring acceleration. As the ion sound speed increases with temperature, $c_s = \sqrt{Zk_bT_e/m_i}$, a hotter plasma will result in a higher energy for shock accelerated ions. Therefore, the final ion energy has a weak dependence on laser intensity, $\mathcal{E}_i \propto \sqrt{a}$.

For targets with thickness (d) on the order of the plasma skin depth, the entire electron population is subject to the radiation pressure, and the ions in the target may be accelerated as a whole. This is known as the 'light sail' mechanism, as the radiation pressure acts to accelerate a fixed mass of plasma. Equation **2.5.2** is then balanced by the acceleration of the ions:

$$\frac{I}{c}A(1+R) = n_i m_i d A \frac{\mathrm{d}v}{\mathrm{d}t} \ . \tag{2.5.6}$$

The ion energies can be estimated by integrating equation **2.5.6** from an initial state of rest over the interaction duration. Assuming a top hat pulse of duration τ the final ion energy is,

$$\mathcal{E}_i = \frac{m_i}{2}\left[\frac{\tau I}{c\sigma_A}(1+R)\right]^2 \ . \tag{2.5.7}$$

where $\sigma_A = n_i m_i d$ is the areal density of the target. For $I = 1 \times 10^{21}$ W cm^{-2}, $\tau =$ 30 fs and a 5 nm carbon target then $v_i \approx 0.04c$. Here the ion velocities are still well described non-relativistically. However, the linear scaling with τ/d makes it possible to achieve conditions for which relativistic effects become important. Taking into account the Doppler shifted laser intensity and the relativistic mass increase as in [Esirkepov04, Robinson08], the ion momentum is given by,

$$p_i = m_i c\left(\sinh(\psi) - \frac{1}{4\sinh(\psi)}\right), \tag{2.5.8}$$

where,

$$\psi = \frac{1}{3}\sinh^{-1}\left[\frac{6It}{\sigma_A c^2} + 2\right]. \tag{2.5.9}$$

Light sail acceleration has the most promising intensity scaling of all the mechanisms described here. However, if you include the necessity that the target must reflect the laser pulse, then the required target mass scales with intensity also. This reduces the maximum energies attainable for $a_0 \gg 1$ compared to when this requirement is ignored.

Figure **2.9** shows the theoretical maximum ion energies per nucleon for optimal conditions with a 40 fs Ti-Sapphire laser. The maximum ion energies from sheath acceleration are calculated from equation **2.5.1** [Mora03], with the acceleration duration taken as the pulse duration of the laser. For the hole-boring calculations, a pure hydrogen plasma at the relativistic critical density is chosen to maximise the predicted energies while maintaining reflection of the driving pulse. For the light-sail acceleration calculations, the target thickness is set to the relativistic skin depth. The maximum ion energy then occurs when

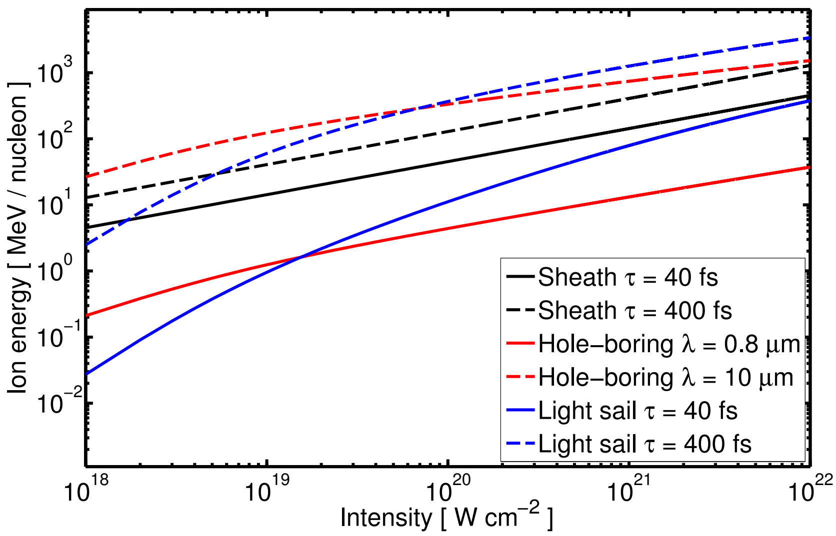

Figure 2.9: Theoretical energy scalings of three ion acceleration mechanisms for ideal conditions. The requirement that the plasma reflects the laser reduces the energy scaling of the light-sail and hole-boring mechanisms for $a_0 \gg 1$.

the target is twice the relativistic critical density. Also plotted are enhanced regimes for which the pulse length is increased (sheath and light-sail acceleration), and the laser wavelength is increased (hole-boring acceleration). It is interesting to note that although the radiation pressure driven mechanisms have a faster scaling with intensity than sheath acceleration, the target requirements reduce this scaling at high intensity. In addition, it seems that sheath acceleration is still hard to beat for an ultrashort laser. But with longer pulse lengths light-sail acceleration becomes more favourable. Using a longer wavelength is also beneficial as lower density plasmas can be used to enhance hole-boring and light-sail velocities. Indeed, recent experiments have made use of 10 μm lasers to generate proton beams from gas targets with very narrow energy spreads [Palmer11, Haberberger11].

2.6 Harmonic generation in solid density plasmas

Several mechanisms exist for the generation of harmonics of a driving laser frequency in a plasma. These can convert some of the laser energy into shorter wavelength beams, which can be useful for secondary applications or as a diagnostic of the plasma. The degree to which harmonic generation occurs, and also what mechanism is responsible, depends both on the laser intensity, the plasma geometry and density profile.

2.6.1 Reflected laser harmonics

The electromagnetic oscillation of the laser pulse acts to drive electron currents in the target surface at the fundamental frequency of the laser ω_0. The driving laser then couples with this oscillation and can lead to new frequency components being generated at integer harmonics of the laser frequency. The reflected laser can only couple to oscillations which are normal to the plane of reflection, and so the ω_0 motion is only seen for p-polarised interactions. However, for normal incidence, or for s-polarised interactions, the laser can couple to the $J \times B$ motion of the electron at $2\omega_0$, resulting in odd order harmonics only. The efficiency of energy conversion to harmonics increases rapidly once the electron motion becomes relativistic, i.e. for $a_0 > 1$. This mechanism is known as the relativistic oscillating mirror (ROM) [Bulanov94, Lichters96, Linde96, Gordienko04, Baeva06] and was observed both in computer PIC simulations [Gibbon96, Plaja98] and experimentally [Norreys96, Zepf98, Tarasevitch00, Dromey06].

2.6.2 Plasma wave emission

The oscillating electric and magnetic fields can drive electron bunches into the target at ω_0 and $2\omega_0$. As these electron bunches travel through the plasma they can set up plasma oscillations at the local resonant frequency, dictated by the plasma frequency. These plasma waves can in turn emit radiation (via linear mode conversion [Sheng05]), from either the front or rear surfaces of the target, containing harmonics of the electron bunch frequency up to the maximum resonant plasma frequency, limited by the peak density of the target [George09]. This process, known as coherent wake emission (CWE) [Quéré06], is efficient for $a_0 \ll 1$ and for solid density plasma, harmonics up to 20–30 ω_0 are generated. Measuring the peak observed harmonic order can be a useful diagnostic of plasma density, especially in the case of pre-expanded thin targets [Hörlein11].

2.6.3 Transition radiation

The electron bunches generated at the laser-plasma boundary can also generate transition radiation as they cross the plasma-vacuum boundary at the rear of the target. This radiation is coherently generated at wavelengths which are larger than the longitudinal structures of the bunch. For shorter wavelengths the radiation is incoherent and therefore produced with a much lower efficiency. Electron bunches driven by the oscillating laser fields arrive at regular time intervals $2\pi/\omega_0$ or π/ω_0, so the emitted radiation is constructed of harmonics of ω_0 or $2\omega_0$ [Zheng03, Bellei12]. In addition, the emitted spectral intensity has a strong negative dependence on frequency at $\omega \sim \omega_p$ [Schroeder04].

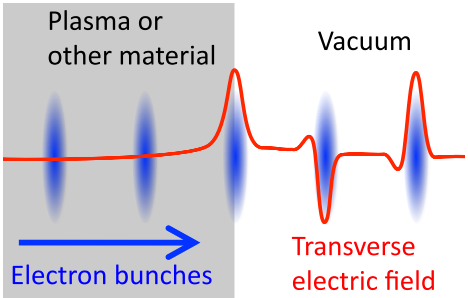

Figure 2.10: The regularly spaced electron bunches generate an electromagnetic field as they cross the boundary between materials with different dielectric constants.

2.7 Electron acceleration in underdense plasmas

As a laser propagates through underdense plasma, the ponderomotive force expels electrons from regions of high intensity. As the laser propagates onwards, the expelled electrons experience a net positive charge on axis. The attractive restoring force causes the electrons to oscillate radially at the plasma frequency and so a plasma wave is generated in the wake of the laser pulse as shown in figure **2.11**. For a laser which has a shorter pulse duration than half of the plasma wave period this process is resonant [Andreev92], leading to a stronger density perturbation.

The phase velocity of the plasma wave is determined by the group velocity of the laser, which is dependent on the density of the plasma as in equation **2.3.12**. The longitudinal structure of the plasma wave is shown in figure **2.12**. An electron positioned in this plasma wave would experience a longitudinal force from the electrostatic field that would act to accelerate the electron either forwards or backwards, depending on the position of the electron. The force on the electron also changes in time, due to the relative motion of the electron and the plasma wave. However, if an electron can be accelerated to close to v_g before leaving the accelerating region, then it becomes 'trapped' and is accelerated for an extended length. Eventually, the electron out-runs the plasma wave and leaves the accelerating region. The distance travelled by the electron in this time is known as the dephasing length and this sets the maximum achievable energy for a non-evolving plasma wave.

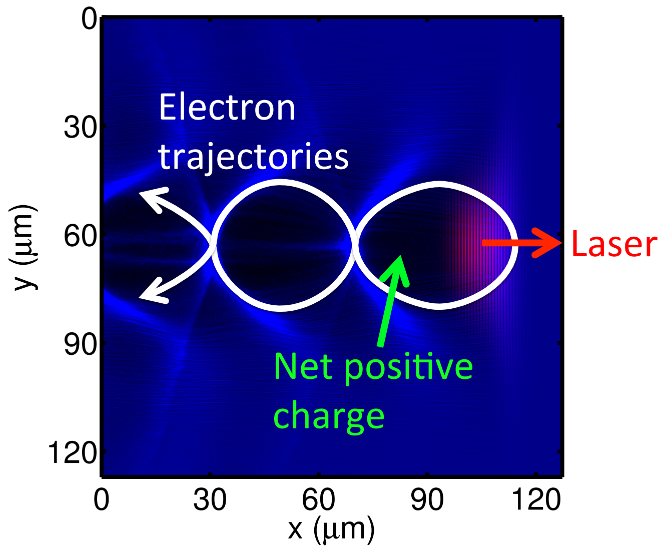

Figure 2.11: The laser pulse (shown in red) is moving towards the right hand side of the picture creating wave structure in the electron density (shown in blue). The trajectories of electrons (shown in white) that define the edges of the ion cavities show the transverse oscillation of the plasma at the plasma frequency.

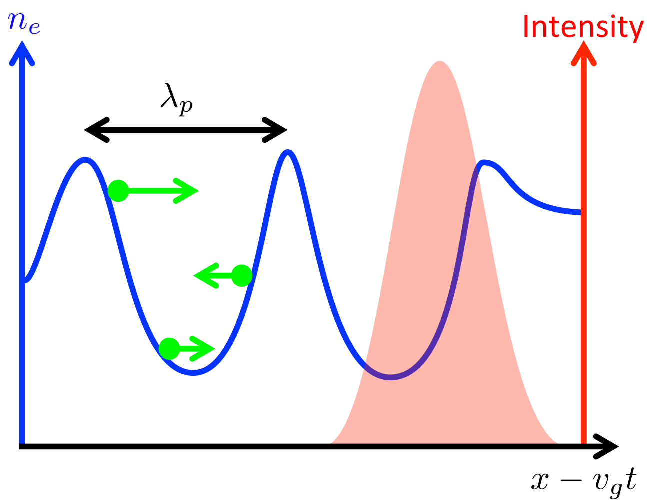

Figure 2.12: A cartoon of the electron density profile of a 1D plasma wave driven by a short laser pulse. The density perturbations cause longitudinal electrostatic fields, which accelerates electrons (shown in green) either in the forwards or backwards direction depending on their position in the wake. Electrons travelling in the accelerating region at close to v_g are accelerated over many plasma periods.

2.7.1 Analytical approximations

Plasma waves are made up of the oscillation of electrons in a constant uniform ion density background. For a 1D system where the order of electrons is preserved, i.e. no electron trajectories intersect, then the electric field experienced by an electron is given by Gauss' law as,

$$E_x = \frac{en_e D(x)}{\epsilon_0} \ , \tag{2.7.1}$$

where $D(x)$ is the displacement from the equilibrium position of an electron. The equation of motion is therefore,

$$\frac{\mathrm{d}^2}{\mathrm{d}t^2} D(x) = -{\omega_p}^2 D(x) \ . \tag{2.7.2}$$

where ${\omega_p}^2 = e^2 n_e/(m_e \epsilon_0)$. For a plasma wave set up by the propagation of a laser pulse the phase velocity of the wave is equal to the group velocity of the laser, i.e. $k_p = \omega_p/v_g$. Therefore, the solution to the equation **2.7.2** is of the form,

$$D(x) = A \sin(\omega_p t - k_p x) \ . \tag{2.7.3}$$

This derivation is valid as long as particles do not cross [Dawson59], i.e. $|\partial D/\partial x| < 1$, which gives a maximum amplitude of the particle displacements of $1/k_p$. For amplitudes greater than this, particle trajectories cross and the derivation is no longer valid. Such behaviour begins to destroy the wave and so this is commonly known as the wave-breaking limit, for which the maximum longitudinal electric field is (for a zero-temperature, non-relativistic plasma),

$$E_0 = \frac{\omega_p m_e c}{e} \ . \tag{2.7.4}$$

For a 3D system, electrons are also ejected radially, setting up a simultaneous radial plasma oscillation. This system can be solved in the linear case using cold fluid equations [Gorbunov87, Sprangle88, Esarey09] to give the plasma response,

$$\left(\frac{\partial^2}{\partial t^2} + {\omega_p}^2\right) \frac{\delta n_e}{n_0} = c^2 \nabla^2 \mathbf{a}^2/2 \ , \tag{2.7.5}$$

where δn_e is the perturbation to the background density and $\mathbf{a}$ is the normalised vector potential of the driving laser. The resulting electrostatic field (ϕ) is given by,

$$\left(\frac{\partial^2}{\partial t^2} + {\omega_p}^2\right) \phi = {\omega_p}^2 a^2/2 \ . \tag{2.7.6}$$

These equations only apply below the wave-breaking limit (equation **2.7.4**) and so do not accurately describe systems for which $a \geq 1$.

For larger amplitude plasma waves, the plasma wave becomes non-sinusoidal. Detailed analysis of this in 1D is provided in [Bulanov89,Sprangle90,Esarey09], leading to coupled equations that describe the plasma-response and the evolution of the laser pulse. It is seen that the length of the wake increases as the system becomes more non-linear, as given by,

$$\lambda_{Np} = \frac{2}{\pi}\frac{E_{\max}}{E_0}\lambda_p \; , \tag{2.7.7}$$

where $E_{\max}$ is the peak longitudinal electric field of the plasma wave. No analytical solution to a full 3D non-linear plasma wave has been found and so exploration of this regime has been through experiments and computer (PIC) simulations.

2.7.2 Blowout regime

2D and 3D PIC simulations of wakefields generated by short-pulse ultra-relativistic lasers reveal that the laser fully expels the electrons from the region of the pulse, creating an ion cavity [Pukhov02,Kostyukov04,Gordienko05,Lu07]. This is know as the 'blowout' or 'bubble' regime as the ion-cavity is seen to be spherical with a radius of,

$$R_b = 2\sqrt{a_0}\frac{c}{\omega_p} \; . \tag{2.7.8}$$

The plasma wave is highly non-linear in this regime and so wave-breaking is seen to destroy the wakefield after a few periods.

2.7.3 Electron injection and trapping

Electrons that persist in the accelerating field region of a plasma-wakefield obtain high energies very rapidly due to the large ($E_x > 10^{11}$ Vm^{-1}) longitudinal electric field. However, as the accelerating structure is travelling at approximately the group velocity of the laser ($v_g \approx c$), stationary electrons only experience the accelerating force for a short time $\sim \lambda_p/c$. Electrons that are injected into the accelerating structure with velocity close the phase velocity of the wakefield can become trapped by the longitudinal and transverse focusing fields and accelerated over many plasma wavelengths. This is possible by injecting an external electron beam into the wakefield or by self-injection of electrons from within the plasma.

For self-injection to occur, electrons must be travelling forwards at the phase velocity of the plasma wave (v_ϕ) by the time they reach the rear of the accelerating region of the wakefield. The trapping threshold, as derived from the electron trajectories around a spherical ion cavity, can be expressed as [Thomas10],

$$\frac{c\sqrt{\ln\left[2{\gamma_p}^2\right]-1}}{\omega_p R_b} \lesssim \frac{1}{2}\ , \tag{2.7.9}$$

where γ_p is the Lorentz factor of the phase velocity of the wakefield. Therefore, trapping occurs more easily at higher densities and for greater a_0. An initially hot plasma may also help trapping [Katsouleas88], as some of the background electrons have a forward momentum before entering the wakefield.

2.7.4 Guiding of laser pulses in underdense plasma

As described in section 2.1.2, the divergence angle of a focused laser pulse in vacuum can be approximated as,

$$\Theta_D = \frac{\sigma_r}{z_R}\ . \tag{2.7.10}$$

In order to maintain the electron acceleration process over distances greater than z_r, a radially dependent phase velocity is required to prevent the laser pulse from diverging. Generation of a focusing effect requires that the phase velocity increases with distance from the axis. This can occur due to a radial density profile and, in the case of relativistically intense pulses, a radial intensity profile. Both of these effects are naturally generated by the geometry of a focused laser pulse and the ponderomotive expulsion of electrons from the laser axis.

Relativistic self-focusing occurs for laser pulses with peak powers in excess of the critical power for relativistic self-focusing (see appendix **A.2**), given by,

$$P_{\text{crit}} \simeq 17\frac{n_c}{n_e}\ [\text{GW}]\ , \tag{2.7.11}$$

to a laser spot size given by,

$$\sigma_r = \frac{4\sqrt{2}}{a_0}\frac{c}{\omega_p}\ . \tag{2.7.12}$$

In some cases the laser is intense enough to completely expel all of the electrons from the laser axis to a distance known as the blowout radius [Sun87], given by,

$$R_b = 2\sqrt{a_0}\frac{c}{\omega_p}\ . \tag{2.7.13}$$

The guiding conditions then change as there is no focusing structure within R_b. The guided spot size is then $\sigma_r \approx R_b$.

2.7.5 Pump-depletion

The acceleration length in a laser-driven wakefield accelerator is limited by the distance over which the laser remains intense enough to drive the wake. As the laser propagates, it inevitably loses energy due to the diffraction of the leading edge of the pulse, and from the generation of the wakefield itself. Decker *et al.* [Decker96] calculate the energy lost in driving the wake (using the phenomenology observed in 1D PIC simulations), in order to derive a pulse-front etching model for pump-depletion, with an etching velocity of,

$$v_{\mathrm{etch}} = \frac{{\omega_p}^2}{{\omega_0}^2} c \, . \tag{2.7.14}$$

Therefore, the pulse front moves back through the laser pulse as it propagates, and the energy ahead of that front is depleted. This eventually reduces the intensity of the pulse so that it no longer drives a wakefield. Also, the phase velocity of the wake now moves at $v_g - v_{\mathrm{etch}}$. Further work to calculate pump depletion from the energy required to drive the transverse electron current [Shadwick09] arrives at an energy loss rate of,

$$\frac{1}{\mathcal{E}(0)} \frac{\partial \mathcal{E}(t)}{\partial t} = -\omega_p \frac{{k_p}^2}{{k_0}^2} \frac{{E_{\mathrm{max}}}^2}{{E_0}^2} \, , \tag{2.7.15}$$

where $\mathcal{E}$ is the pulse energy, E_{max} is the maximum longitudinal electric field amplitude of the wake and E_0 is the electric field at the wave-breaking limit.

2.7.6 Dephasing

Once a trapped electron begins accelerating in a wakefield, it begins to overtake the wakefield structure, which is limited to the laser group velocity. In the linear case once an electron has been accelerated over a distance of $v_g \lambda_p / [2(c - v_g)]$ then the electron leaves the accelerating region of the wakefield. This distance is known as the dephasing length. In the case of pulse front etching, this length is shortened due to the reduction in the phase velocity of the wakefield. For non-linear wake-fields or the blowout regime, the dephasing length is longer, as the accelerating structure is longer than λ_p.

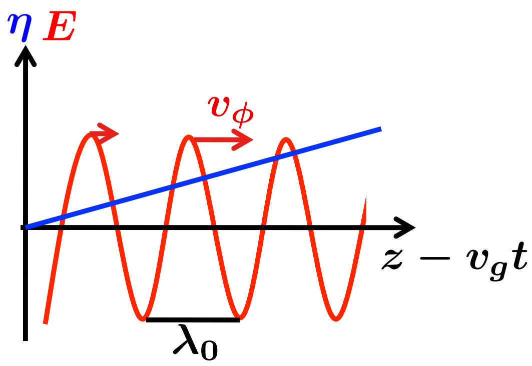

Figure 2.13: An electromagnetic wave co-moving with a refractive index gradient experiences a change in wavelength due to the longitudinal variation in phase velocity. In this case the phase velocity is greatest at the front, so that the radiation is red-shifted.

2.7.7 Photon acceleration and pulse compression

As the laser is co-moving with a longitudinal refractive index gradient, created by the electron density perturbation and the intensity gradients of the laser pulse, the pulse spectrum and temporal properties evolve as the laser propagates. The spectral modifications arise due to the longitudinal variation of the phase velocity over the length of the pulse, as shown in figure **2.13**.

Assuming that the refractive index is relatively constant over a laser wavelength then the rate at which the wavelength changes is,

$$\frac{\mathrm{d}\lambda}{\mathrm{d}t} = c\lambda \frac{\partial}{\partial z}\eta^{-1} \ , \tag{2.7.16}$$

and in terms of angular frequency this becomes,

$$\frac{\mathrm{d}\omega}{\mathrm{d}t} = -\omega \frac{\partial}{\partial t} \ln \eta \ . \tag{2.7.17}$$

The refractive index depends on the electron density and the relativistic effect of the ponderomotive force, so gradients in both density and intensity contribute to wavelength shifts. In a short pulse laser-driven wakefield red-shifting is seen to occur towards the front of the pulse and blue-shifting can occur near the rear [Wilks89, Schreiber10]. Also, as the plasma density at the rear of the pulse is much lower, the group velocity is closer to c than at the leading edge of the pulse. This results in pulse compression from the rear of the pulse, as illustrated in figure **2.14**.

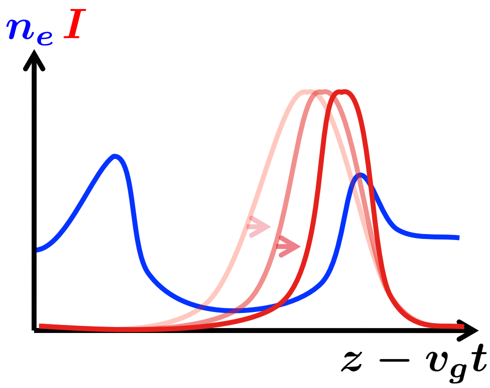

Figure 2.14: An illustration of pulse compression in a short-pulse laser-driven wakefield. The group velocity at the rear of the pulse is greater than at the leading edge, resulting in compression of the pulse.

Chapter 3

Methods

3.1 Astra-Gemini laser

The experimental work presented in this thesis was performed on the Astra-Gemini laser at the Central Laser Facility based at the Rutherford Appleton Laboratory. This is a dual-beam titanium-sapphire laser, which can produce up to 15 J in 40 fs pulses at a central wavelength of 800 nm. The laser can be fired every 20 seconds in full power mode, with CW and 10 Hz lasers available for alignment purposes. The final collimated beam diameter is 15 cm and focusing parabolic mirrors in the $f/1 - f/20$ range are available. The flexible experimental target area allows for a huge variety of gas and solid target experiments.

3.2 Frequency-resolved optical gating (FROG)

Frequency-resolved optical gating (FROG) is a diagnostic for measuring the intensity and phase of a laser pulse (for a good overview of the diagnostic see [Trebino00]). This provides the intensity profile of the pulse, and the instantaneous frequency. FROGs were originally used to diagnose laser systems such as oscillators, amplifiers, stretchers and compressors and allowed optimisation of pulse lengths in order to get the highest peak powers possible. They can also be used as diagnostics of laser-plasma interactions by tracking changes to the laser spectrum and temporal profile caused by the interaction.

The type of FROG used in this thesis is based on second harmonic generation in a birefringent crystal (SHG-FROG). This method is more sensitive than third-order devices, and also has a greater dynamic range, which is advantageous to measurements in laser-plasma experiments as the signal can be highly variable. Second harmonic generation is a non-linear optical process, in which a high intensity electromagnetic field affects the refractive index of the material through which it propagates. The material response to an electric field is termed as the polarisation density $\mathbf{P}$ (see section 2.1.4). The second harmonic term for a single pulse is given by,

$$E_{\mathrm{SHG}}(t) \propto E_1(t)^2 \exp\left[2i(\omega_1 t - \mathbf{k_1} \cdot \mathbf{r})\right] . \tag{3.2.1}$$

Crossing two waves, E_1 and E_2, in a material produces three second harmonics pulses, one for each pulse individually and the cross-correlations term, given by,

$$E_{\mathrm{C}}(t) \propto E_1(t)E_2(t) \exp\left[i((\omega_1 + \omega_2)t - (\mathbf{k_1} + \mathbf{k_2}) \cdot \mathbf{r})\right] . \tag{3.2.2}$$

For two identical input pulses, as created by splitting a single pulse with a partially reflecting mirror, then this cross-correlation term is know as the autocorrelation. This can be used as a diagnostic (an autocorrelator) to measure the duration of a laser pulse, by measuring the intensity of the autocorrelation term for a range of different time delays between the two pulses. The intensity will be greatest when the time delay is zero and will decrease for increasing time delay at a rate which is dependent on the temporal profile of the pulse. The pulse length can be retrieved from this information, if a particular pulse shape is assumed, i.e. a gaussian. By introducing a small angle between the two pulses, the same information can be collected on a single shot, as the delay between them is mapped onto the transverse dimension of the beams, as illustrated in figure **3.1**.

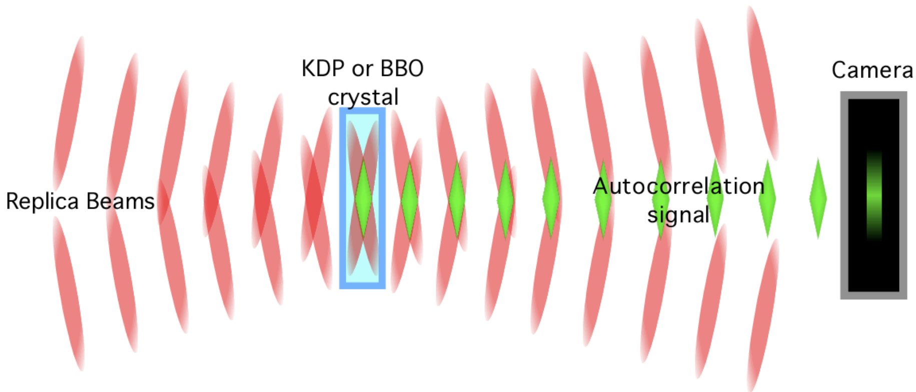

Figure 3.1: Schematic of the autocorrelation process.

For a FROG the autocorrelation is resolved spectrally, typically by placing a grating in the autocorrelation beam. The resulting image has the relative delay between the two replica pulses on one axis and the spectrum of the autocorrelated pulse on the other. Figure **3.2** shows the calculated FROG images for a 10 fs pulse with a flat phase and after propagation through fused silica. In this case the reflection and absorption are ignored, but the spectral phase is modified due to the wavelength dependent refractive index of the propagation medium. For most materials the dispersion is positive, i.e. it imparts a positive chirp on a pulse passing through it (longer wavelengths travel faster). However, plasma has a negative dispersion.

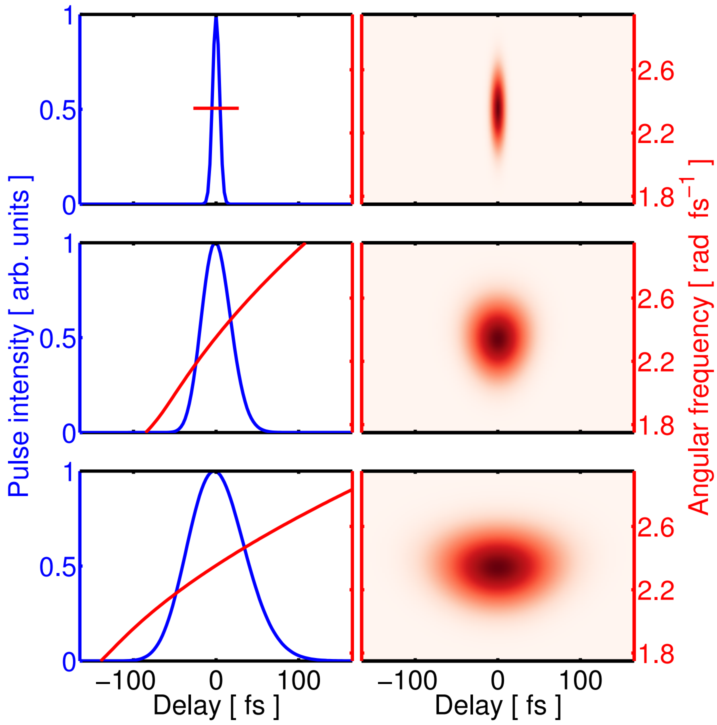

Figure 3.2: (Left) Temporal intensity profile (blue) and instantaneous frequency (red) and (Right) FROG traces of a 10 fs unchirped gaussian pulse (Top) and after numerical propagation through (Middle) 4 mm and (Bottom) 8 mm of fused silica glass.

For the SHG-FROG the equation that gives the FROG trace for a particular electric field $E(t)$ is given by,

$$I_{\mathrm{FROG}}(\omega,\tau) = \left| \int_{-\infty}^{\infty} E(t)E(t-\tau)\exp[-i\omega t]dt \right|^2, \tag{3.2.3}$$

where τ is the relative delay of the two pulses. As this is an autocorrelation, a positive delay gives the same result as a negative delay, so the SHG-FROG trace is always symmetrical about $\tau = 0$. There is no function which directly obtains the electric field from this image, so instead it is retrieved by guessing the electric field and comparing the calculated FROG image for the guess pulse to the measured image. This guess is then iteratively improved until the best fit is found, which gives the retrieved pulse.

Due to the mathematics of the diagnostic, carrier envelope phase of the pulse can not be retrieved. Also, equation **3.2.3** shows that $E(t)$ will give the same FROG trace as $E(-t)$, so the time direction can also not be directly found. However, this ambiguity can be resolved if an asymmetric time-dependent property of the pulse is known in advance, such as the chirp of the pulse [Schreiber10].

3.2.1 FROG retrieval algorithm

The comparison of a calculated FROG trace to a measured FROG trace is quantified by the FROG error,

$$G^{(k)} = \sqrt{\frac{1}{N^2}\sum_{i,j=1}^{N}\left|I_{\text{FROG}}(\omega_i,\tau_j) - \mu^{(k)} I^{(k)}_{\text{FROG}}(\omega_i,\tau_j)\right|^2}\ , \tag{3.2.4}$$

where I_{FROG} is the measured FROG image, $I^{(k)}_{\text{FROG}}$ is the calculated FROG image for the k^{th} guess electric field, N^2 is the number of pixels in each image (both images must be square and have the same size) and $\mu^{(k)}$ is the scalar which minimises the error of the k^{th} guess field.

By calculating the error $G^{(k)}$ for a large number of possible electric fields, an accurate reconstruction of the actual electric field can be made. In practice, there are several processes by which a guess can be modified using the experimental data in order to get an improved guess. The ones used in the program FROGed, written for the analysis in this thesis, are outlined in the following sections.

3.2.1.1 Data and mathematical constraints

The signal field for an SHG FROG is defined as,

$$E_{\text{sig}}(t,\tau) = E(t)E(t-\tau)\ . \tag{3.2.5}$$

The data constraint, contained in equation **3.2.3**, dictates that the magnitude of the Fourier Transform of this quantity must be equal to the square root of the measured FROG trace. Therefore, the signal field for a particular guess electric field can be modified to comply with the data constraint,

$$\tilde{E}_{\mathrm{sig}}^{(k+1)}(\omega,\tau) = \frac{\tilde{E}_{\mathrm{sig}}^{(k)}(\omega,\tau)}{\left|\tilde{E}_{\mathrm{sig}}^{(k)}(\omega,\tau)\right|}\sqrt{I_{\mathrm{FROG}}}\ . \tag{3.2.6}$$

The phase is unchanged by this operation so it is extremely unlikely to be the correct solution. However, a new guess field can be calculated from the signal field in the time domain using the mathematical constraint given by,

$$E^{(k+1)}(t) = \int_{-\infty}^{\infty} E_{\mathrm{sig}}^{(k+1)}(t,\tau)d\tau\ . \tag{3.2.7}$$

Iteratively repeating this process will converge very quickly towards to the electric field responsible for the measured FROG trace in the majority of cases but will not usually produce a good final result by itself except for the simplest of pulses. Consequently, the first iterations of FROGed are always using these basic constraints to quickly arrive at an approximate solution.

3.2.1.2 Generalised projections

The generalised projections method (GP) also solves the data and mathematical constraints but with an additional requirement that the guess field is modified as little as possible when complying with each constraint. For the data constraint function this is achieved in the same way as described above but for the mathematical constraint it is necessary to minimise the function,

$$Z = \sum_{i,j=1}^{N} \left|E_{\mathrm{sig}}^{(k+1)}(t_i,\tau_j) - E^{(k)}(t_i)E^{(k)}(t_i-\tau_j)\right|^2\ . \tag{3.2.8}$$

This can be achieved by following the negative gradient of Z to find the electric field which minimises Z. This minimisation is computationally intensive, so instead the power method principle component GP algorithm, as developed in [Kane97] [Kane98], is used. In the majority of cases the GP algorithm is sufficient to obtain an excellent retrieval. However, purely running a GP algorithm is likely to stagnate at a local minimum, so beginning the algorithm from different initial guesses will help to find a solution closer to the global minimum.

3.2.1.3 Genetic algorithm

A genetic algorithm (GA) attempts to retrieve an unknown answer to a problem by pure 'trial and error'. It starts with a population of proposed guess solutions and quantifies the fitness of each, i.e. how well it fits the measured data. It then produces a second generation of guesses by combining features from the previous set and adding some random variations. This approach mimics how evolution creates solutions to problems in nature and can produce good results in a surprisingly short number of generations. It also has the advantage that very little about the system has to be known in advance, as long as there is a way to assess the quality of each individual. The main approaches to generating a new generation of potential solutions are as follows:

1. Breeding: Two solutions from one generation are combined to create a new solution. This is done by randomly selecting 50% of values from each parent solution and combining them into the offspring solution. The parents can be selected at random, or preferentially from those with a high level of fitness. This process takes the diversity between the existing solutions and creates new combinations, which will converge to the optimum arrangement of the parts of the initial solutions.

2. Mutation: Single individuals can be subjected to some random changes to elements. This provides new elements for potential solutions which can lead to the fortuitous discovery of elements of the optimal solution.

Each generation maintains at least the best solution from the previous generation so that the best solution is always preserved and each generation has the potential to create a better solution. It is also important to keep a high level of variation within each generation of solutions so that there is a large potential for generating novel solutions at each iteration. This can be controlled by specifying what processes to use in generating new solutions. Preferentially using the best solutions for breeding for the next generation increases the number of solutions which are close to optimal, which are the most likely to produce an improved solution. Increasing the number and strength of mutations increases the variation within each generation, which increases the likelihood of finding new solutions. Therefore, it is important to balance both of these parameters for optimal convergence of the genetic algorithm.

Monitoring minimum, maximum and average fitness of each generation of solutions gives an indication of how well the algorithm is performing, as shown in figure **3.3**. In this case the population of solutions all quickly converged to the same solution and progress stalled. The GA control program then increased the proportion of produced solutions

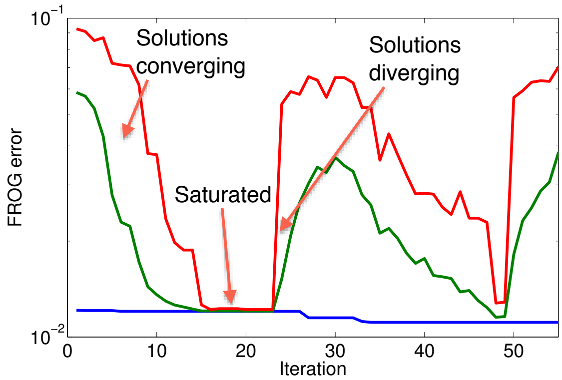

Figure 3.3: Example plot of the minimum (blue), maximum (red) and average (green) FROG errors of the solutions in each generation of a genetic algorithm.

that contained random mutations, and reduced the number of solutions that took values from the best solutions. This resulted in an increase in diversity of the solutions, so that the GA could again make progress. As the average FROG error increased above a threshold value, relative to the minimum error, these changes are reversed and the average error reduces again. This control logic is important to stop the GA saturating or diverging after a few iterations.

3.2.1.4 Algorithm control

Each retrieval algorithm is capable of reducing the FROG error, but they do so at different speeds and efficiencies. In addition, each algorithm alone is prone to stagnation at local minima. For these reasons, a program that switches between the different algorithms with varying initial conditions will produce better results than any one method running in isolation. In FROGed, the basic data constraint algorithm is utilised first, as it is the quickest and normally produces a good approximation from a random starting point. The generalised projections method is slower but is capable of finding a much more accurate solution and so it uses the best solution found by the data constraint algorithm as the starting point. The algorithms are switched when each method stagnates, i.e. no significant progress of the FROG error value for a given number of iterations. After a few attempts with each method, the algorithm switches to the genetic algorithm, which is the slowest but can find much better solutions away from a local minima. An example of the progress of FROGed is shown in figure **3.4**.

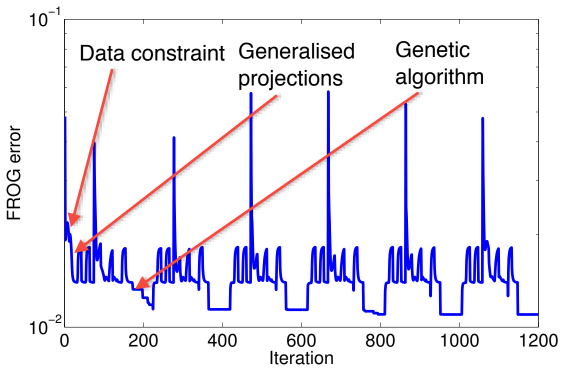

Figure 3.4: Example plot of the progress of the FROG error showing the switch between algorithms.

3.2.1.5 Data gridding

The FROG pulse retrieval algorithms use fast Fourier Transforms (FFT) for the various calculations and this requires that the temporal axis and the frequency axis are related by,

$$d\omega = \frac{2\pi}{Ndt} \,. \tag{3.2.9}$$

Therefore the FROG trace needs to be remapped so that the dispersion axis is linear in ω. It then must be resized into an $N \times N$ grid that satisfies equation **3.2.9** and which is large enough to contain the data. The size of the grid required depends on the complexity of the measured pulse, with more complex pulses requiring a larger grid, due to their large time-bandwidth product. The grid size is limited to values of $N = 2^n$, where n is an integer, for which the FFT routine is optimal.

It is also vitally important to set $t = 0$ on the delay axis for the correct pixel, to avoid errors in the pulse length. In an ideal case, this corresponds to the image maximum and also the centre of weight of the image. However, in the presence of detector noise or intensity asymmetries this will not be the case, so the image centre must be selected as the mirror axis of the image as shown in figure **3.5**.

3.2.2 Retrieved pulse analysis

The final FROG error achieved by the retrieval process is indicative of the confidence levels of the retrieved pulse, and values of 0.02 or less (as given by equation **3.2.4**) were found to correlate with good retrievals. However, if an overly large grid size is used lots of

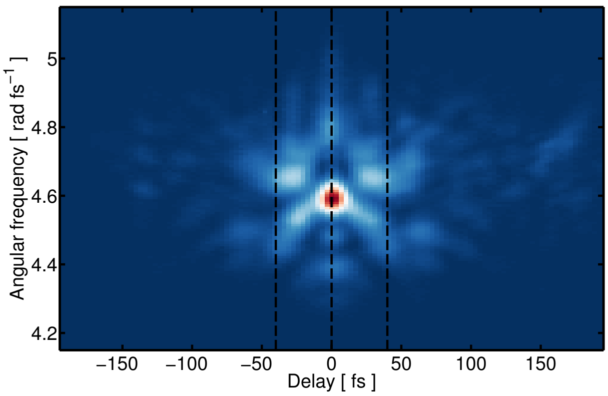

Figure 3.5: Example of an experimental FROG trace centred on a 256 × 256 grid with lines at $t = -40, -0$ and 40 fs to aid selection of the mirror axis.

cells will have a value of zero far away from the actual signal. This creates an artificially low error, as a large variety of erroneous pulses could satisfy this requirement. Also intensity variations in some regions of the image, or a low dynamic range of the image can result in a high FROG error for an apparently good retrieval. For this reason, each image is also assessed individually to determine if (for a FROG error which is close to 0.02) the measurement should be included or rejected in the analysis. Example retrieval images are shown in figure **3.6**. The top row is an example of a relatively large numerical error for a good retrieval. Here, the numerical error is increased due to the noisy image with a beam imperfection. The middle row shows a good retrieval with a low error. The bottom image has a good numerical error but the retrieval was badly affected by a non-symmetric measured FROG and needs to be discarded. Asymmetries can occur due to spatial variations in the input beam, leading to an erroneous FROG trace.

Once the pulse retrievals are obtained, there remains the time-direction ambiguity which is unavoidable in an SHG-FROG. This ambiguity can only be removed by applying some outside knowledge of the pulse shape. For example, if there is sufficient glass in the optical path before the FROG diagnostic then the pulse must be positively chirped. Knowing this, the potential solution with a negative chirp can be discarded. Another method, developed during the work for this thesis, employed two separate FROGs with different optical path lengths. The correct retrievals for each FROG must therefore have a relative difference in chirp which is equal to that caused by the optical path difference.

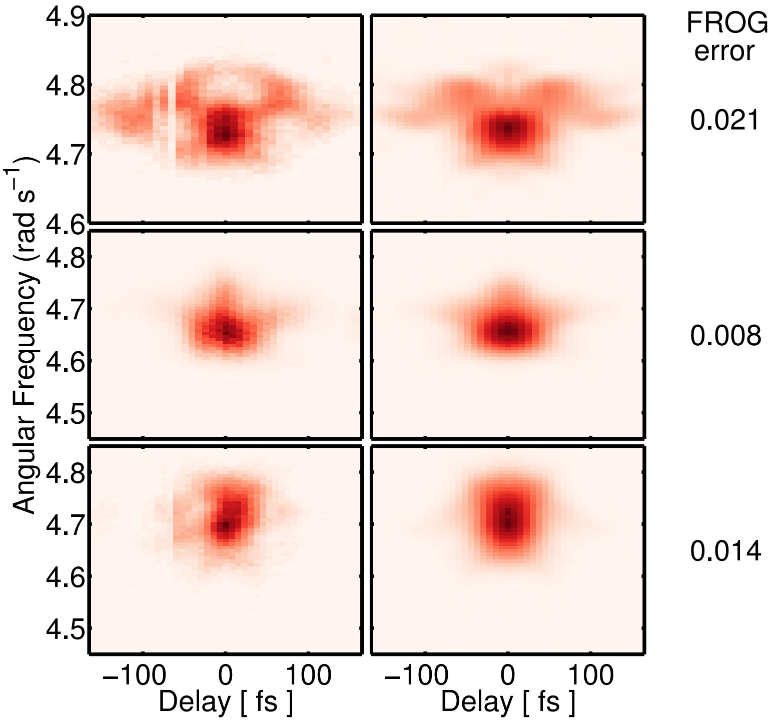

Figure 3.6: (Left) Measured FROG traces and (right) FROG traces calculated from the retrieved pulses. The FROG error for the retrieval is shown to the right of each row.

3.2.3 FROG calibration

The electric field of two identical pulses separated in time by Δt is given by,

$$E(t) = E_0 \exp\left[-\frac{(t-\Delta t/2)^2}{2{\sigma_t}^2}\right] \exp\left[i\omega_0(t-\Delta t/2)\right] + E_0 \exp\left[-\frac{(t+\Delta t/2)^2}{2{\sigma_t}^2}\right] \exp\left[i\omega_0(t+\Delta t/2)\right] . \tag{3.2.10}$$

The Fourier Transform of this field has the form,

$$E(\omega) = \sqrt{S(\omega)} \exp\left[i\omega\frac{\Delta t}{2}\right] \exp[\phi(\omega)] . \tag{3.2.11}$$

The spectrum of the two pulses, given by $|E(\omega)|^2$ will have an envelope of $S(\omega)$, which is modulated with peaks separated by $\Delta\omega = 2\pi/\Delta t$.

The SHG-FROG used to obtain the results presented in chapters **4** and **5** was calibrated using a double pulse generated by an interferometer. The measured spectrum shown in figure **3.7** shows a spectral intensity oscillation at $\Delta\omega = 0.03$ rad fs^{-1}, indicating a pulse separation of $\Delta t = 209$ fs. This gives the calibration of the temporal and spectral axes of the FROG by measuring the peak separation in the image (figure **3.7**).

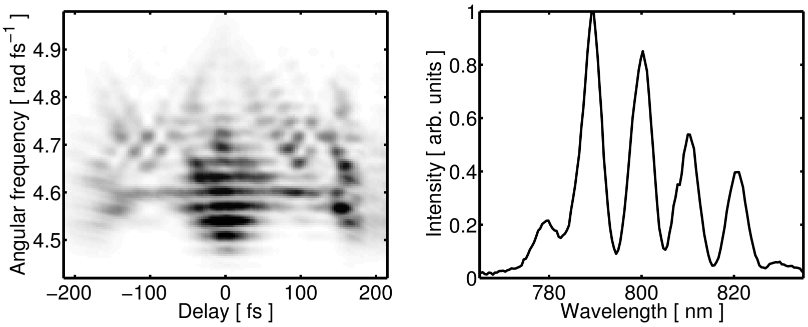

Figure 3.7: (left) FROG trace and (right) spectrum of a double pulse generated with an interferometer. The spectrum is used to calculate the pulse separation and then calibrate the FROG image.

3.3 Plasma mirrors

Plasma mirrors have been successfully used to temporally filter ultra-short laser pulses [Kapteyn91,Gold94]. In this interaction, a flat glass optic which has been coated with an anti-reflection ($R < 1\%$) coating is illuminated by the laser beam with a peak intensity which is higher than the ionisation threshold. The optic is therefore transparent to any laser energy which arrives prior to the peak of the pulse but then is highly reflective once the ionisation threshold is reached. This enhances the contrast ratio of the reflected pulse and allows solid density interactions at higher intensities with a much reduced scale length.

Figure **3.8** shows how a plasma mirror results in a reflected laser pulse with a better contrast than the input pulse. For optimal operation, the peak intensity must be tuned (by defocusing on the mirror) such that the reflectivity of the main pulse is high, while gating out the energy preceding that pulse. Increasing the intensity beyond this point can actually reduce the reflectivity and the focusability of the beam, due to the creation of a large scale-length plasma [Ziener03].

Plasma mirrors were used for the solid-target experiments described in chapters 5-6 to increase the contrast of the Astra-Gemini laser from $\approx 10^6$ to $\approx 10^{10}$. In this set-up the beam was focused with an off-axis $f/7$ parabolic mirror onto two anti-reflection coated glass blocks, such that the the focus was between them. The beam was then collimated

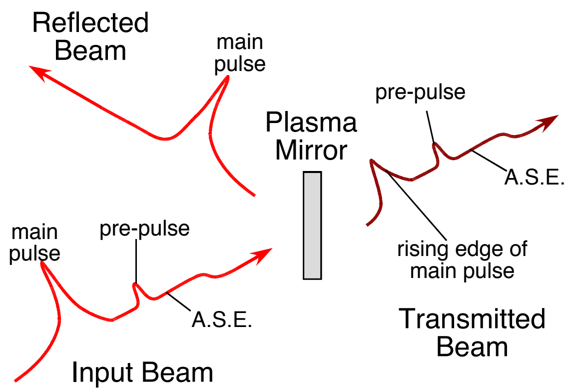

Figure 3.8: Illustration of the operation of a plasma mirror

by an identical parabolic mirror. This reduced the available energy of the laser by 50% but allowed high-intensity interactions with unperturbed targets.

3.4 Particle-in-cell simulations

Simulations included in this thesis were performed using OSIRIS [Fonseca02] and EPOCH [Brady11], both fully relativistic, three-dimensional, parallel particle-in-cell (PIC) codes. For the main simulations performed here, the codes were operated in a cartesian 2D3V mode for which a 2D spatial grid was used but with fields and velocities defined in 3D. This is physically equivalent to having infinite and uniform plasma and fields in the unused third physical dimension. Some simulations were also performed in 1D3V, mainly for convergence testing. Ionisation was not simulated, so it was necessary to specify initial ion and electron densities and charge-to-mass ratios which appropriately represented the expected ionisation states in the simulated experiment. The simulations were performed on the cx1 cluster based at the High Performance Computing service at Imperial College London. This cluster allows simulations to be performed on up to 72 nodes for up to 72 hours per job.

3.4.1 Spatial and temporal resolution

The numerical methods used in the PIC codes require that the cell size, Δx, and the time step, Δt, comply with the Courant condition which for a 2D grid is $c^2\Delta t^2 < \Delta x^2 + \Delta y^2$. For a square grid ($\Delta x = \Delta y$) this leads to $c\Delta t < \Delta x/\sqrt{2}$. Also the accuracy to which plane waves can be reproduced is characterised by [Birdsall91],

$$\left(\frac{\sin\frac{\omega\Delta t}{2}}{c\Delta t}\right)^2 = \left(\frac{\sin\frac{k_x\Delta x}{2}}{\Delta x}\right)^2 + \left(\frac{\sin\frac{k_y\Delta y}{2}}{\Delta y}\right)^2 . \tag{3.4.1}$$

In effect this modifies the vacuum dispersion relation and results in the group and phase velocities of an electromagnetic wave differing from c. This becomes of critical importance for simulations of underdense laser-plasma interactions, specifically laser-wakefield accelerators where the group velocity of the laser is critically important (see appendix **A.3**). It is also important to have sufficiently small cell size to resolve important parameters such as the plasma skin depth and, in the case of ultra-thin targets, the target thickness.

3.4.2 Calculating the space charge fields

In order to measure the simulated laser field in the presence of plasma it is necessary to remove the space charge contribution to the electric field. This can be calculated from the charge density distribution (ρ), using the definition,

$$\nabla \cdot \mathbf{E} = -\nabla \cdot \nabla\phi = \frac{\rho}{\epsilon_0} , \tag{3.4.2}$$

and the differential property of Fourier Transforms,

$$\mathcal{F}\left[\frac{\mathrm{d}^2\phi}{\mathrm{d}x^2} + \frac{\mathrm{d}^2\phi}{\mathrm{d}y^2}\right] = \mathcal{F}\left[\frac{\mathrm{d}^2\phi}{\mathrm{d}x^2}\right] + \mathcal{F}\left[\frac{\mathrm{d}^2\phi}{\mathrm{d}y^2}\right] = -{k_x}^2\mathcal{F}\left[\phi\right] - {k_y}^2\mathcal{F}\left[\phi\right] . \tag{3.4.3}$$

Taking the Fourier Transform of equation **3.4.2** gives,

$$\phi = \mathcal{F}^{-1}\left[\frac{1}{({k_x}^2 + {k_y}^2)\epsilon_0}\mathcal{F}\left(\rho\right)\right] . \tag{3.4.4}$$

Therefore the electrostatic field is is,

$$\mathbf{E} = -\nabla\left(\mathcal{F}^{-1}\left[\frac{1}{({k_x}^2 + {k_y}^2)\epsilon_0}\mathcal{F}(\rho)\right]\right) . \tag{3.4.5}$$

3.4.3 Computing peak a_0 from experimental parameters

Full representation of experimental laser pulses can be quite challenging due to the difficulty of accurate measurements and the complexity of real laser pulses. For the simulations in this thesis, the laser pulse at the focus in vacuum is approximated as a gaussian function of intensity in time and spot radius as described by,

$$I(t,r) = I_0 \exp\left(-\frac{t^2}{{\sigma_t}^2}\right) \exp\left(-\frac{r^2}{{\sigma_r}^2}\right) , \tag{3.4.6}$$

where I_0 is the peak intensity, t is time and r is the distance from the centre of the focal spot. The standard deviations of the gaussian functions are defined as,

$$\sigma_t = \frac{t_{\text{FWHM}}}{2\sqrt{\ln(2)}} , \qquad \sigma_r = \frac{r_{\text{HWHM}}}{\sqrt{\ln(2)}} , \tag{3.4.7}$$

where t_{FWHM} is the temporal FWHM of the pulse and r_{HWHM} is the lateral radius at which the flux drops to half of the peak value. The energy in the pulse is then given by the integral of $I(t,r)$ over all time and space as,

$$\begin{aligned} \mathcal{E} &= \int_0^{\infty} \int_{-\infty}^{\infty} \int_0^{2\pi} I(r,t)\, d\theta\, dt\, dr , \\ \mathcal{E} &= \left(\frac{\pi}{\ln(2)}\right)^{\frac{3}{2}} \frac{I_0}{2}\, t_{\text{FWHM}}\, {r_{\text{HWHM}}}^2 . \end{aligned} \tag{3.4.8}$$

The experimentally measured values are generally $\mathcal{E}$, t_{FWHM} and r_{HWHM} so the peak intensity is given by,

$$I_0 = \left(\frac{\ln(2)}{\pi}\right)^{\frac{3}{2}} \frac{2\mathcal{E}}{t_{\text{FWHM}}\, {r_{\text{HWHM}}}^2} . \tag{3.4.9}$$

A perfectly uniform beam with a circular cross section will produce an Airy disc pattern at focus which is well approximated by a gaussian as shown in section 2.1.2. However, a real laser beam will have non-uniformities and phase errors in the beam profile which will increase r_{HWHM} and result in more laser energy at a large distance from the centre of the focal spot. So the actual peak intensity for a given r_{HWHM} can be significantly lower than calculated from equation **3.4.9**. The fraction of the energy in r_{HWHM} for an ideal gaussian is,

$$\frac{\mathcal{E}_{\text{FWHM}}}{\mathcal{E}} = \frac{2\pi \int_0^{r_{\text{HWHM}}} r \exp\left(\frac{r^2}{2\sigma_r^2}\right) dr}{2\pi \int_0^{\infty} r \exp\left(\frac{r^2}{2\sigma_r^2}\right) dr} = 0.5 \tag{3.4.10}$$

The reduction in intensity for extra energy outside of the focal spot can then be accounted for by multiplying the total pulse energy by the measured energy inside r_{HWHM} divided by 0.5 when calculating equation **3.4.9**. For example for a 10 J pulse with 35 % of the energy in r_{HWHM}, equation **3.4.9** would be calculated for $\mathcal{E} = 7$ J.

Chapter 4

Non-Linear Plasma Optics in a GeV Laser Wakefield Accelerator

Understanding self-guiding and propagation of laser pulses in underdense plasmas is critical to optimising laser-driven electron beams. Particularly the accelerating fields in the laser wakefield are highly dependent on the pulse intensity so it is important to demonstrate that high intensities can be maintained over the interaction length. Fortunately, the radial refractive index profile, that is a direct result of the radial intensity variation of a focused laser beam, creates a focusing 'lens'. This effect, known as relativistic self focusing, is capable of maintaining the beam waist over many Rayleigh lengths leading to acceleration of electron beams to GeV energy levels [Karsch07, Kneip09, Clayton10, Lu11]. A further obstacle to acceleration over many centimetres of plasma is laser beam depletion. As the beam energy is coupled to the plasma wave, energy is inevitably lost from the pulse reducing the strength of the generated wakefield. However, the longitudinal refractive index gradients co-moving with the laser pulse can cause pulse compression [Gordon03, Faure05, Schreiber10] leading to an intensity increase with propagation distance. This can also have a crucial effect on self-injection of background electrons into the accelerating structure [Hidding06].

This chapter presents experimental measurements of laser guiding, energy depletion and pulse compression from a laser-driven wakefield acceleration experiment with a 200 TW laser. Analysis of these results along with analytical and numerical modelling provides insight into the observed electron beam energies and properties, as well as opportunities for further optimisation of the process.

4.1 Experimental setup

An experiment was performed using the Astra Gemini Laser in the Central Laser Facility at the Rutherford Appleton Laboratory. The laser was focused into a gas target to create a plasma wakefield and the transmitted pulses were characterised spatially and temporally as shown in figure **4.1**. Each input pulse contained ≈ 12 J with a duration of

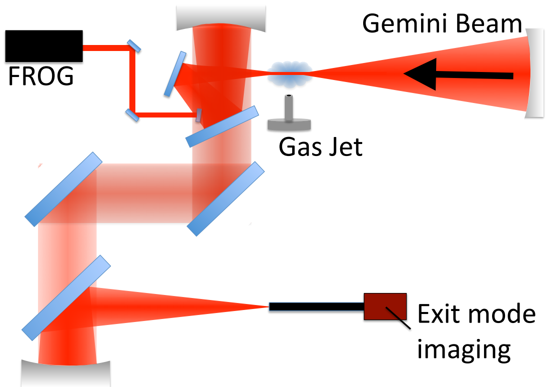

Figure 4.1: Experimental setup showing the optical diagnostics.

≈ 55 fs (FWHM) at a central wavelength of 800 nm. An $f/20$ off-axis parabolic mirror was used to create a 22 μm (FWHM) diameter focal spot containing $\approx 35\%$ of the total pulse energy. Super-sonic gas nozzles with diameters of 5, 10 and 15 mm were used to create a region of helium gas which, when fully ionised, produced a plasma electron density up to $n_e = 1.5 \times 10^{19}$ cm^{-3}. The gas profile resulted in a density plateau region in the middle of each nozzle with approximately linear density ramps down to zero at the nozzle diameter. The diameters of the plateau regions were 4, 8 and 11 mm respectively [Kneip10]. An $f/10$ spherical mirror allowed imaging of the exit plane of the gas jet. The imaging system had a resolution limit of 10 μm and a field of view of 902×675 μm. The integrated energy of the transmitted beam was measured by integrating the counts on the camera and cross-calibrated with an energy diode. Also a 5 mm diameter area near the centre of the transmitted beam ($\approx 1/50^{\text{th}}$ of the full beam diameter) was directed into a Grenouille (Swamp Optics) SHG-FROG (second harmonic generation - frequency resolved optical gating). This device produced a spectrally dispersed auto-correlation of the pulse from which the complete temporal intensity and phase information of the pulse was retrieved (see section 3.2.1). A magnetic electron spectrometer was used to measure the spectrum of the accelerated electron beam in the $100 - 1400$ MeV range.

4.2 Exit mode imaging

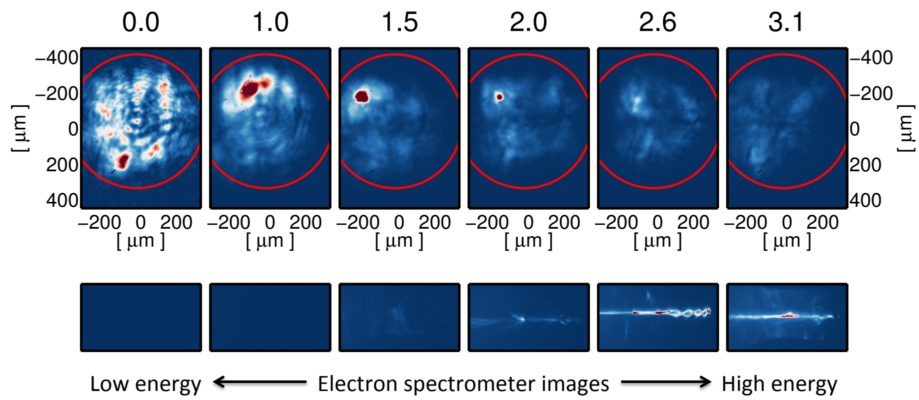

Figure 4.2: (Top) Spatial distribution of the transmitted laser pulse showing the vacuum beam size (red circle) and (Bottom) spectrometer screens showing the accelerated electrons (high energy to the right). The electron densities given above each pair of images are in units of 10^{18} cm^{-3}. The colour tables for each density are the same to allow easy comparison.

Sample images from the exit mode imaging for a 15 mm diameter gas nozzle are shown in figure **4.2** along with the corresponding images from the electron spectrometer. The exit mode imaging indicates that a significant fraction of the laser energy is trapped in the guided central channel for $n_e > 1 \times 10^{18}$ cm^{-3}. As the density is increased further, less energy remains in the guided spot as it is coupled into the plasma. This coincides with a substantial increase in electron energy and flux indicating that self-injection has occurred. The pulse energy observed outside of the guided spot was relatively constant at all densities.

4.2.1 Guided spot size

The exit mode imaging shows that for n_e = 1–2.5 $\times$ 10^{18} cm^{-3} there is a bright spot in the transmitted laser beam, which is the main guided filament of the laser. The lateral extent of a relativistically self-guided laser pulse can be calculated by balancing the natural diffraction of a focused laser with the relativistic self-guiding effect of the plasma. In this way the guided spot size (assuming a gaussian radial profile) is given by,

$$\sigma_r = \frac{4\sqrt{2}}{a_0}\frac{c}{\omega_p} \,, \tag{4.2.1}$$

when the laser power exceeds the critical power given by,

$$P_c \approx 17 \left(\frac{\omega_0}{\omega_p}\right)^2 \text{ [GW]} . \tag{4.2.2}$$

The critical power was exceeded for $n_e > 0.2 \times 10^{18}$ cm^{-3}, indicating that all shots should show evidence of self-guiding. For very strong wakefields, where $\delta n_e/n_e \sim 1$, the electron density drops to zero to a radius given by the blowout radius [Lu06],

$$R_b \approx \frac{2c\sqrt{a_0}}{\omega_p} . \tag{4.2.3}$$

In this case the laser pulse will be guided by the edges of the cavity, i.e $\sigma_r \approx R_b$. Clear guiding was only observed for $n_e > 1 \times 10^{18}$ cm^{-3} for which $P_c = 30$ TW. At this density, the guided spot size $\sigma_r = 10$ μm and the blowout radius $R_b = 18$ μm compared to the vacuum focus of the laser pulse for which the $1/e^2$ radius $\sigma_r = 19$ μm. For $n_e > 3 \times 10^{18}$ cm^{-3} the guided filament is seen to disappear from the exit mode imaging, due to depletion of the guided pulse.

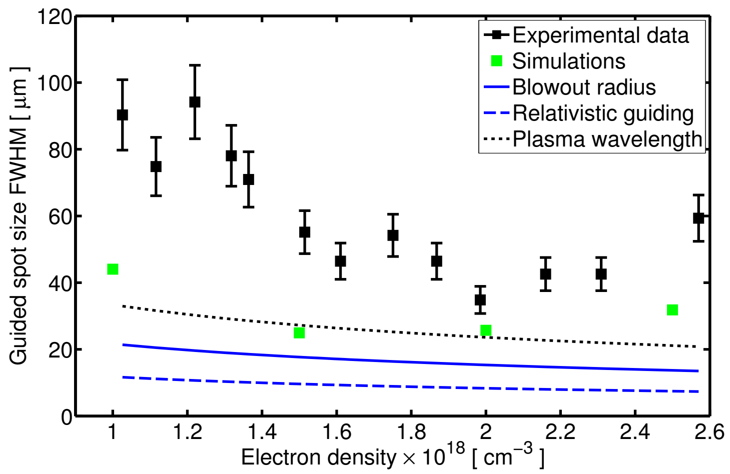

Figure 4.3: A graph showing the transverse FWHM size of the guided laser pulse after 15 mm of plasma from the experimental and simulation results. The data points are grouped with a bin width of 10^{17} cm^{-3} and the error bars are the average RMS variation of the binned data points. The blowout radius (solid blue line) and relativistic self-guided (dashed blue line) spot sizes are calculated from equations **4.2.1** and **4.2.3** respectively for $a_0 = 3$.

Figure **4.3** shows how the experimentally observed guided spot size varied with plasma density in the observable density range. The experimental and simulation results both show a larger spot size than calculated by either model. This could be due to a decrease in the plasma density towards the rear of the target, near the plasma boundary, as in this region the pulse will begin to diffract. Also, aberrations in the laser focal spot, leading to a non-gaussian input beam, may have adverse effects on the guiding effect. Previous work by Thomas [Thomas07] saw guiding of laser spot sizes of the order of plasma wavelength for a propagation distance of 2 mm.

4.2.2 Transmitted laser energy measurements

The transmitted laser energy is plotted in figure **4.4** as well as the peak electron energy observed on the electron spectrometer (the highest energy point which the electron signal is observable above the background). This shows that the laser pulse is more strongly depleted as the density is increased. A rapid decrease in transmitted laser energy is observed in the density region where acceleration of electron beams begins to occur, as more energy is coupled to the wake and into the accelerated electron beam. For $n_e > 3 \times 10^{18}$ cm^{-3}, only the unguided fraction of the laser energy remains, corresponding to $\approx$ 15% of the input laser energy. This energy in the unguided region was seen to be weakly linearly dependent on density, increasing to $\approx$ 20% for $n_e = 1 \times 10^{18}$ cm^{-3}.

Decker et al. [Decker96] calculate the pump depletion rate (see section 2.7.5) as due to a density dependent pulse front etching velocity given by

$$v_{\mathrm{etch}} = c\frac{{\omega_p}^2}{{\omega_0}^2} \; . \tag{4.2.4}$$

The energy of the photons in the etched region of the laser pulse is transmitted to the wakefield and so the laser energy is absorbed as the pulse propagates. The transmitted energy after 15 mm of propagation can be calculated by assuming the measured Gemini pulse profile (see section 4.3) enters the plasma and starts to be etched from a point on the leading edge of the pulse. The point on the leading edge t_{etch} can be taken as the point on the rising edge where the power equals some threshold value P_{etch}. This is plotted as the solid grey line in figure **4.4** for P_{etch} taken as $1/e$ of the peak power. This gives a reasonable agreement with the experimental data, but the value is a relatively arbitrary choice for a non-gaussian pulse shape. Alternatively, a more physical value can be taken, such as the critical power for relativistic self-focusing (P_c), which varies with plasma density. In this case, no pulse depletion is seen with this model for $n_e < 0.2 \times 10^{18}$ cm^{-3} as the peak power of the pulse is less than P_c for these densities. The results of this model is plotted as the dashed black line in figure **4.4** and significantly underestimates the laser absorption for $n_e > 1.5 \times 10^{18}$ cm^{-3}.

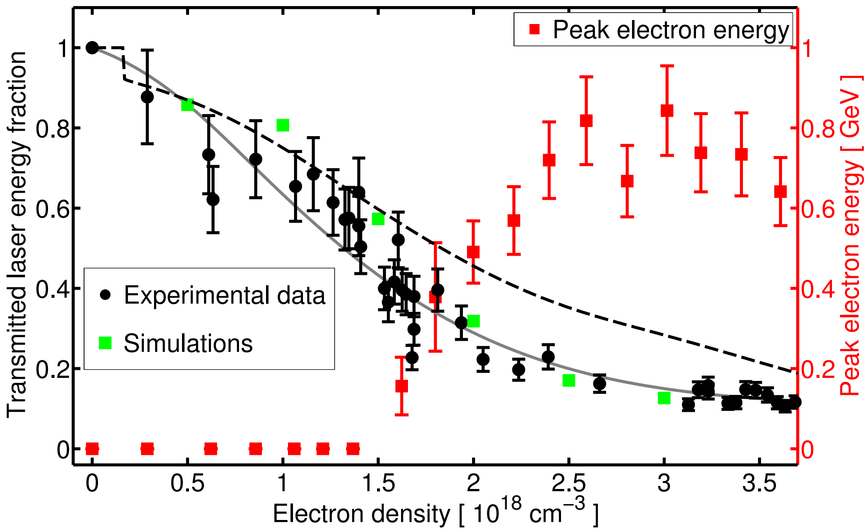

Figure 4.4: Transmitted pulse energy (black circles) and peak electron energy (red squares) as a function of gas electron density. The experimental data points are grouped with a bin width of 10^{17} cm^{-3} and the error bars are the average RMS variation of the binned data points. Also shown are the transmitted energy calculated from OSIRIS simulations (green diamonds). The calculated energy depletion rates, based of the Decker pulse front etching model [Decker96], are plotted for t_0 equal to the point on the leading edge of the pulse at which the power is $1/e$ of the peak (solid grey line) and greater than the critical power for self-focusing (dashed black line).

Slightly changing the threshold conditions such that $P_{\text{etch}} = mP_c$, where m is a fitting parameter, allows a much better fit to be achieved for $m = 1.8$, as shown in figure **4.5**. A lower value of m fits less well at high densities, and a higher value fits less well at lower densities. It is perhaps counterintuitive that a higher threshold value P_{etch}, for a given electron density, generally results in greater absorption. However, as the pulse shape has a slow rising edge, a lower P_{etch} causes a lower power region of the pulse to be etched away, resulting in higher transmission. This Gemini pulse shape and the etched region (shaded grey) is shown in figure **4.6** for $n_e = 2.5 \times 10^{18}$ cm^{-3} and various values of m.

It is also possible with this model for the transmission to increase with increasing density, as shown with the dashed line for $P_{\text{etch}} = 0.5P_c$ in figure **4.5**. This occurs due to t_{etch} decreasing with density faster than v_{etch} increases, given in equation **4.2.4**. This could occur for any choice of m, given the right pulse shape, and would be a very bizarre result to observed in an experiment. Experimental testing of a suitable pulse shape would be a useful test of the validity of this model.

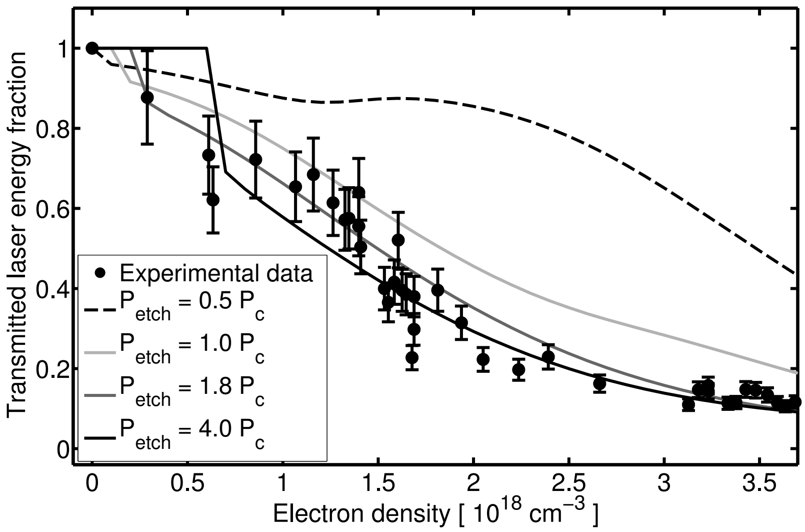

Figure 4.5: Experimental pulse depletion measurements with calculated values for the experimentally measured pulse shape and a pulse front etching threshold of $P_{\text{etch}} = mP_c$.

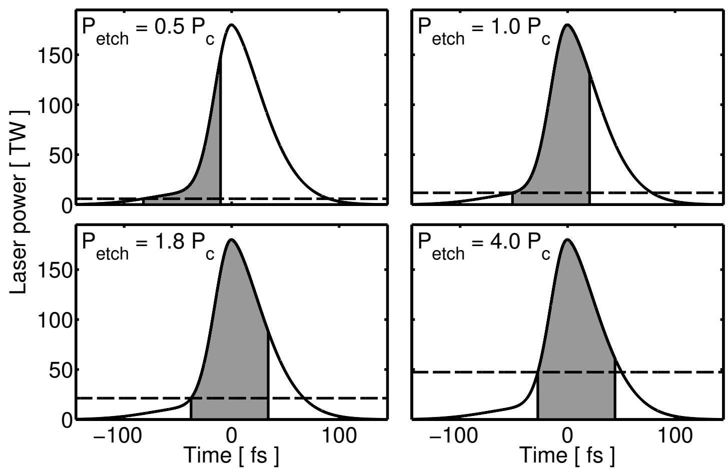

Figure 4.6: Illustration of the pulse front etching model. Here, the measured temporal pulse power profile is plotted and the etched region is coloured grey for $n_e = 2.5 \times 10^{18}$ cm^{-3} and $P_{\text{etch}} = mP_c$.

The most obvious effect that is not included in this model is pulse compression, which is observed to occur over $n_e = 0 - 1.5 \times 10^{18}$ cm^{-3} (section 4.3). Including this effect would result in a higher rate of depletion, as more of the energy of the pulse would lie within the etched region. This may be able to provide a better fit to the observed behaviour for the $P_{\text{etch}} = 1.0P_c$.

The non-linear dephasing length [Lu07] (see section 2.7.6), given by

$$L_d = \frac{4c\sqrt{a_0}}{3}\frac{{\omega_0}^2}{{\omega_p}^3}, \tag{4.2.5}$$

indicates the maximum acceleration in 15 mm of plasma will occur for $n_e = 1.3 \times 10^{18}$ cm^{-3}. As electron acceleration was seen to be optimal for higher densities, this indicates that injection of electrons into the accelerating structure occurred after some propagation through the plasma. High-energy, quasi-monoenergetic beams were observed for $n_e = 2.2 \times 10^{18}$ cm^{-3}, for which the dephasing length is 6.6 mm. This indicates that significant injection of charge occurs near the halfway point of the interaction length, after the plasma effects have had time to modify the driving pulse. For higher densities, dephasing starts to reduce the energy and quality of the electron beams and the laser pulse is so depleted that it no longer drives a significant plasma wave. The electron beam can then begin to generate a plasma wakefield, further reducing the electron energies.

4.3 Transmitted pulse shape measurements

The FWHM pulse duration of the retrieved pulses from the FROG diagnostic are plotted in figure **4.10**. As the density was increased, the measured pulse duration decreased from an initial 53 fs to below 15 fs. For most of the shots it was not possible to determine the direction of time in the retrieved pulse field and the back propagation, which accounts for the glass in the beam, results in two possible answers for the temporal duration of the pulses.

Pulse length shortening can occur due to pulse front etching [Decker96] or self-phase modulation [Gordon03] and in general both of these occur. In the case of the latter, photon acceleration [Murphy06] results in spectral broadening and then the pulse is compressed by the group velocity dispersion in the wake. This can result in an increase in the peak power of the pulse, whereas pulse-front etching only depletes energy from the pulse.

The transmitted pulse shape was measured with a SHG-FROG (Grenouille) with a 10 μm thick BBO crystal. This diagnostic has spectral bandwidth and temporal resolution to measure pulses as short as 10 fs. The optical path between the exit of the gas jet and the FROG diagnostic contained 2 mm of glass. In order to determine the direction of time firstly the chirp of the input pulse was determined and then gradual changes to this were observed as the plasma density was increased. The initial chirp was diagnosed by adding a known group delay dispersion (GDD) to the pulse with a Dazzler (a commercial Acousto-Optic Programmable Dispersive Filter (AOPDF)) and observing the effect on the measured GDD. The additional GDD was varied in the range of -1500 to 1000 fs^2 while the absolute chirp was measured. This then shows whether the original pulse had a positive or negative chirp. The results of these measurements are shown in figure **4.7**, along with a linear fit with a gradient of 1. These results show that the initial laser pulse was negatively chirped with a GDD of 726($\pm$239) fs^2.

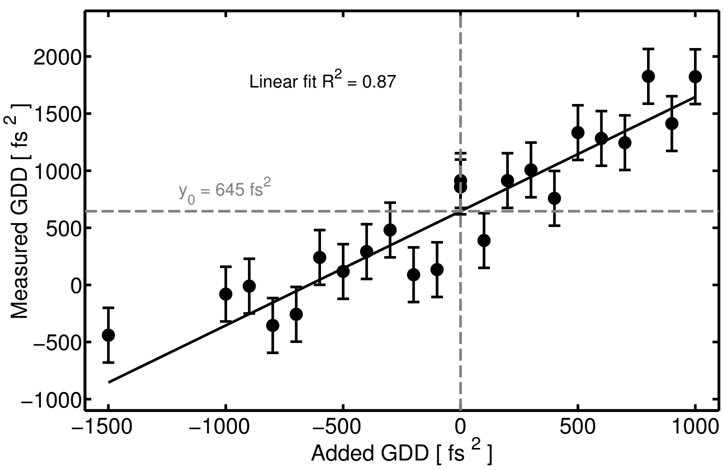

Figure 4.7: Measured GDD from the FROG diagnostic as a function of additional GDD added with a DAZZLER. The linear fit gives an initial pulse GDD of 645($\pm$239) fs^2. This indicates that the pulse is negatively chirped before the plasma interaction. The glass in the optical path accounts for another 80 fs^2 so the initial pulse in the vacuum chamber has a GDD of 726($\pm$239) fs^2. The error bars are calculated from the RMS error to the linear fit.

A common, and useful way of visualising a laser pulse is the Wigner transform [Wigner32], which provides a photon distribution map in time-frequency space and is defined as,

$$W(t,\omega) = \int_{-\infty}^{\infty} E(t'-t/2)E(t'+t/2)\exp(i\omega t)\mathrm{d}t \tag{4.3.1}$$

It was originally formulated to express the phase space of an ensemble of particles in quantum mechanics. Although there are some classically unrealistic properties of a Wigner distribution (i.e. there can be regions with negative values) it serves to provide an intuitive picture of the spectral and temporal properties of laser pulses. The marginals of the distribution, $S(\omega) = \int W(t,\omega)\,dt$ and $I(t) = \int W(t,\omega)\,d\omega$, are equal to the spectral and temporal intensity profiles respectively. Figure **4.8** shows the Wigner distributions and temporal profiles of the measured pulse after transmission through a 15 mm plasma. A gradual change in the pulse profile is seen as the plasma electron density is increased from 0.0–0.8 $\times$ 10^{18} cm^{-3}. Spectral broadening is observed as the density is increased, along with a reduced chirp, leading to pulse compression down to 20 fs for $n_e = 0.83 \times 10^{18}$ cm^{-3}. Independent confirmation for the direction of time in the retrieved pulses was obtained

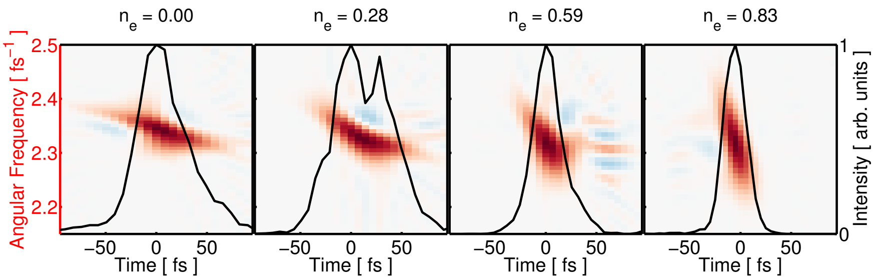

Figure 4.8: Wigner distribution (left axis) and temporal pulse profile (right axis) of the laser pulse after transmission through a 15 mm helium gas jet with the electron density given in units of 10^{18} cm^{-3}. The incident pulse (left) had a slight residual negative chirp. For each increase in plasma density the bandwidth of the laser spectrum broadened and the pulse was compressed temporally.

by using the measurements from an additional FROG. The beam path to this secondary diagnostic contained an additional 5.7 mm and 1 mm of fused silica and BK7 respectively. Comparison of the retrieved pulses from each FROG allows the direction of time to be uniquely determined as the relative chirp difference between the two pulses is known.

Figure **4.9** shows the Wigner distributions of the retrieved pulses from both FROGs for $n_e = 0.3 \times 10^{18}$ cm^{-3} . Both potential time directions are shown after adjusting the spectral phase of the pulses to account for the glass in the optical paths. Therefore, two of the Wigner distributions shown (one for each FROG) should represent the pulse shape after exiting the plasma. The two matching Wigner distributions are those of the negatively chirped pulses, confirming the previous analysis. As the second FROG used a thicker crystal and had a narrower spectral range it was only usable for shots with $n_e < 0.6 \times 10^{18}$ cm^{-3}, for which the spectral broadening and pulse compression was within the range of the diagnostic. When the spectrum was clipped by the diagnostic it was not possible to obtain a retrieval of the pulse profile.

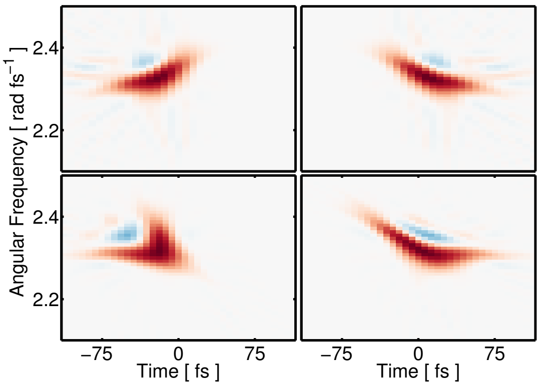

Figure 4.9: Wigner distributions of the retrieved pulses (both possible time directions) from FROG A (top) and FROG B (bottom) for $n_e = 0.3 \times 10^{18}$ cm^{-3}. All pulses have been back-propagated through the glass in the optical paths, so the correct time direction choices are the two pulse that match (right).

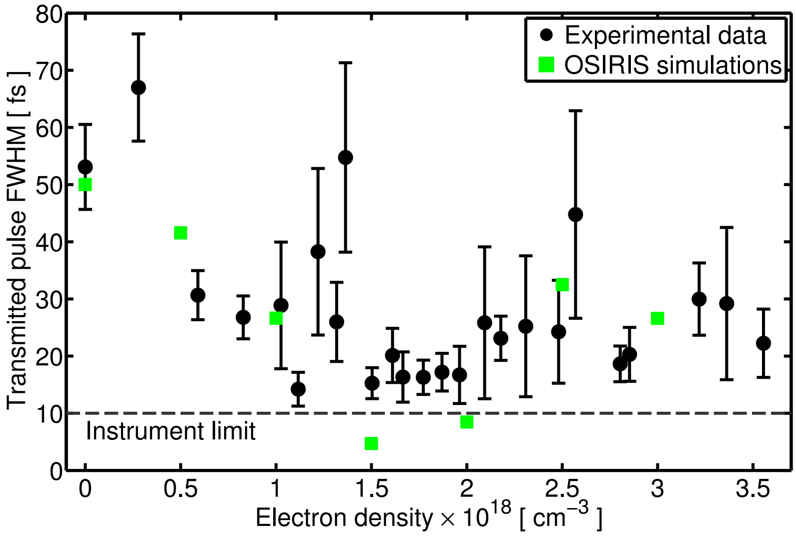

Figure 4.10: Transmitted pulse duration (FWHM) as a function of target electron density. Each point in the experimental data is averaged over shots within a density bin width of 0.1×10^{18} cm^{-3}. Uncertainty in the direction of time gives two possible results for $n_e > 1 \times 10^{18}$ cm^{-3}. The error bars are the combination of this uncertainty, the measurement errors and the standard error for each point.

For $n_e > 1 \times 10^{18}$ cm^{-3}, it was not possible to determine the direction of time for the retrieved pulses. Figure **4.10** shows the pulse temporal width (FWHM) as a function of density, after averaging over these two possibilities and over a density bin width of 0.1×10^{18} cm^{-3}. A large amount of scatter is observed in the data, however pulse lengths below 20 fs are routinely observed for n_e = 1–2 $\times$ 10^{18} cm^{-3}. The shortest observed pulse length on a single shot was 13.8($\pm$2) fs for $n_e = 2.1 \times 10^{18}$ cm^{-3}. A large variation in transmitted pulse length is observed for high densities due to depletion of the main pulse. This reduces the intensity of the main peak resulting in the observation of multiple highly structured pulses, which are highly variable. The largest shot-to-shot variations were seen for $n_e = 1.3$ and 2.5×10^{18} cm^{-3}, where as density regions between these values were relatively stable.

4.3.1 Transmitted pulse power and intensity

By combining the transmitted energy, spatial profile and pulse length measurements it is possible to obtain the peak power and intensity of the guided pulse. The pulse power is readily obtained from setting the energy of the transmitted pulse equal to the time integral of the temporal pulse shape,

$$\mathcal{E} = \int_{-\infty}^{\infty} \mathcal{P}(t)\, dt \; . \tag{4.3.2}$$

This gives a spatially averaged pulse power, as energy from outside of the guided filament will also propagate to the detector. For $n_e \simeq 1.5 \times 10^{18}$ cm^{-3}, the energy of guided filament is approximately equal to the unguided fraction and so the FROG measurements will be a superposition of both. The pulse power after transmission through 15 mm of plasma is plotted in figure **4.11**. The greatest power enhancement at the exit of the plasma is observed for $n_e = 1.1 \times 10^{18}$ cm^{-3}, where the power is increased from 0.18 PW to 0.32 PW. At this density the pulse length is shortened to 14 fs while the energy transmission is still around 70%, corresponding to the highest power few cycle pulse ever achieved. For higher densities no additional pulse compression is observed and the laser is more strongly depleted. This is indicative of a greater coupling of laser energy into the plasma wave and acceleration of electron beams. As the experiment relied on self-injection to obtain electron beams, it is likely that pulse compression was necessary to achieve injection at moderate ($\sim 1.5 \times 10^{18}$ cm^{-3}) densities. As this is the region in which the highest quality and energy of electron beams is observed pulse compression appears to be crucial for self-injection laser wakefield acceleration.

It is also possible to estimate the peak intensity of the laser pulse at the exit of the plasma

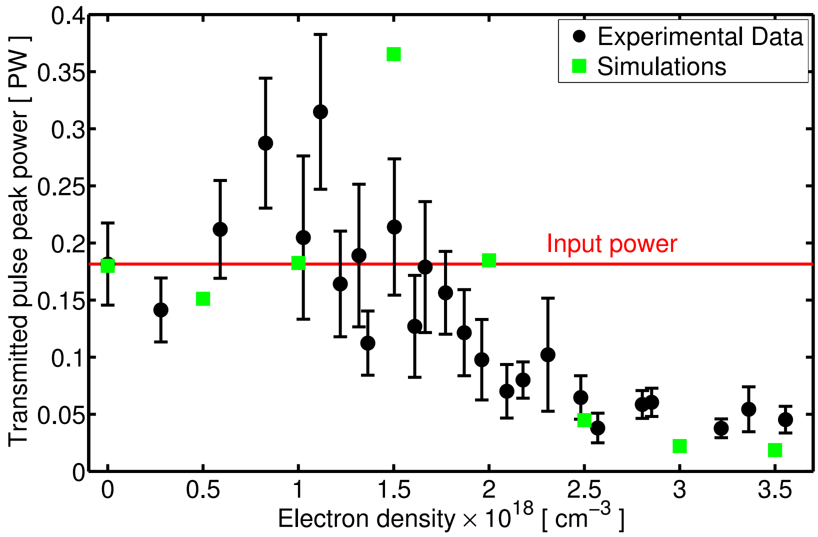

Figure 4.11: The peak pulse power plotted of the transmitted laser against gas electron density. The peak input power is 0.18 PW and a significant power increase is observed for $n_e = 0.6 - 1.1 \times 10^{18}$ cm^{-3}. The error bars are the combination of errors in the energy and pulse shape measurements.

by equating the pulse power to the space integral of the intensity,

$$\mathcal{P}(t) = \int_{-\infty}^{\infty} \int_{-\infty}^{\infty} I(t, x, y)\, dx\, dy \; . \tag{4.3.3}$$

As the spatial variation of the pulse shape is not known, it was approximated by assuming that the pulse shape is the same over all space. Comparison to 2D simulations to obtain this parameter is not straightforward as the beam is only free to expand in one direction. Therefore, as the beam diameter increases, the fluence will drop linearly with beam radius instead of R^2 as it would in the 3D case. Therefore, the final beam intensity will not be truly representative if there is significant change in the transverse pulse profile. For comparison with the experimental data, the final transverse pulse profile from the simulations was integrated assuming cylindrical symmetry to find the peak intensity. The experimental and simulation peak intensities, inferred in this way, are plotted in figure **4.12**.

The peak intensity of the incident laser pulse was determined to be 2×10^{19} Wcm^{-2} from measurements of the pulse energy, focal spot distribution and temporal profile. The greatest intensity observed at the exit mode was 2×10^{18} Wcm^{-2} for $n_e = 1.5 \times 10^{18}$ cm^{-3}. This is an order of magnitude decrease compared to the peak vacuum intensity, and indicates that a much lower intensity plasma wave may be driven at the exit of plasma

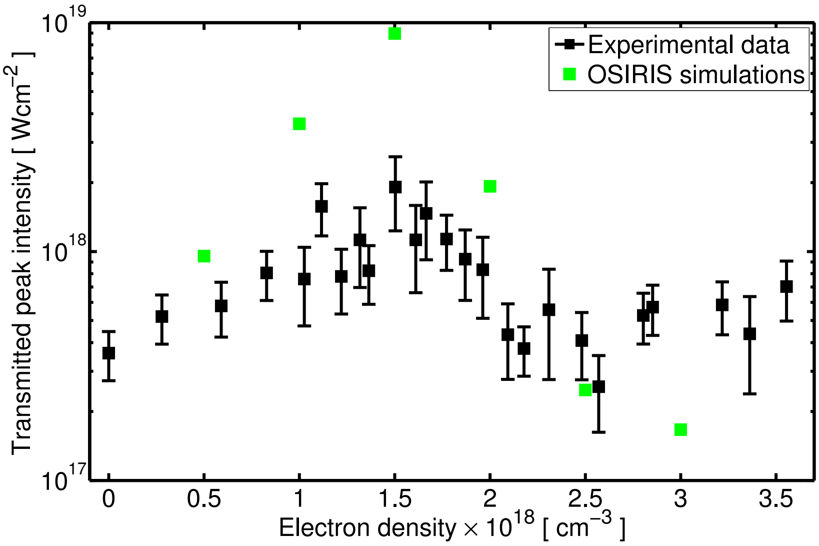

Figure 4.12: The transmitted pulse peak intensity as inferred from the spatial and temporal profile of the pulse at the exit of the plasma. Note that the peak vacuum intensity of the laser pulse at the entrance to the plasma is 2×10^{19} Wcm^{-2}. The error bars are the combination of errors in the energy, pulse shape and exit mode focal spot measurements.

as compared to earlier in the interaction. However, it is likely that the method used here underestimates the intensity as the peak power in the guided region of the pulse may be greater than the average value. A more direct measurement of the pulse intensity, combined with 3D simulations is required to determine if a high pulse intensity can be maintained over 15 mm of self-guided propagation. In addition, the density ramp at the exit of the gas jet may result in a spot size increase, and hence a reduction in intensity that is not representative of the guided pulse in the density plateau.

4.4 Simulation of the laser pulse propagation

Simulations were performed using the OSIRIS [Fonseca02] particle-in-cell code to model the evolution of the optical and plasma waves. The 2D3V simulations were run in a moving box of 200×200 μm divided into 8000×800 cells in the pulse propagation (x) and the transverse (y) directions respectively. The relatively poor transverse resolution was required in order to satisfy the Courant-Friedrichs-Lewy condition while keeping $\mathrm{d}x/\mathrm{d}t \simeq c$ to minimise the effects of numerical dispersion in the laser propagation direction. Convergence testing (appendix **A.3**) indicates that this grid resolution accurately captures the relevant processes. Also, when measuring the laser pulse evolution, it was seen that 1D simulations produced quantitatively similar results to 2D simulations indicating that the majority of the physics is longitudinal. It is therefore assumed that 2D simulations are capable of reproducing the results that would be obtained from 3D simulations. The pulse was modelled as a gaussian with FWHM duration of 50 fs, focused to a spot width FWHM of 25 μm and a peak a_0 of 3. The plasma target was 15 mm in length including initial and final density ramps over 500 μm. Five runs were performed with electron densities of n_e = 1–4 $\times$ 10^{18} cm^{-3} each with 4 particles per cell and stationary ions. Comparison simulations were performed which showed that no appreciable difference was observed in the laser pulse evolution when including a mobile He^{2+} ion species. The pulse duration of the transmitted pulse was determined by removing the rapidly oscillating component from the electromagnetic pulse after it exits the plasma and measuring the FWHM in the longitudinal direction. The electromagnetic radiation fields were found by subtracting the space charge contribution to the electric fields as shown in section 3.4.2. The transmitted energy was calculated by integrating the Poynting vector over the 2D plane. The results are plotted in figures **4.4** and **4.10** alongside the experimental data.

4.4.1 Simulation results

The results from 2D simulations are shown in figures **4.4** and **4.10** to **4.12**. Quantitative agreement is seen with the transmitted pulse energy indicating that the relevant laser depletion processes have been accurately captured. The rate of pulse compression also fits well with the experimental data. It shows compression to a minimum pulse length of 5 fs at $n_e = 1.5 \times 10^{18}$ cm^{-3}. For higher densities the pulse length increases again once almost all the laser energy is depleted. Self-injection of a small number of electrons is observed at $n_e = 1 \times 10^{18}$ cm^{-3}, with significantly more charge accelerated at $n_e = 1.5 \times 10^{18}$ cm^{-3}. Pump depletion for $n_e > 2.5 \times 10^{18}$ cm^{-3} results in a termination of particle acceleration before the end of the 15 mm plasma, and for $n_e = 4 \times 10^{18}$ cm^{-3} the accelerated electron bunch drives a wakefield itself once the laser pulse is fully depleted.

The general quantitative agreement of the pulse properties between the 2D simulations and the experimental data indicates that the phenomenology observed in the simulations can be used to understand the evolution of the laser pulse in experiments. However, some disagreement is observed when comparing the spectral evolution of the laser. 1D simulations were performed using a numerical fit to the measured temporal pulse profile using the EPOCH [Brady11] PIC code. Figure **4.13** shows the Wigner transforms of the simulated pulse after 15 mm of plasma for increasing electron density from left to right. A much greater red-shift is observed in the simulations, with the central wavelength shifting to 900 nm. This enhanced red-shift is a common feature of PIC simulations and as yet the cause of this discrepancy is not known. Also, the red-shift is greatest at the centre of the pulse, where the intensity is greatest, in contrast to the experimental data which shows the largest red-shift closer to the back of the pulse. However, the 'v' shaped distribution seen in the $n_e = 0.3$ and 0.6×10^{18} cm^{-3} simulations is qualitatively similar to the experimental observations in figure **4.8**. For the 2D simulations, and experimental results, the pulse is not well guided for $n_e < 1 \times 10^{18}$ cm^{-3}, so photon acceleration, which depends on pulse intensity, is likely to be overestimated by 1D simulations. In reality the energy spreads out as the pulse propagates through the plasma, leading to a reduced peak intensity. This will also reduce the amplitude of the plasma wave and potentially lead to a change in the photon acceleration experienced by the laser. In addition, the energy away from the centre of the pulse will not experience any photon acceleration effects and so may contribute to the appearance of an overall reduction in red-shift.

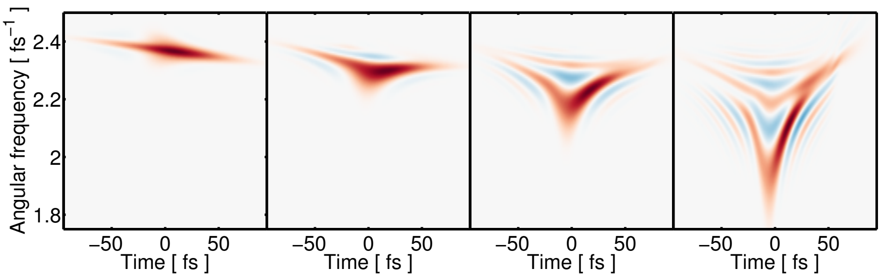

Figure 4.13: Wigner distributions of the laser pulse from 1D PIC simulations after 15 mm of plasma with (left to right) $n_e = 0, 0.3, 0.6$ and 1×10^{18} cm^{-3}.

4.5 Gas nozzle diameter comparisons

Data was also collected with 5 and 10 mm nozzles using the same diagnostic set. As expected, the shorter interaction length results in a higher energy transmission for the same plasma density. Figure **4.14** shows the dependence of the energy transmission with areal electron density (ρ_e), i.e. the electron density multiplied by the nozzle diameter. All three nozzles display a remarkably similar trend indicating that the rate of pulse depletion has the same dependence on plasma density as with propagation distance.

In the 2D OSIRIS simulations the laser energy was well guided to a spot width approximately equal to twice the 'blowout' radius given by equation **4.2.3**. The change in spot

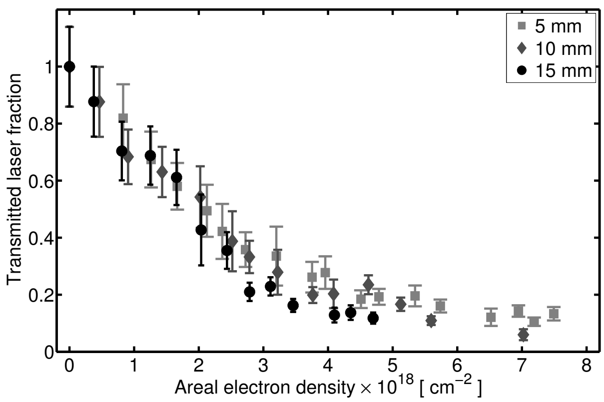

Figure 4.14: Transmitted laser energy fraction as a function of areal density for nozzle diameters of 5, 10 and 15 mm. Results are averaged over a 0.4×10^{18} cm^{-2} bin width and the error bars are a combination of the experimental and standard errors.

width from the input pulse to the matched spot occurs within a few millimeters, with the fastest evolution observed for the highest density. Once the spot size has stabilised the subsequent evolution of the laser pulse is dominated by the longitudinal effects and the depletion of the pulse energy. The rate at which energy is lost, and the rate of pulse compression is seen to scale with the $n_e L$, where L is the propagation distance. Figure **4.15** illustrates this by showing the laser pulse energy and pulse length as a function of $Lc_0 n_e/n_c$. A close match is seen for all the simulation results, indicating that the evolution rate chosen is a good approximation. This linear dependence on plasma density has also been analytically derived for the pulse front etching model [Decker96] pump depletion length [Shadwick09, Teychenne94] and pulse compression rate [Schreiber10]. This linear relationship indicates that the evolution within a particular plasma target as a function of propagation distance can be investigated by performing a scan of plasma density.

4.6 Effects of pulse evolution

Figure **4.16** shows the evolution of the laser pulse and the generated wakefield from an OSIRIS simulation with $n_e = 4 \times 10^{18}$ cm^{-3}. Self-focusing is observed in the first 1 mm of plasma, after which a stable guided spot size is reached. The plasma wave is generated by the leading edge of the laser pulse which moves slower than the linear group velocity as the leading edge is lost due to diffraction and energy coupling to the wake. The majority of the leading half of the pulse is lost after ~ 5 mm of propagation so that the peak of the laser pulse is now directly driving the wakefield structure. This increases

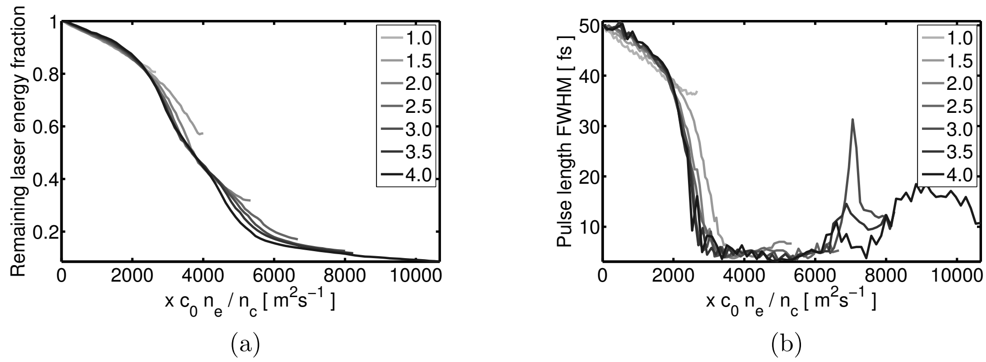

Figure 4.15: (a) Depletion of laser energy and (b) pulse compression in 2D OSIRIS simulations. The legend values are electron density $\times 10^{18}$ cm^{-3}.

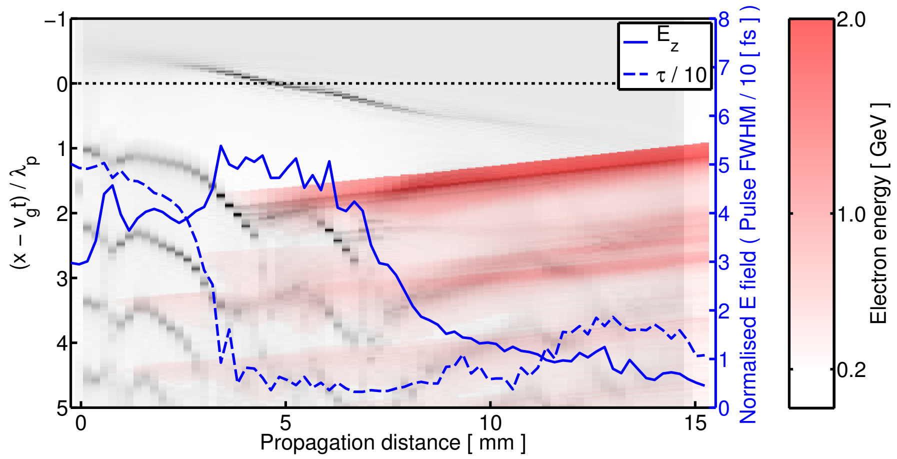

Figure 4.16: A map of the on-axis electron density (greyscale) in the frame co-moving with the driving laser pulse as a function of propagation distance from an OSIRIS simulation with $n_e = 4 \times 10^{18}$ cm^{-3}. The red colouring shows the peak energy of accelerated electrons above 100 MeV. The left y-axis shows position relative to the initial peak intensity point travelling at v_g. The right y-axis gives the values for the blue curves, which show the peak electric field of the laser pulse normalised by $(m_e\omega_0 c/e)$ (solid line) and the FWHM pulse duration divided by 10 (long dashed line).

the amplitude of the electron density modulation generated and subsequently the length of the first wakefield period increases. Pulse compression is also observed, leading to an enhancement of the peak electric field and further increasing the wakefield amplitude. The position of the second maxima of the electron density recedes from the laser pulse at approximately ≈ 5 nm fs^{-1}, effectively decreasing the phase velocity of the plasma wave as seen by Fang *et al.* [Fang09] . The relativistic γ factor for an electron co-moving with the plasma wave phase velocity is reduced from 12 to 5.5 at this point, which occurs between 3 and 4 mm into the plasma. This reduces the a_0 threshold for self-injection from 4.7 to 2.9 according to the formula in Thomas [Thomas10], matching observations of trapping and acceleration at this point. Self-injection into a dynamically expanding bubble is also described in PIC simulations by Kalmykov *et al.* [Kalmykov09] for the case of an increase in the guided spot size due to a density perturbation. Efficient acceleration of this bunch is seen until 8 mm into the plasma, after which point the driving laser pulse is mostly depleted and no longer drives a strong wakefield. However, by this point electrons in the bunch have already achieved a maximum kinetic energy of 2 GeV. As the laser loses influence, the bunch itself begins to drive a strong plasma wave which accelerates trailing electrons up to ≈ 700 MeV.

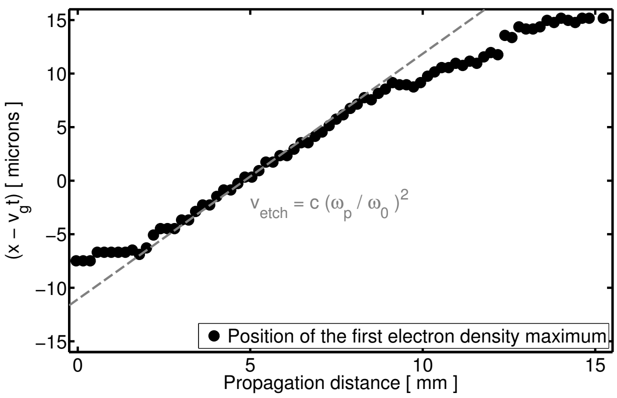

Figure 4.17: The blue circles show the motion of the front of the wakefield relative to the point given by $x = v_g t$. The red line gives the expected motion of this point from the pulse front etching model [Decker96].

Although the linear group velocity of the laser pulse is given by $v_g = c\sqrt{1 - n_e/n_c}$, the position of the first maximum of the electron density, i.e. the point at which the wakefield is being driven by the laser, is seen to move more slowly. Figure **4.17** shows this position as a function of propagation distance and fits well the pulse front etching rate given by Decker et. al [Decker96]. This will also have the effect of reducing the required trapping condition as an electron co-moving with the wakefield will have $\gamma = (1 - (v_g - v_{etch})^2/c^2)^{-1/2}$.

4.6.1 Wakefield acceleration length model

From the PIC simulations it appears that self-injection occurs when the length of the first period of the wakefield rapidly increases. This occurs during a phase of rapid pulse compression that was seen in the simulations and in the experimental measurements. As the pulse evolution rate has been demonstrated to be closely proportional to n_e, this allows the injection point, and the point at which the pulse energy is almost completely depleted, to be estimated as a function of density. The experimental measurements for the 15 mm nozzle shows that the pulse is fully compressed for $n_e = 1.5 \times 10^{18}$ cm^{-3} and fully depleted by $n_e = 2.5 \times 10^{18}$ cm^{-3}. The pre-injection, and pulse depletion lengths are then given by,

$$L_{\mathrm{PI}} = 13 \left(\frac{n_e[\mathrm{cm}^{-3}]}{1.5 \times 10^{18}} \right) \ [\ \mathrm{mm}\ ]\ , \tag{4.6.1}$$

$$L_{\mathrm{PD}} = 13 \left(\frac{n_e[\mathrm{cm}^{-3}]}{2.5 \times 10^{18}} \right) \ [\ \mathrm{mm}\ ]\ , \tag{4.6.2}$$

with the plasma length for the 15 mm nozzle taken as 13 mm to take account of the density ramps at the edge of the gas jet (11 mm plateau region plus 4 mm ramp region at an average of half plateau density). The acceleration length is $L_{\mathrm{PD}} - L_{\mathrm{PI}}$ up to the limit of the plasma length. In the blowout regime the accelerating field linearly increases with distance from the centre of the ion cavity up to the maximum $E_{\max} = \sqrt{a_0} m_e c_0 \omega_p$ at $R_b = 2\sqrt{a_0}/k_p$ [Lu06, Lu07]. The dephasing length is given by $L_{\mathrm{deph}} = R_b/(1 - \beta_\phi)$, where β_ϕ is the phase velocity of the plasma wave divided by the speed of light. The maximum electron energy is then $\epsilon_e = eE_{\max} L_{\mathrm{deph}}/2$. The rate of energy gain for the electron will decrease quadratically with acceleration length up to the dephasing length and then become negative as the electron moves into the decelerating phase of the bubble. Therefore the final energy of an electron accelerated over L_{acc} is given by,

$$\epsilon_e = \frac{2 a_0 m_e {c_0}^2}{1 - \beta_\phi} \left(R - \frac{R^2}{2} \right)\ , \tag{4.6.3}$$

where $R = L_{\mathrm{acc}}(1 - \beta_\phi)/R_b$. Due to pulse front etching the phase velocity of the wave is not exactly the group velocity of the pulse but can be estimated as [Decker96],

$$\frac{1}{1 - \beta_\phi} \simeq \frac{2}{3} \frac{{\omega_0}^2}{{\omega_p}^2}\ . \tag{4.6.4}$$

Equation **4.6.3** with L_{acc} calculated from the observed pulse compression and depletion points are used to calculate the expected maximum electron energies, using the estimate $a_0 = 5$ to include pulse compression effects as seen in the PIC simulations. The nozzle lengths are taken as the plateau distance for each nozzle plus half of the density ramp length.

The calculated values are plotted alongside the experimental measurements in figure **4.18**. A good fit is seen to the observed electron energies in terms of the peak energies and the

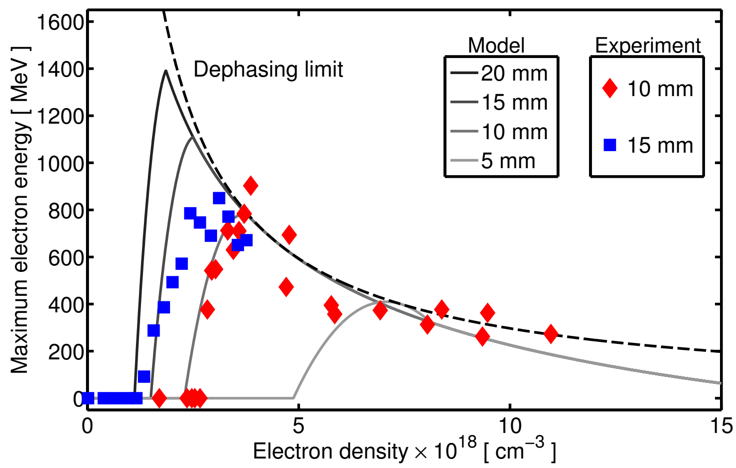

Figure 4.18: The predicted electron energies (solid lines) calculated from the pulse compression and depletion rates observed in the 15 mm gas nozzle. Also plotted is the maximum energy an electron can achieve from acceleration over one dephasing length (dashed line). The experimentally observed electron energies are plotted for the 15 and 10 mm gas nozzles.

variation with plasma density for the 10 mm nozzle. For high densities the predicted acceleration length is longer than the dephasing length, indicating that the maximum electron energies should decrease as the electrons move into the decelerating phase of the wakefield. However, the observed electron energies follow closely what would be expected for acceleration up to the dephasing limit even when the maximum acceleration length is longer. This indicates that injection can occur after L_{PI} and is continuous such that there are always some electrons with the maximum possible energy. This is consistent with experimental observations of the electron spectra at these densities, which are seen to have large energy spreads. For the 15 mm nozzle the electron energies are lower than expected and show a shallower increase in energy with density. This potentially indicates that the laser was not as well guided over the 15 mm nozzle and the longest possible acceleration lengths were not reached or that the laser intensity in the acceleration region was lower than for the 10 mm nozzle.

4.6.2 Effects of a few-cycle driving pulse

The simulations show that the pulse is red-shifted near the peak of the laser pulse, at the first peak in the electron density, and is blue-shifted at the rear of the pulse. The group velocity dispersion then leads to temporal compression of the pulse, increasing the peak intensity of the pulse. The minimum pulse length observed in the simulation for

$n_e = 2.5 \times 10^{18}$ cm^{-3} is 5 fs (FWHM) with the peak $a_0 = 6$ after 8 mm of propagation. At this point the laser spectrum contains a large red-shifted component at the peak of the pulse. As the group velocity of this component is slower than the average, it begins to slip back relative to the peak.

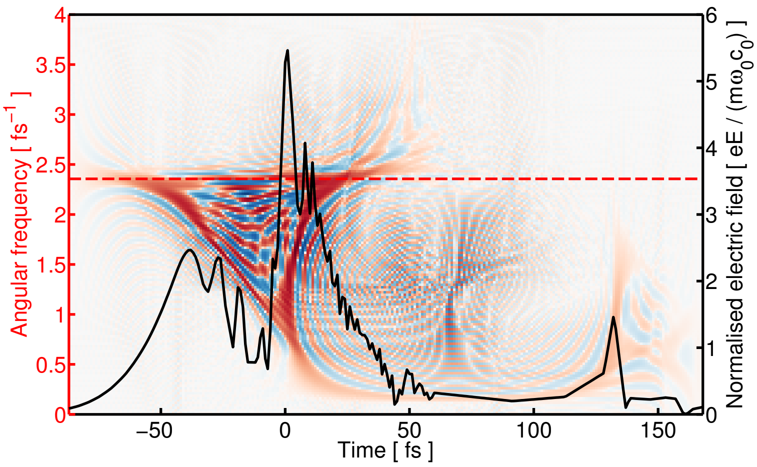

Figure 4.19: The Wigner distribution of the driving laser pulse after 12 mm of propagation through a plasma with $n_e = 2.5 \times 10^{18}$ cm^{-3}.

This is observable in figure **4.19**, which shows the Wigner distribution (specifically the cube root of the Wigner distribution to show regions of lower intensity) of the pulse after 12 mm of propagation. At this point a highly red-shifted fraction of the laser pulse fills the first period of the plasma wave. As the radiation slips back to the second electron density peak, it experiences blue-shifting due to the decreasing refractive index. This effectively traps ≈ 13 μm radiation within the bubble and a second pulse is formed at the rear bubble edge.

The long wavelength radiation in the ion cavity is sufficiently strong to significantly affect the trajectories of the electrons as they are passed by the main laser. The electrons which define the boundary of the ion cavity undergo an oscillation in this long wavelength field leading to a wiggling bubble structure. Figure **4.20** shows some test electron trajectories in the frame co-moving with the laser pulse on top of (a) the electron density distribution and (b) the transverse electric fields. The wiggle in the bubble structure persists until the rear of the bubble, where the blue-shifting of the radiation increases the spatial frequency of the oscillations. This is seen in electron trajectories and also the transverse fields. The transverse fields include the normal focusing space-charge field of the bubble. The trapped radiation significantly modifies this structure and therefore has significant implications for the acceleration of electrons and the generation of betatron radiation.

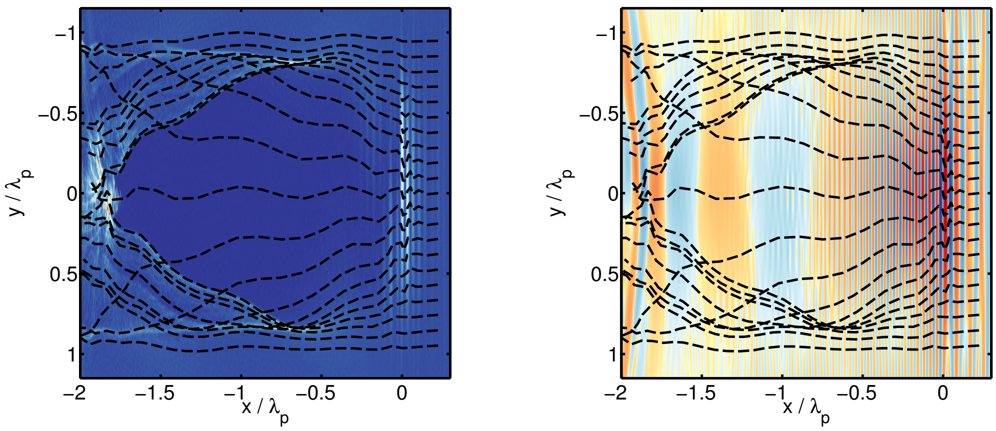

Figure 4.20: (a) A picture of the electron density and laser field intensity after propagating 11 mm through a plasma with $n_e = 2.5 \times 10^{18}$ cm^{-3}. The electron density is shown in blue and the laser field in red. (b) The cube root of the electric field intensity in the y direction from blue to red. The sample electron trajectories are shown as dashed black lines in both images.

The phase velocity of the long wavelength radiation in the bubble is $\approx 1.03c$, and so the phase of this radiation, relative to the front of the ion cavity, changes by 2π over $\approx 1.7ps$. The wiggle in the bubble structure oscillates at the same rate as this relative phase change.

The experimental FROG measurements show a similar effect to that observed in the simulations with the 'C' shape to the Wigner distribution and the formation of a second pulse. Figure **4.21** shows some examples for the range $n_e = 1.5 - 2.5 \times 10^{18}$ cm^{-3} where the effect is observed. The direction of time was chosen such that the direction of curvature of the Wigner distribution matched that observed in the simulations. The pulse spectrum is significantly increased by photon acceleration in the wake and the longer wavelengths are seen to slip back relative to the peaks of the pulses. Some laser energy is also seen as post-pulses extending beyond the linear plasma wavelength. This potentially indicates a increase in the wake length due to pulse compression causing an increase in a_0.

4.7 Initial pulse shape effect

The effect of a non-gaussian driving pulse shape was investigated by comparing two 2D EPOCH simulations, one with a numerical approximation to the measured Gemini pulse and one with an idealised gaussian pulse. The pulse shapes at the start of the simulations

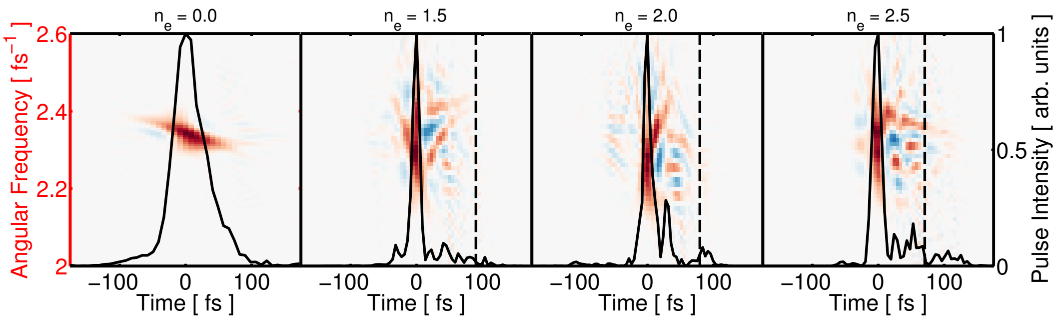

Figure 4.21: Wigner transforms and temporal pulse profiles of the transmitted laser pulse after propagation through 15 mm of plasma. The electron density is given above each image in units of 10^{18} cm^{-3}. The left and right y-axes refer to the Wigner distributions and pulse intensity profiles respectively. The dashed vertical line is positioned one linear plasma wavelength behind the peak of the pulse.

and after 15 mm of propagation are shown in figure **4.22**. For these simulations the Gemini-like pulse was normalised to the gaussian pulse such that the peak power was the same. Another simulation was also performed in which the total energy in each pulse (the integral of the temporal profile) was the same, and very similar results were observed.

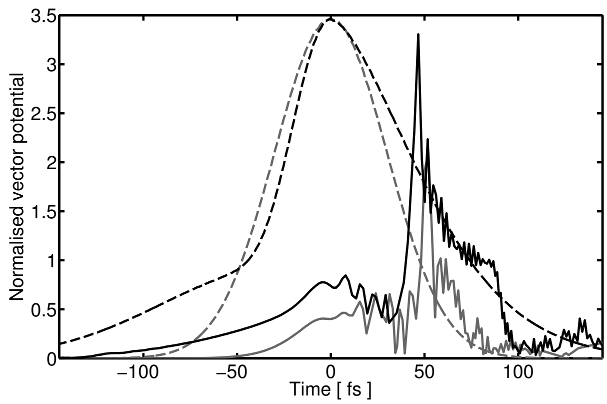

Figure 4.22: Pulse shapes used in 2D EPOCH simulations. The real Gemini pulse shape is shown as the black dashed line and the black solid line is that pulse after propagating through 15 mm of plasma. The gaussian approximation to the real pulse is shown in grey.

The real Gemini pulse has a slight asymmetry, with a slightly sharper rising edge sitting on top of a gradual ramp up in intensity. The main effect this had in the simulations was to slow down the longitudinal evolution of the pulse. Specifically, the point of rapid pulse compression occurred about 1.5 mm later for the non-gaussian pulse. This causes self-injection to occurs slightly later in the non-gaussian case. This may have some effect on the experimental results in that the density threshold for self-injection may be slightly higher than would otherwise be the case.

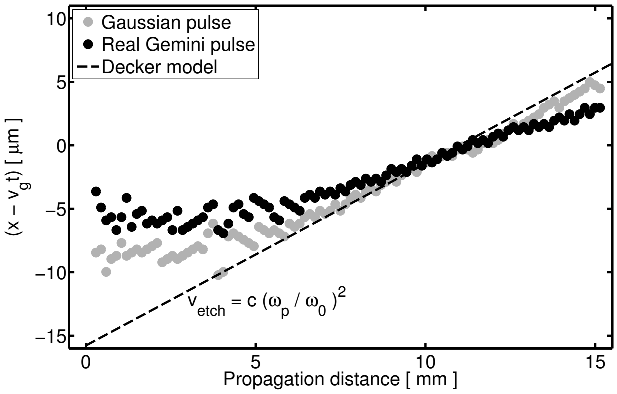

Figure 4.23: Comparison of the etching rates for real and gaussian pulses in 2D simulations. The dashed line shows the analytically derived etching rate given in Decker et. al [Decker96].

Figure **4.23** shows the position of the first maximum of the plasma wave from the simulations with the gaussian pulse and the real Gemini pulse. Although the gaussian pulse simulation follows the expected etching rate, the non-gaussian Gemini pulse is seen to etch at a slower rate. This slows down the evolution of the laser pulse and also leads to a larger phase velocity for the plasma wave. As a consequence, self-injection is seen later and for a shorter period for the Gemini-like pulse.

4.8 Conclusions

Self-guiding of a relativistically intense laser beam through 15 mm of plasma has been observed leading to temporal compression from an initial 55 fs pulse down to 14($\pm$2) fs. This is accompanied by an increase in the laser power to 320 TW, from an initial value of 180 TW ($\approx$ 78% increase). These pulses are far more powerful than few-cycle laser pulses currently available from conventional laser systems, which have achieved 16 TW in 8 fs [Herrmann09].

The observed dependence of laser depletion with plasma density is well approximated by pulse front etching, when the etching begins at the point which the pulse power is $1/e$ of the peak power. A more physical picture, where the etching threshold power is set to the critical power for self-focusing gives a good fit to the data at low densities, while underestimating the depletion at high densities. This is likely due to pulse compression, which increases the rate of depletion and is not included in the simple model. PIC simulations have been shown to match the experimental results very well and therefore provide a useful tool for further study of the non-linear optics within laser-driven wakefield accelerators. These suggest that pulse compression down to as short as 5 fs can occur while retaining 60% of the initial beam energy.

Measuring the pulse compression and depletion rates as a function of density is seen to be closely equivalent to studying the pulse evolution as a function of propagation length. This allows the optimal electron acceleration plasma density to be predicted for any given plasma length. A semi-empirical model is shown to fit the observed peak electron energies by calculating the accelerating fields and acceleration lengths based on the 'blowout' model of the laser wakefield accelerator.

The pulse compression was seen to be critical in terms of the self-injection process itself. Kostyukov et al. [Kostyukov09] and Thomas [Thomas10] both provide electron trapping thresholds based on the blowout radius and the phase velocity in the wake. The work here shows that the phase velocity is not constant throughout the interaction and the rapid compression of the pulse leads to a brief period in which the phase velocity drops significantly. For a correctly chosen plasma density this can lead to highly mono-energetic electron beams as injection only occurs in one very narrow region of the interaction [Kalmykov09].

Further work is required to fully characterise the pulse intensity as a function of propagation within the plasma interaction. Experimental measurements and 2D PIC simulations indicate that the intensity may drop considerably from the peak input pulse intensity. This would have important consequences for the evolution of the accelerating structure for long propagation lengths in self-guided laser wakefield accelerators. Full 3D simulations and more direct experimental measurements would be required to fully investigate this.

Chapter 5

Reflectivity of Relativistic Plasma Surfaces and Second Harmonic Generation

This chapter details the characterisation of the specular reflection of 50 fs laser pulses obliquely incident with p-polarisation onto solid density plasmas in the intensity range $10^{17} - 10^{21}$ Wcm^{-2}. These measurements give the efficiency and spatial beam quality of the second harmonic pulse generated in these interactions. It also quantifies the reflectivity of the fundamental laser wavelength, allowing an upper limit to be placed on the plasma absorption. A simple model based on the relativistic oscillating mirror (ROM) concept reproduces the observed intensity scaling, indicating that this is the dominant process involved for these conditions.

5.1 Experimental setup

The experiment was carried out using the Astra Gemini laser [Hooker06] which delivered up to 12 J in a 50 fs pulse at a central wavelength $\lambda_0 = 800$ nm. Figure **5.1** shows the setup in which an $f/2$ parabolic mirror focused the laser onto 100 nm thick aluminium foils at a 35° angle of incidence with p-polarisation to create a focal spot with a 2.5 μm full width half maximum (FWHM) containing ~35% of the laser energy. The laser contrast, defined as the ratio of the intensity of preceding amplified spontaneous emission (ASE) to the peak intensity, was measured using a scanning autocorrelator as 10^{-6}. Double plasma mirrors [Ziener03] were used to increase this to 10^{-10}. The intensity on target was varied in the range of 10^{17} - 10^{21} Wcm^{-2} by moving the parabolic mirror relative to the target.

This changed the irradiated spot size while keeping the energy on target constant. The targets were optically flat (waviness less than 0.1 μm over 100 μm) [Spindloe07] aluminium foils.

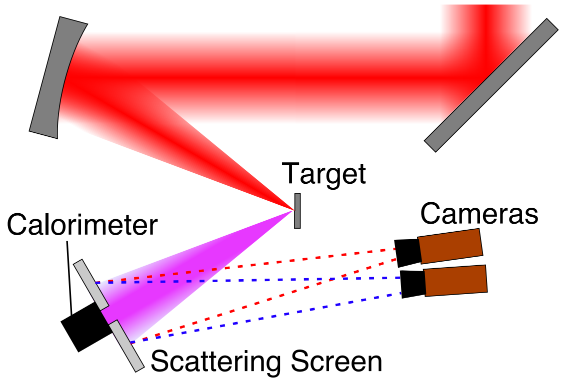

Figure 5.1: Schematic of the experimental setup showing the focusing geometry and the specular reflectivity monitor.

The specularly reflected light from the target was incident onto a plastic (PTFE) scattering screen which was imaged by two cameras each with an interference filter, one centred at 800 nm with 25 nm bandwidth, corresponding to the fundamental frequency ω_0, and one centred at 400 nm with 10 nm bandwidth to observe the second harmonic $2\omega_0$. The screen covered an angular range equivalent to an $f/0.62$ cone and had a 31 mm diameter circular aperture cut into the centre to allow direct energy calibration with a surface absorbing calorimeter. Several low intensity shots were taken, to ensure that almost all the energy incident on the energy meter was at ω_0 with a relatively uniform intensity profile, providing a calibration of the camera signal with the calorimeter. The 400 nm camera was calibrated relative to the 800 nm camera by taking into account the relative responses of the cameras and the opacity of their respective filters at the relevant wavelength. The reflected energy for each wavelength was measured by integrating the signal on the scattering screen, compensating for the holes and edges of the screen. This adjustment was typically $\sim$10% of the measured energy.

5.2 Experimental results

Figure **5.2** shows sample images observed during the intensity scan. No qualitative difference in the 800 nm images was seen until the intensity became $I > 10^{20}$ Wcm^{-2} at which point the signal became noticeably weaker. However, even at the highest intensities the beam profile remains constant in size. This indicates that the plasma surface remained relatively flat over the timescale of the interaction for all the shots. The $2\omega_0$ image was very weak by comparison for $I = 10^{17}$ Wcm^{-2}, but became much brighter as the intensity was increased. The observed 400 nm and 800 nm energy on the screen as a fraction of

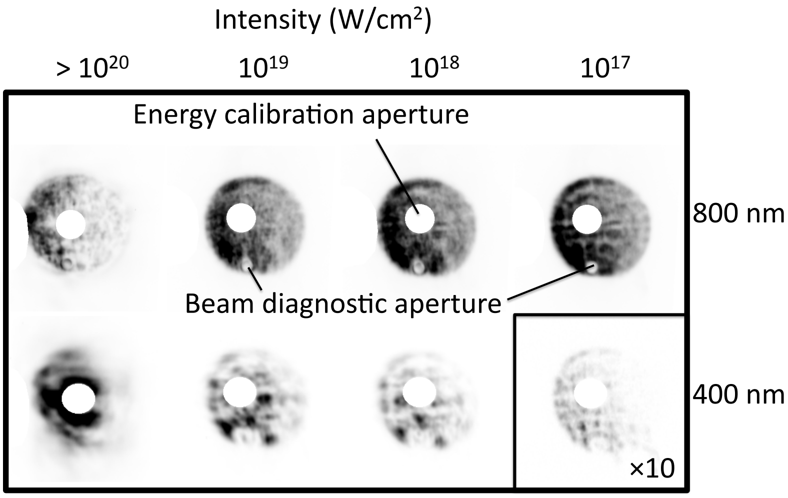

Figure 5.2: Images of the specularly reflected beam. Top line shows the 800 nm (ω_0) and second line 400 nm ($2\omega_0$) images from the same shots. The small hole at the bottom of the beam, visible in the ω_0 image, is caused by a hole in a mirror at the output of the compressor used for pulse length measurement. The central hole was used to calibrate the camera for energy measurements with a calorimeter. Note that the brightness of the $2\omega_0$ image for 10^{17} Wcm^{-2} has been multiplied by a factor of 10 to make it visible on the same scale.

incident laser energy is shown in figure **5.3**. Measurements of the specular 400 nm beam shows the conversion efficiency to $2\omega_0$ increasing with intensity up to a maximum of 22($\pm$8)%. This is consistent with previous work [Hörlein08] which give an efficiency of $> 5\%$ at 10^{19} Wcm^{-2}. The energy converted to $2\omega_0$ represents a significant fraction of the incident laser energy and accounts for most of the reduction in reflected 800 nm energy. For $I > 1 \times 10^{20}$ Wcm^{-2} the reflected ω_0 beam profile shows a loss of brightness while retaining the same beam structure. As higher spatial frequency modulations will be spread over a larger area in the focal plane they will be reflected from regions of lower intensity, which retain high reflectivity. The lower spatial frequencies will be concentrated in the high intensity regions, where they are preferentially converted to higher harmonics.

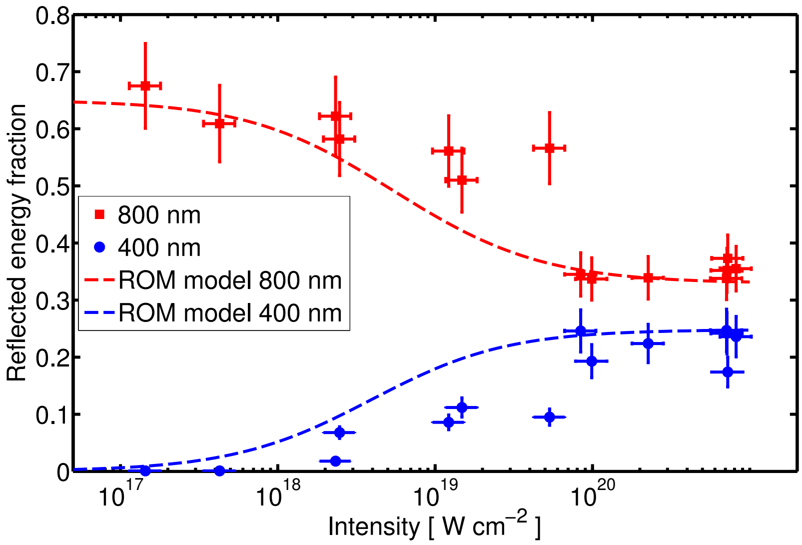

Figure 5.3: Energy incident onto the scattering screen as observed at 800 nm (squares) and 400 nm (diamonds). Vertical error bars are combined calibration and measurement errors. In the region near focus the intensity was calculated as the mean within the FWHM radius, away from focus it is the mean intensity within the beam radius. The dashed lines represent the results of the ROM model.

Therefore, the near field of the reflected beam is observed to contain the high frequency modulations but less overall brightness as observed. This process is analogous to spatial filtering with a high pass filter. For lower intensity interactions, this effect would be reduced as second harmonic conversion efficiency is low for all irradiated regions. Also, because the intensity was decreased by defocusing, the plasma interaction occurs in the quasi-near field of the beam and so no pure spatial filtering can occur.

The profile of the second harmonic beam matches that of the ω_0 beam, except for $I > 10^{19}$ Wcm^{-2} where it becomes more centrally peaked. Here the higher spatial frequencies are much reduced, especially for $I > 10^{20}$ Wcm^{-2}. This is consistent with the spatial filtering observed in the ω_0 beam, confirming that the loss of energy is largely due to second harmonic generation and not due to scattering of the beam outside of the measurement cone. At tight focus, the $2\omega_0$ production efficiency is more efficient in the centre than in the wings, preferentially filtering out high spatial frequencies of the input beam and resulting in a more gaussian profile at $2\omega_0$. Hence, in stark contrast to other methods of SHG, this process has the ability to produce a smoother second harmonic beam than the fundamental beam that drives it.

Several plasma mechanisms exist that can generate harmonics of a driving laser (see section 2.6) such as emission from plasma waves generated by fast electron bunches (coherent wake emission) and reflection of the laser from surface oscillations of the plasma (relativistic oscillating mirror model). Coherent wake emission (CWE) occurs when fast electron bunches, generated by the electric field of the laser, propagate through the target creating plasma oscillations in their wake. In the presence of a density gradient the frequency of these plasma oscillations can range from the laser frequency up the maximum plasma frequency supported by the peak target density. The electron bunches, which are created by the vacuum heating effect, occur at every cycle of the laser field and therefore will preferentially drive plasma waves which are harmonics of the driving laser. These oscillations then emit photons which can be reflected in the specular direction by the higher density regions of the target. This process has been studied experimentally and theoretically and the efficiency is found to be weakly dependent on intensity from $I = 10^{15}$ Wcm^{-2} [Quéré06]. This does not seem to fit our observations which show an increase in efficiency at $I = 10^{18}$ Wcm^{-2}.

The relativistic oscillating mirror (ROM) model describes specularly emitted harmonics to be the result of the reflection of the laser from the plasma surface, which oscillates rapidly under the electromagnetic field of the driving pulse. As the reflection point is moving within the cycle of the laser field, this redistributes the phase of the reflected pulse, corresponding to the generation of new frequencies in the reflected spectrum. The period of the plasma surface oscillation is set by the period of the laser, so the new spectral components will be at harmonics of the driving field. The magnitude of the surface oscillation will be strongly dependent on the intensity of the laser and significant modification of the laser will only occur once the electron motion becomes relativistic ($I > 10^{18}$ Wcm^{-2}). Higher frequency components in the plasma surface motion will be observed as the intensity increases but the amplitude of the ω_0 component of the surface displacement cannot exceed c_0/ω_0 so the SHG component will saturate. Hence, our experimental data appears to follow the expected behaviour given by the ROM model.

5.3 Relativistic oscillating mirror model

In order to calculate the motion of the plasma surface caused by the electromagnetic field of the incident laser the surface is modelled as an infinite sheet of electrons with an immobile ion background, based on methods in [Lichters96, Landau75]. All electrons are assumed to move in identical trajectories, which are given by solving the electron motion in a plane wave for which the time averaged electron position remains constant. Using the derivation shown in section 2.2 (and in more detail in appendix **A.1**) , the Lorentz factor for resulting particle motion is,

$$\gamma = \frac{a^2 + \alpha^2 + 1}{2\alpha}, \tag{5.3.1}$$

and the transverse and longitudinal velocity components are,

$$v_\perp = \frac{2\,a\,\alpha\,c}{a^2 + \alpha^2 + 1}; \qquad v_\parallel = \frac{(a^2 - \alpha^2 + 1)\,c}{a^2 + \alpha^2 + 1}, \tag{5.3.2}$$

where α is a constant of integration. For the ROM model any drift velocity in this rapid oscillation will be eliminated as long as the average position of the solid surface is assumed to remain constant. This is done by numerically calculating the value of α for which the time averaged $v_\parallel$ is zero. Equation **5.3.2** can then be integrated to give the particle position as a function of time. The projection of this particle motion onto the target normal axis gives the surface motion of the oscillating mirror. The reflected pulse is temporally modulated by the motion of the reflecting surface, resulting in new frequency components. Because the period of the plasma surface is set by laser field period this results in harmonics being generated in the reflected pulse. Some target expansion or hole-boring of the target would be expected, which would lead to an additional Doppler shift but this is ignored here for simplicity.

The reflected pulse at a fixed position is given by,

$$E_r = E_0 \sin(\omega_0 t'), \tag{5.3.3}$$

where E_0 is the amplitude of the electric field and,

$$t' = t + \frac{2\,z' \cos\theta}{c}. \tag{5.3.4}$$

t' and z' are the retarded time and position respectively and θ is the angle of incidence. The retarded position is the point of intersection of a light ray and the plasma surface. This position is obtained numerically which allows the reflected field to be calculated as demonstrated in figure **5.4**.

In order to calculate the reflected field for a given intensity the input pulse is defined with a $\sin^2(\pi t/T)$ intensity envelope, where T defines the length of the pulse. The surface motion is then calculated using equations **5.3.1** and **5.3.2** and the reflected pulse is generated from the result. Figure **5.5** illustrates the motion of the plasma surface, and the reflected electric field for intensities ranging from $10^{17} - 10^{20}$ Wcm^{-2}, showing the increasing non-linearity in the reflected pulse.

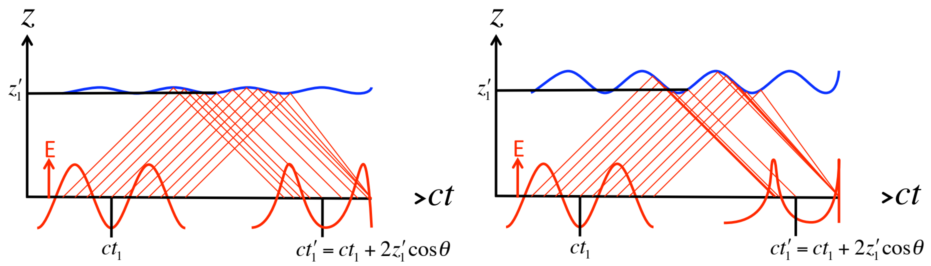

Figure 5.4: Illustration of the effect of an oscillating reflecting surface on the reflected wave. The sinusoidal incident wave travels from $z = 0$ and reflects from the plasma surface at z_1'. The time taken for a light ray to propagate from $z = 0$ to z_1' and back to 0 is $2z_1' \cos\theta$, where θ is the angle of incidence of the electromagnetic wave.

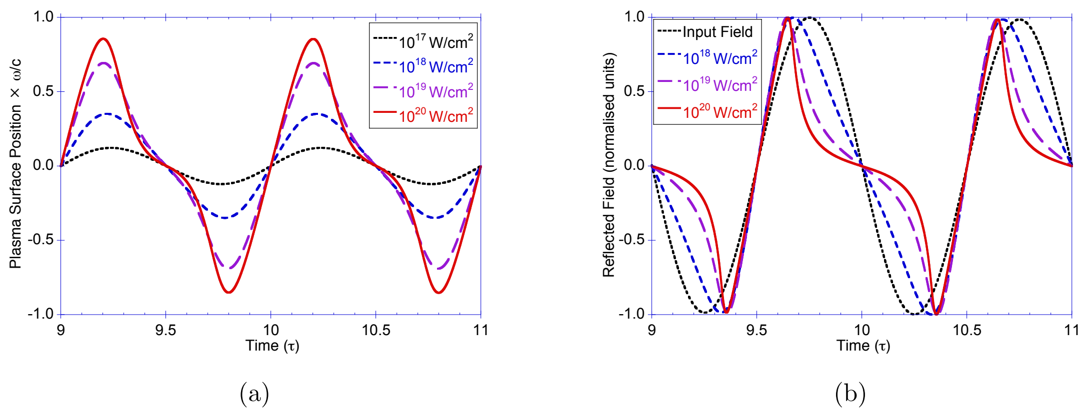

Figure 5.5: Two cycles of (a) the plasma surface position and (b) the reflected electric fields, normalised to the maximum amplitude at each intensity, given by the ROM model (the deviation from the input field is negligible for 10^{17} Wcm^{-2}). τ is the period of the laser.

The Fourier transform of the reflected field gives the spectral content and the strength of the ω_0 and $2\omega_0$ are then found as fractions of the total energy in the spectrum. The results of the ROM model are compared with the experimental results in figure **5.3**. As absorption is not included in the model all values were multiplied by 0.65 to represent the absorption inferred from the experimental measurements (see figure **5.6**). The model closely follows the measured ω_0 and $2\omega_0$ reflectivities and also displays the saturation in SHG efficiency and ω_0 reflectivity at the level determined experimentally. Lower conversion to $2\omega_0$ is seen for $I = 10^{19} - 10^{20}$ Wcm^{-2} compared to the ROM model. This could be due to the complex phase and intensity profiles of the laser in this transition region between the far-field and near-field of the laser. In addition, the model predicts

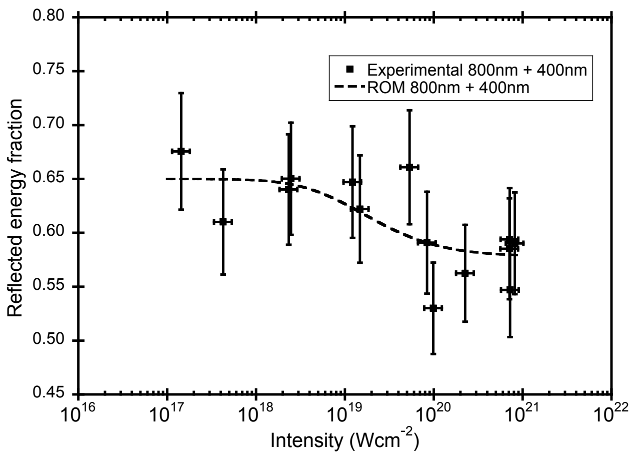

Figure 5.6: Specular reflectivity into ω_0 and $2\omega_0$ given by the ROM model and measured experimentally.

that the sum of ω_0 and $2\omega_0$ should decrease as a fraction of the total specularly reflected energy by up to 7% at the highest intensities (see dashed line in figure **5.6**). This is due to the increasing production of higher harmonics predicted by the model. The measured combined energy in the reflected pulse at 400 and 800 nm shows an average drop of 8% for $I > 10^{20}$ Wcm^{-2}. This indicates that the magnitude of additional energy loss mechanisms such as absorption did not significantly change in this intensity range.

Experimental measurements and calculations using the ROM model for harmonic generation show that the efficiency of second harmonic generation is intensity dependent and becomes efficient only in the relativistic regime $I\lambda^2 > 10^{18}$ Wcm$^{-2}\,\mu$m^2 [Tarasevitch07]. The good agreement between the two indicates that the ROM process is the dominant mechanism in this experiment. CWE, on the other hand, is only weakly dependent on intensity and is efficient at intensities above 10^{16} Wcm^{-2} [Quéré06], which implies that it is unlikely to be a major contribution to our observed SHG. However, the scale length of the plasma at the time of the interaction, which has a significant effect on the efficiency of harmonics generated by either process [Tarasevitch07, Geindre10], was not measured directly. As plasma mirrors were used to make high contrast interactions, it is likely that the scale length was short enough to suppress the generation of plasma waves which has been shown to be crucial for the production of reflected harmonics [Rödel12].

The ROM model can also be used to predict the conversion efficiencies for different angles of incidence and s and p polarisation as is plotted in figure **5.7**. The second harmonic conversion efficiency is predicted to be maximal for an angle of incidence of 50° at p-polarisation. However, this assumes that the absorption remains constant with the changing angle of incidence which may not be the case. The third harmonic generation is most efficient at an angle of 45° for p-polarisation. S-polarisation results in much higher reflectivity at the fundamental wavelength for all angles of incidence.

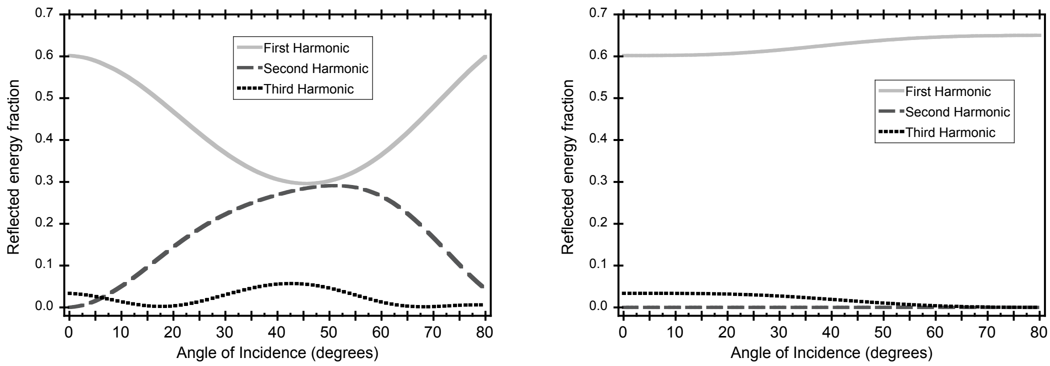

(a) (b)

Figure 5.7: The predicted first, second and third harmonic conversion efficiencies for $I = 1 \times 10^{21}$ Wcm^{-2} assuming a constant 35% absorption a) p-polarisation and b) s-polarisation.

In general, experimental measurements of reflected harmonics could provide a means to determine the plasma scale length during the interaction, as discussed by Rödel [Rödel12]. This would be useful in diagnosing interactions of femtosecond pulses with thin targets for applications such as ion acceleration, where target pre-expansion plays a critical role in the effectiveness of the acceleration mechanisms [Kaluza04].

5.4 Plasma absorption

Figure **5.8** shows that the *total* specular reflectivity (combined ω_0 and $2\omega_0$) of the plasma was approximately constant over the intensity range 10^{17} - 10^{21} Wcm^{-2}. This puts an upper limit on the plasma absorption which does not significantly change with intensity, in contrast with previous results [Ping08, Davies09]. This disagreement is likely due to a differing relationship between intensity and plasma scale length for the different experiments. For high contrast interactions, the scale length can remain short even for very high intensity interactions [Rödel12]. Lower contrast experiments exhibit an intensity threshold at which the pre-pulses become sufficient to expand the target before the arrival of the main pulse. This emphasises the importance of plasma scale length in determining the absorbed fraction of laser energy in this intensity range [Haines09, Kemp08].

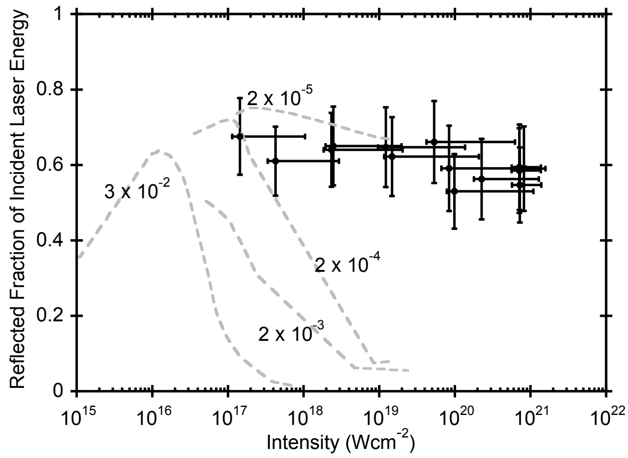

Figure 5.8: Measured total reflectivity as a function of intensity. Combined ω_0 and $2\omega_0$ signal from this experiment is plotted alongside data previously collated in [Pirozhkov09]. Note that the contrast quoted here is the ratio of energy in the ASE to that in the main pulse (as opposed to intensity contrast as used elsewhere in this paper).

There is close correlation between reflectivity for this experiment and for the $E_{\mathrm{ASE}}/E = 2 \times 10^{-5}$ (energy contrast) data set taken with Astra, which shares the same laser components up to the third amplifier of Gemini. In our experiment the ASE pedestal has a relative intensity of 10^{-10}, which begins ≈ 10 ns before the main pulse, so we also obtain $E_{\mathrm{ASE.}}/E \approx 2 \times 10^{-5}$.

5.5 PIC simulations of front-surface harmonic generation

The PIC code OSIRIS was used to perform 2D3V simulations of the experimental interactions. A grid of 21600×21600 cells was divided among 72 nodes of the CX1 cluster. The grid covered 32×32 microns giving a spatial resolution of 1.47 nm. The laser pulse was initialised at the left ($x = 0$) boundary travelling in the positive x direction with the electric field polarised in the y direction. The temporal profile of the laser pulse approximated a gaussian with a FWHM of 30 fs and a central wavelength of 800 nm. The electric and magnetic field diagnostics averaged values over 15 cells, which results in a highest observable harmonic order of $10\,\omega_0$. The target was modelled as a 100 nm thick slab of electrons at 448 n_c with an exponentially decaying plasma on the front surface with a scale length of $\lambda/10$. This estimation of the pre-plasma was taken to match observations with measurements from interactions of similar high-contrast short pulse from Rödel *et al* [Rödel12]. This pre-plasma was also necessary to enable the plasma skin depth to be adequately resolved. When a step-like density profile at aluminium solid density was used the laser was seen to reflect from the target without affecting the plasma. An immobile ion population was simulated to remove the effects of target expansion and hole-boring from simulations making the rapid surface oscillations easier to measure. The target was angled at 45° to the simulation box such that the pulse reflects towards the positive y direction.

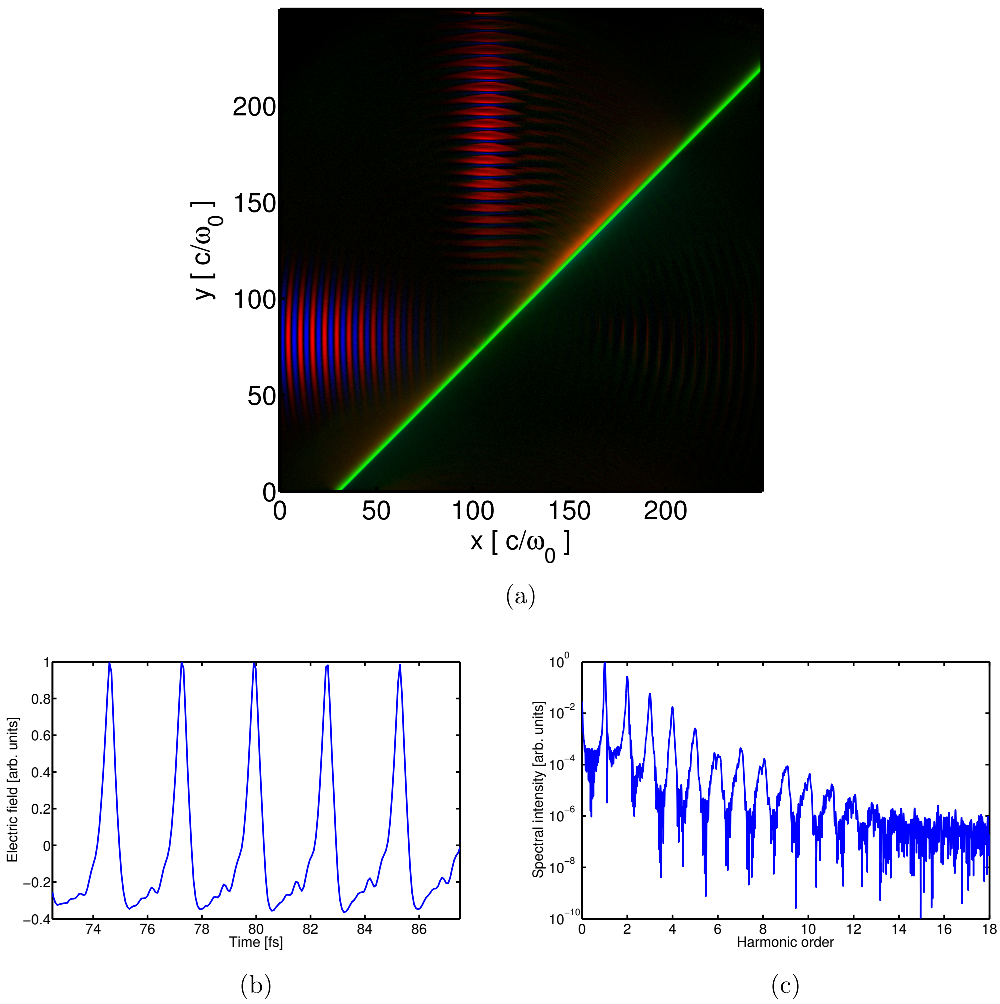

Figure 5.9: (a) Composite image of the electric field (blue to red) and target density (green) at t = 43 fs and t = 133 fs for peak incident intensity of 5.5×10^{20} Wcm^{-2}. (b) 5 periods of the reflected laser pulse electric field. (c) The power spectrum of the reflected pulse.

The reflected laser pulse was measured by calculating the Poynting vector at the lower

y boundary and summing over the x direction. This resultant field as a function of y is equivalent to the temporal field of the reflected laser pulse as it is propagating in free space. This was then used to measure the total reflectivity of the plasma and, by taking the Fourier transform, the energy fraction contained in each harmonic. An example simulation image and the reflected pulse and spectrum are shown in figure **5.9**.

The reflected laser field was observed to be highly asymmetric, indicating that the plasma oscillation is out of phase with the driving electric field by $\pi/2$. This indicates the plasma surface oscillation is a forced harmonic oscillator for which the equation of motion is,

$$-eE_0 \exp(i\omega_o t) = \frac{\mathrm{d}^2 x}{\mathrm{d}t^2} + \zeta\frac{\mathrm{d}x}{\mathrm{d}t} + {\omega_p}^2 x \, , \tag{5.5.1}$$

where ω_p is the natural frequency of the oscillator, in this case the plasma frequency, ω_0 is the laser frequency and ζ is the damping ratio. The solution to this equation is of the form $x = x_0 \exp(i\omega_0 t - \Phi)$ where the phase delay Φ is given by,

$$\tan\Phi = \frac{2\zeta\omega_0}{{\omega_0}^2 - {\omega_p}^2} \, . \tag{5.5.2}$$

For a phase delay of $\pi/2$, $\omega_p = \omega_0$ indicating that the reflecting surface motion dynamics is determined at the critical density surface.

Simulations were performed with the peak a_0 varying from 0.16 to 22.7 to determine the intensity dependence of the emitted harmonics. The energy content of the first three harmonics, relative to the total reflected energy, are plotted in figure **5.10** along with the prediction of the ROM model.

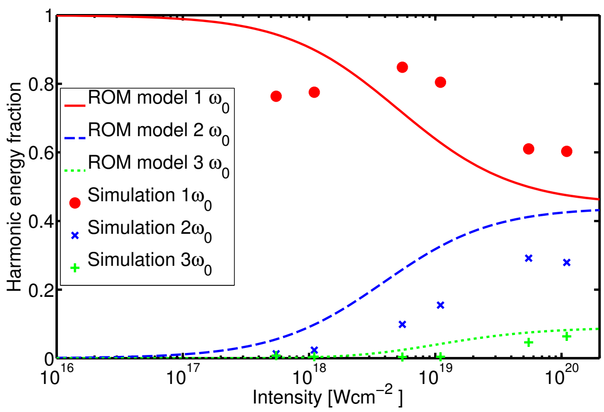

Figure 5.10: Relative harmonic strength in the reflected laser pulse from a 45 degree target from OSIRIS PIC simulations and calculated from the ROM model.

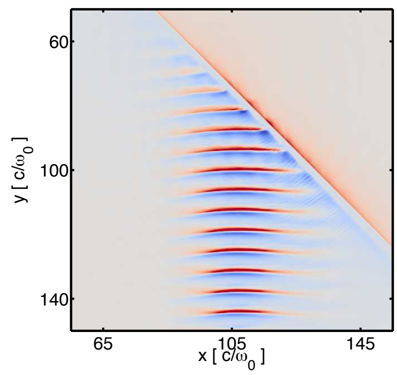

(a)

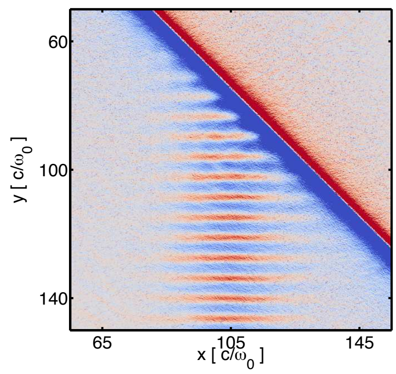

(b)

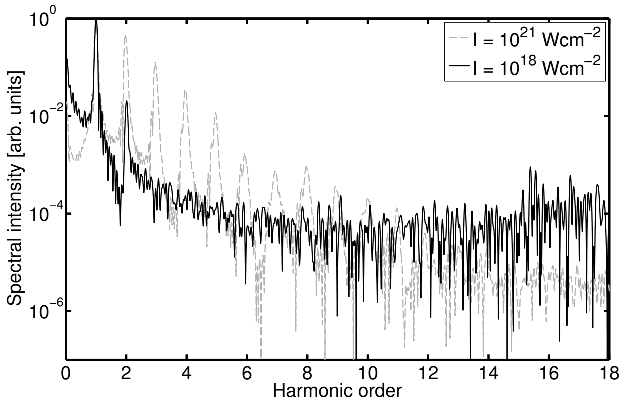

(c)

Figure 5.11: (a) Electric field in the x direction after the laser has reflected from the target for a peak incident intensity of (a) 10^{21} Wcm^{-2} and (b) 10^{18} Wcm^{-2}. Significant noise is observed for the lower intensity case, which results in most of the energy in the spectrum lying outside of the harmonic bands (c), generally at the extreme high and low frequencies.

A similar intensity dependence for the efficiency of the reflected harmonics is seen in the simulation as in both the ROM model and the experimental results. However, the ROM model overestimates the second harmonic efficiency. For $I \geq 10^{20}$ Wcm^{-2}, the simulation values of the first and second harmonic differ from those predicted by our model by approximately 10%. For lower intensities the electrostatic fields generated by particles ejected from the target are comparable to the reflected laser field reducing the visibility of the harmonics. This leads to approximately 20% of the energy in the reflected spectrum lying outside of the harmonic bands (see figure **5.11**).

Rapid heating of the target occurs, partly due to deposited energy but also due to numerical heating as a result of under-resolving the Debye length when the plasma is cold. The numerical heating very rapidly raises the temperature of the electron population so that the Debye length is resolved. For the grid used here this occurs at $T_e \approx 30$ keV. If it is assumed that 50% of the laser energy is deposited evenly through the target over the focal spot area, this temperature would be expected for a laser energy of ~ 0.02 J, corresponding to an intensity of 5×10^{18} Wcm^{-2}. The heating of the target leads to the expansion of the electron population and those which leave the front of the target gain additional energy from the laser field. In addition, the higher plasma temperature allows the laser to propagate further into the target. Both of these effects lead to an artificial increase in plasma absorption, which dominates at lower intensities. This is apparent in the total reflectivity of the target as plotted in figure **5.12**. The total reflectivity from the experiment was seen to drop by only 5% over 4 orders of magnitude in intensity, whereas the simulated values show a large increase with intensity. Very little transmission through the target is observed in the simulations, so this difference is due to plasma absorption. Previous work [Ping08] has shown a gradual increase in absorption over this intensity range, which is in better agreement with our experimental results than the simulations. It is also possible that the scale length of the front surface plasma is different in our experiments to the simulations, or that in reality the pre-plasma shape is not an exponential. The pre-plasma scale length in the experiments is also likely to vary with the peak intensity as the ASE intensity also increases. This effect may work to suppress any intensity dependent absorption effects. The scale length of the plasma has also been shown been shown to play a crucial role in surface harmonic generation [Rödel12]. Therefore, accurate control and diagnosis of this parameter would have great benefit to the understanding and optimisation of harmonic sources generated in this way.

Figure **5.13** shows the plasma surface wave generated by a 10^{21} Wcm^{-2} peak intensity laser pulse. The front surface wave gives rise to harmonics in the reflected laser pulse via the ROM mechanism. Coherent plasma waves are also observed on the rear surface driven by energetic electron bunches, which are accelerated by the laser and travel through the target.

5.6 Conclusions

In conclusion, the conversion efficiency for the generation of second harmonic was observed to be 22($\pm$8)% for intensities greater than 10^{20} Wcm^{-2}. This conversion efficiency is comparable with that achievable with an optimised KDP or BBO frequency doubling crystal for a ≈ 50 fs pulse but without the adverse problems of group delay dispersion and

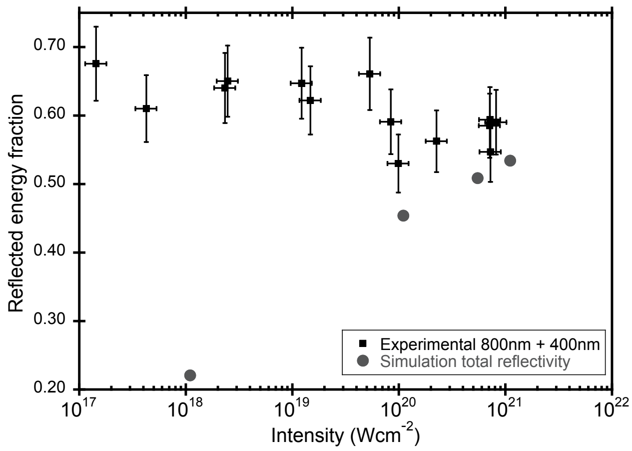

Figure 5.12: Total plasma reflectivity from OSIRIS PIC simulations plotted with experimental measurements of the reflectivity into $1\omega_0$ and $2\omega_0$.

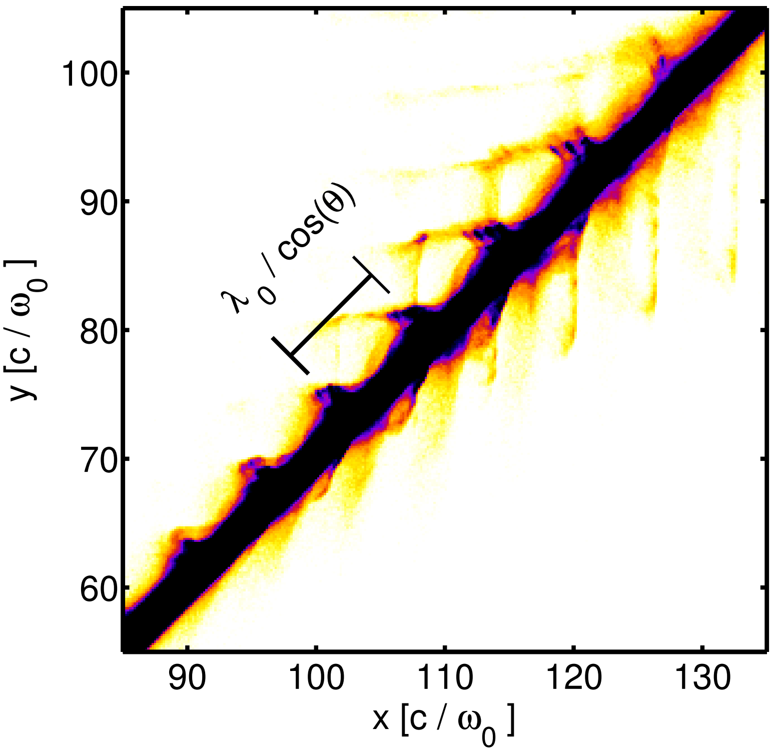

Figure 5.13: Snap shot of the electron density distribution at 100 fs into the simulation. Surface waves are observed leading to the generation of harmonics in the reflected laser pulse.

reduction in spatial coherence [Marcinkevicius04, Mironov09], provided that the quality of the plasma surface is maintained. Optimising this process would allow for extremely high contrast and high intensity laser plasma interactions with 400 nm ultra-short pulses.

A model based on the relativistic oscillating mirror concept agrees well with the observed reflectivities. This indicates that this is the dominant mechanism for second harmonic generation for the intensity range 10^{17} - 10^{21} Wcm^{-2} for ultrashort pulses with high contrast. The model also suggests that the conversion efficiency into the second harmonic with this process saturates at $\approx$ 22% for intensities $>10^{19}$ Wcm^{-2} at a 35° angle of incidence. Simulations indicate that the surface oscillation behaves as a forced harmonic oscillator with a natural frequency equal to the laser frequency. The reflected electric field is subsequently asymmetric with temporal compression of the electric field occurring at half of the peaks.

In addition, the specular reflectivity of the plasma reveals that plasma absorption remains nearly constant over four orders of magnitude in incident laser intensity. This differs from previous measurements, which we attribute to the high contrast of these interactions. The slight drop in reflectivity in the first and second harmonic is matched by calculations using the ROM model with an assumed constant 35% absorption. This indicates that the majority of this lost energy is actually present in higher order harmonics which were not measured experimentally.

Chapter 6

Temporally Resolved Measurements of the Laser-Plasma Boundary Motion in Solid-Density Interactions

The increase in achievable laser intensities above 10^{20} Wcm^{-2} has triggered research into radiation pressure ion acceleration. In the overwhelming majority of experiments to date the dominant process of ion acceleration from solid density targets has been interpreted as sheath acceleration [Clark00, Snavely00, Fuchs05] (section 2.5.1), whereby energetic electrons, produced at the laser-plasma boundary, expand outwards and create electrostatic fields at the plasma-vacuum interfaces. These fields accelerate ions away from the target to energies of >MeV per nucleon. For thick targets, electrons gain energy while in the focal region of the laser but are quickly shielded from the accelerating fields by the bulk of the plasma. For very thin targets (on the order of a few skin depths) the laser field can effectively accelerate electrons throughout the entire depth of the plasma for the duration of the pulse (τ). For this mechanism, termed radiation pressure acceleration (RPA) [Esirkepov04, Robinson08], laser energy is more efficiently converted to the energy of the ions (ϵ_i), which scales with intensity (I) and the areal density (σ_A) of the target as,

$$\epsilon_i = \frac{m_i}{2}\left[\frac{\tau I}{c\sigma_A}(1+R)\right]^2, \tag{6.0.1}$$

in the non-relativistic case, where R is the reflectivity of the plasma surface. This compares favourably with the $(I\lambda)^{1/2}$ scaling seen for sheath acceleration. However, for currently available laser systems the maximum achievable ion energies by either sheath acceleration or RPA are similar.

An intermediate process, which can also lead to the acceleration of ions is hole-boring acceleration, during which radiation pressure drives the laser-plasma boundary into the target. This occurs for targets that are thicker than the skin depth such that the laser pressure is only affecting the front surface. Ions are reflected by the electrostatic field at this boundary to twice the hole-boring velocity ($2v_{hb}$), giving an ion energy of,

$$\epsilon_i = \frac{I(1+R)}{cn_i}, \tag{6.0.2}$$

where n_i is the ion number density. Therefore, the energy of ions accelerated by hole-boring acceleration may be linear with laser intensity for a fixed density. As the laser-plasma boundary propagates through the target, it may eventually reach a light-sail phase if $v_{hb}\,\tau > d$, where d is the target thickness.

It is typically difficult to determine exactly which mechanisms have lead to an experimentally observed ion spectra due to the complex and time-varying nature of the interaction. For thin targets, it is likely that a combination of all of these mechanisms are involved so more information about the dynamics of the laser-plasma interaction is required in order to characterise and optimise the resultant ion beams.

Signatures of RPA and hole-boring acceleration are recorded by the reflected laser pulse, due to the motion of the laser-reflecting surface. Previous experimental work has used the reflected laser spectrum to determine the surface acceleration [Sauerbrey96]. However, a number of assumptions are required in order to obtain quantitative results and as such this approach can yield only an approximate answer. More recent results [Ping12] have used a frequency-resolved optical gating (FROG) diagnostic (section 3.2) to obtain the time-resolved second harmonic emission spectrum from a 1.4 ps interaction at 5×10^{19} Wcm^{-2}. This allows a much more qualitative determination of target evolution during the interaction by tracking the front surface motion.

This chapter contains measurements of the motion of the laser-reflecting surface during the interaction of the Astra Gemini Laser with nanometer-scale diamond-like carbon (DLC) [Ma11] targets at a peak intensity of 2×10^{20} Wcm^{-2}.

6.1 Experimental setup

An experiment was performed using a single beam of the Astra Gemini laser at the Rutherford Appleton Laboratory. Each pulse initially contained ≈ 8 J and had a pulse length of 50 fs (FWHM). Double plasma mirrors were used to enhance the laser contrast to 10^{10} with a throughput of 50% resulting in ≈ 4 J on target. An $f/2$ off-axis parabolic mirror was used to create a 2.5 μm focal spot (FWHM) containing 25% of the pulse energy. Targets of diamond-like carbon (DLC) of thickness $3.5 - 1000$ nm were used. The focusing parabolic mirror had a central 1 cm diameter hole which was used to sample the back-scattered laser energy. Two Grenouilles (commercial SHG-FROGs, see section 3.2) were used to characterise the temporal properties of the back-scatter pulse. An optical spectrometer also measured the time integrated spectrum of the back-scattered radiation. A single additional Grenouille was used to measure the temporal properties of the transmitted pulse as sampled by a reflective mirror. A layout of the experiment is shown in figure **6.1**.

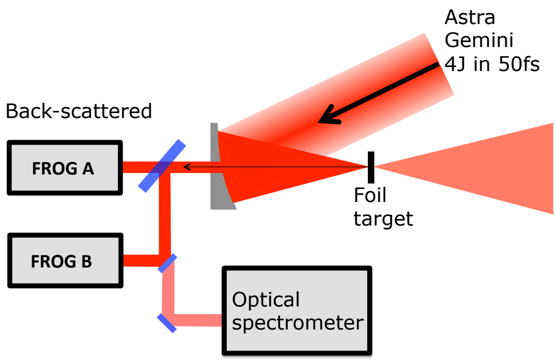

Figure 6.1: Schematic of the experimental setup showing the back-scattered and transmitted pulse diagnostics. The incoming beam is contrast enhanced by double plasma mirrors.

6.2 DLC thickness scan

DLC targets of thickness $3.5 - 1000$ nm were shot at $0°$ angle of incidence and with linear polarisation. FROG images of the back-scattered pulses were recorded and the pulse profiles were retrieved. Some example images of the retrievals are shown in figure **6.2**.

For each shot there were two possible retrieved pulses for each FROG trace, due to the time-direction ambiguity of the autocorrelation process. However, an extra 5.5 mm of fused silica was placed in the path to FROG A compared to FROG B. Therefore, by mathematically back-propagating both potential solutions for the FROG A pulses

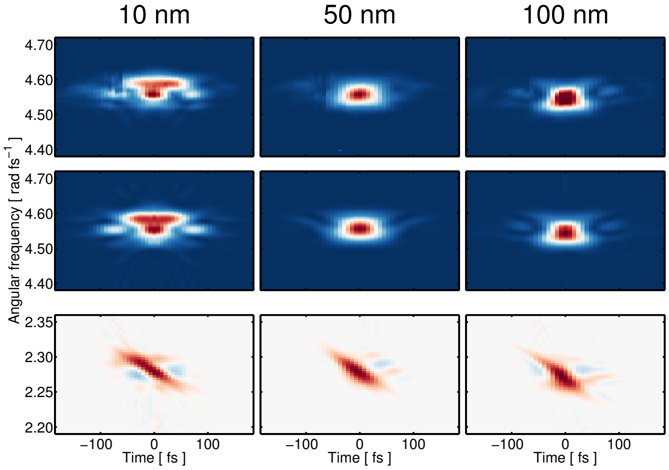

Figure 6.2: (Top row) Measured FROG images, (middle row) retrieved FROG images and (bottom row) Wigner distributions of the reflected laser pulses. Target thickness is given above each column.

through this extra glass, it was possible to determine the correct direction of time. This is most easily seen through the Wigner distribution [Wigner32], which gives a visual representation of the time dependent spectrum of the pulse. Figure **6.3** shows the Wigner distributions for both potential retrieved pulse shapes from each diagnostic. The Wigner distribution is only the same from both diagnostics for the case of negatively chirped pulse. This was done for all shots for which retrievals were obtained from both FROGs, thereby determining the chirp for each pulse and removing the time-direction ambiguity in the diagnostic. For shots on which only one FROG retrieval was possible, the time-direction could not be determined and so were excluded from the results.

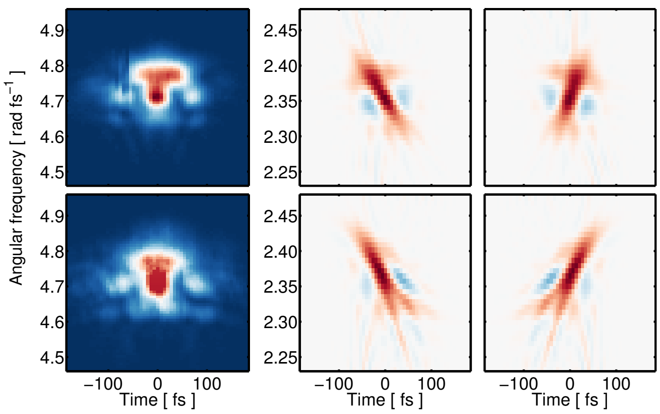

Figure 6.3: The measured FROG image and the Wigner distributions of the two retrievals from (top row) FROG A and (bottom row) FROG B.

The Wigner transform of the retrieved pulses gives a 2D representation of the pulse energy in time-frequency space. This was used to find the central frequency of the pulse as a function of time by calculating the center of weight of the spectrum at each time step. The values below 3σ ($3\times$ standard deviation of the Wigner distribution) were set to zero to remove the effect of noise in this calculation. The temporal range over which the central frequency was calculated was limited to points in the Wigner distribution where the maximum was greater than 3σ, where σ is the standard deviation of the distribution.

Assuming that the frequency shift of the pulse is entirely due to the motion of the reflecting surface the recession velocity is given by $v/c = (\omega_i - \omega_r)/\omega_r$, where ω_i and ω_r are the frequency of the incident and reflected pulses respectively. The incident pulse was measured to have a negative chirp so the frequency, ω_i, also varies in time. For all pulses $t = 0$ was set at the maximum of the pulse envelope and the surface velocities obtained are shown in figure **6.4**.

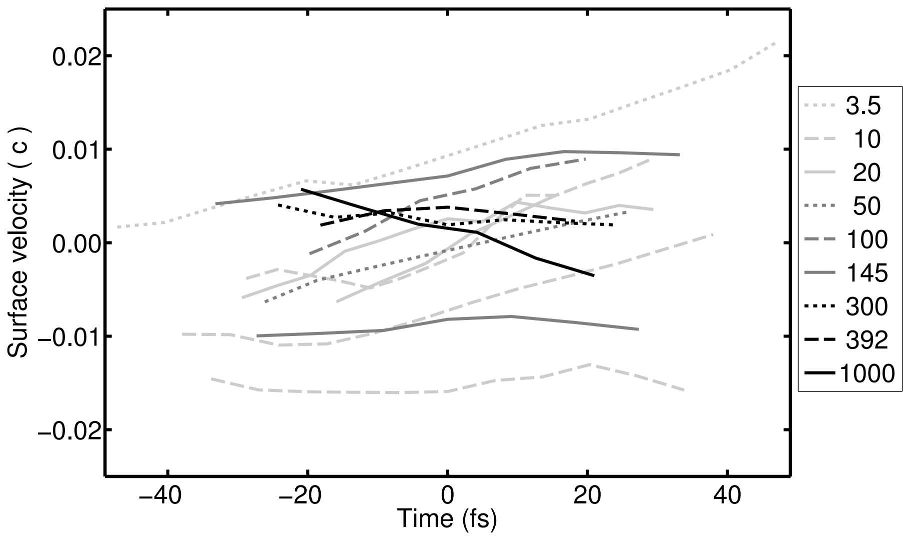

Figure 6.4: Surface velocity as a function of time relative to the reflected pulse envelope for targets of 3.5−1000 nm thickness. Positive velocities correspond to motion of the reflecting surface away from the laser.

The surface velocities of the targets show significant variation in their absolute position but the slope of the lines clearly varies over the thickness range. The 1000 nm target shows an initial recession from the laser but as the interaction progressed this changes to motion towards the incoming laser. For targets below 145 nm in thickness the acceleration is observed away from the laser. The variation of initial observed velocities indicates that the plasma conditions evolve significantly before the observation window of the diagnostic.

The pulse intensity is already greater than 10^{15} Wcm^{-2} at $t \approx -100$ fs whereas the diagnostic was only able to retrieve velocity information up to $t \approx -30$ fs for most targets. Also, pre-pulses and residual A.S.E. may cause target heating and expansion picoseconds before the main pulse. The fluctuation in the pre-pulse levels from shot to shot may result in a rather large differences in plasma conditions.

The initial and final observed surface velocity for each shot is plotted against target density in figure **6.5**. A general trend is seen that the largest reflecting surface velocities towards the laser is seen for targets thicknesses of 10–50 nm. For thicker targets, and also the single shot with a 3.5 nm target, the reflecting surface was seen to be initially receding from the laser. It would perhaps be expected that the thinner targets would be more easily pushed by the radiation pressure of the laser, due the lower density caused by the expansion of the target. However, a lower density target may also be heated more efficiently, due to the increase in plasma skin depth, resulting in a higher temperature and therefore a larger plasma pressure. The final observed surface velocities show an increasing recession for thinner targets. This would be expected from the thermal expansion of the plasmas, which would lead to a larger decrease in plasma density for thinner targets. Using equation **2.5.4**, $v_{\text{hb}} \approx 0.005c$ for a laser intensity of 2×10^{20} Wcm^{-2} and assuming 100% reflection from a pure DLC target. The majority of the final measured

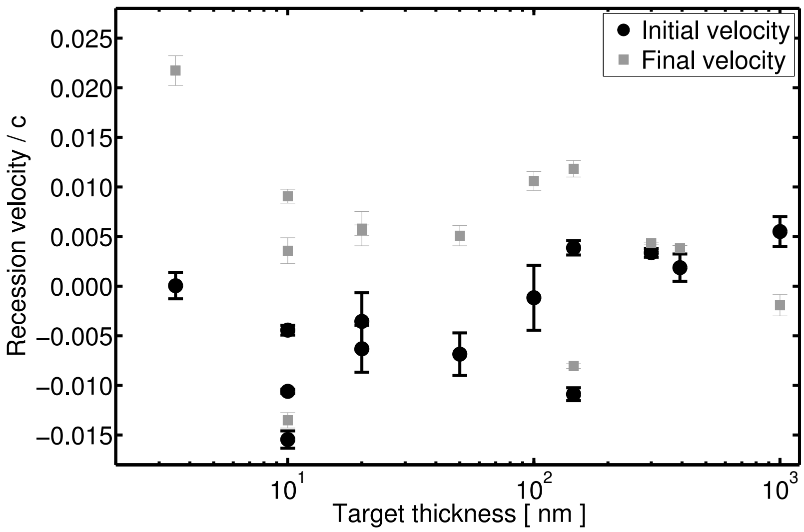

Figure 6.5: Initial and final surface velocity as a function of target thickness. Positive velocities correspond to motion of the reflecting surface away from the laser. The error bars are taken from the standard deviation of the surface velocity values from the first 10.3 fs, which corresponds to the standard deviation in measured pulse length.

surface velocities are of this order, although there is significant variation.

The motion of the laser-reflecting surface is due to the balance between the thermal expansion and the radiation pressure of the laser. The observation of surface recession indicates that the radiation pressure is dominant, whereas the surface will expand towards the laser if the thermal pressure is dominant. As the plasma expands it will also become less dense, so without any increase in laser intensity the surface may seem to accelerate away from the laser purely due to the drop plasma pressure. Conversely, hole-boring into the target may create an increase in density, which will begin to resist further compression.

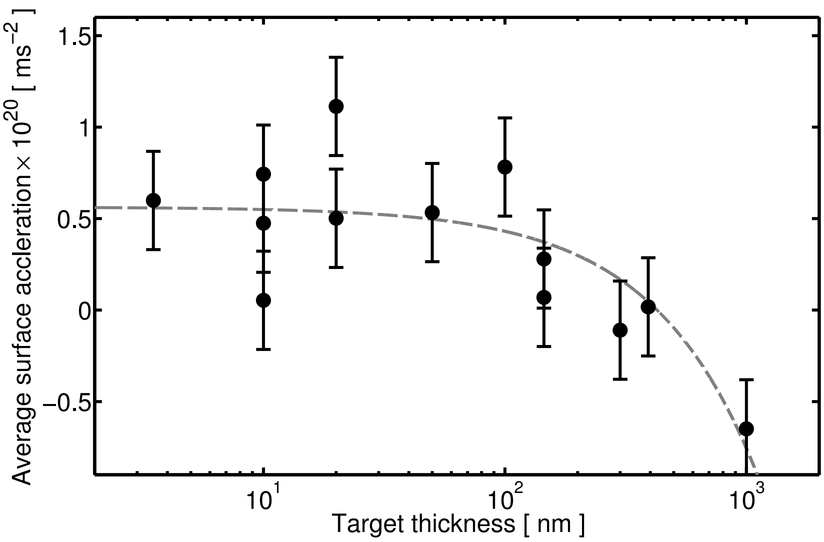

Figure 6.6: A graph of the average surface acceleration measured by FROG diagnostics on the back-scattered laser pulse. The values are calculated over the temporal intensity FWHM of the reflected pulse. The error bars are calculated as a RMS error from the linear fit plotted as the dashed line. A positive acceleration is in the direction away from the incoming laser.

The average acceleration for each shot is plotted against target thickness in figure **6.6**. This shows a clear trend for thinner targets to experience a much stronger acceleration away from the laser. A linear fit of the form $\dot{v}(d) = \dot{v}_0 + md$ was found for $\dot{v}_0 = 0.56 \times 10^{20}$ ms^{-2} and $m = -1.3 \times 10^{17}$ ms^{-2}nm^{-1} with an RMS error of 0.27×10^{20} ms^{-2}. The existence of negative accelerations demonstrates that pure light-sail or hole-boring acceleration does not occur for the thicker targets. For the 3.5 nm target the 1D light-sail model would obtain a much higher acceleration than observed. This indicates that the acceleration measured is a result of the balance between the radiation pressure and the plasma pressure. In addition, the peak proton energies observed during the experiment were 5–10 MeV, much higher than would be expected from the hole-boring or light-sail mechanisms for the observed surface velocities.

For a stationary laser-plasma boundary, the radiation pressure of the laser pulse is balanced by the thermal pressure of a plasma (modelled with the ideal gas law) with density and temperature given by,

$$n_e k_b T = \frac{2I(1+R-T)}{3c}. \tag{6.2.1}$$

For $I = 2 \times 10^{20}$ Wcm^{-2} and a solid density plasma then $k_b T \approx 70$ KeV for equal thermal and radiation pressures. For expanded targets, with lower plasma density, this equilibrium temperature is much higher and is in the MeV range for $n_e \approx 10 n_c$.

6.2.1 Forward harmonics as a diagnostic of plasma frequency

Target surface motion measurements indicate that the laser radiation pressure is opposed by the plasma pressure for all DLC targets in the thickness range 3.5 − 1000 nm. This demonstrates that even for the thinnest target the plasma remains overdense for the majority of the interaction. This is also supported by the transmitted laser energy measurements (see figure **6.8**) which show that the majority of the laser energy is reflected or absorbed for all targets. In order to determine the target density during the peak of the pulse the harmonic spectrum in the laser forward direction was measured with a transmission grating and CCD coupled MCP (micro-channel plate). The resultant images were analysed and converted to spectra by J.H. Bin [Bin]. The detector range allowed observation of harmonics in the range of $7\,\omega_0 - 19\,\omega_0$.

Assuming that each target is pre-expanded by the same distance, then the peak density will be lower for initially thinner targets. Forward harmonics generated by the coherent wakefield emission (CWE) mechanism [Quéré06] exhibits a cut-off frequency determined by the peak plasma frequency in the target (see section 2.6). Figure **6.7** shows the observed cutoff harmonic order as a function of target thickness. These measurements are consistent with the density drop expected for an increase in the thickness of each target by 15 nm. This measurement does not take into account that the target may evolve during the main pulse or that there may be spatial variations in the target density. Also, the equation used to calculate the peak density assumes the plasma-frequency is given by the non-relativistic formula. For our interactions the peak $a_0 > 1$ and so it is likely that the plasma frequency would be modified by the relativistic quiver motion of the electrons. However, previous work [Sheng05] has shown that the CWE process only generates harmonics for p-polarised interactions. As pointed out by Hörlein *et al.* [Hörlein11] for normal incidence, the curvature of the target surface, due to the radial intensity profile of the laser focus, leads to a p-polarised component of the laser, which can lead to the generation of CWE harmonics.

6.2.2 Target transmissivity

A scattering screen was placed to sample part of the transmitted laser pulse which was then imaged with a CCD camera. This gave a measurement of the transmitted laser energy for the 5, 10 and 15 nm targets, which was provided by J. H. Bin [Bin]. The transmissivity can also be calculated using the expanded target density and thickness information gained from the harmonic diagnostic using the relativistic equation for the skin depth,

$$\delta_s = \frac{c}{\omega}\left(\frac{n_e}{\langle\gamma\rangle\, n_c} - 1\right)^{-\frac{1}{2}} \quad . \tag{6.2.2}$$

The experimental data is plotted in figure **6.8**, alongside calculated values for various values of $\langle\gamma\rangle$. The curves in figure **6.8** were found by taking the pre-expanded target thicknesses and densities (section 6.2.1) and then calculating the skin depth from equation **6.2.2** with a fixed value for $\langle\gamma\rangle$. It was assumed that the targets had constant density and sharp boundaries and that there was no absorption. It was also assumed that the target did not evolve during the interaction of the laser pulse. A further calculation was

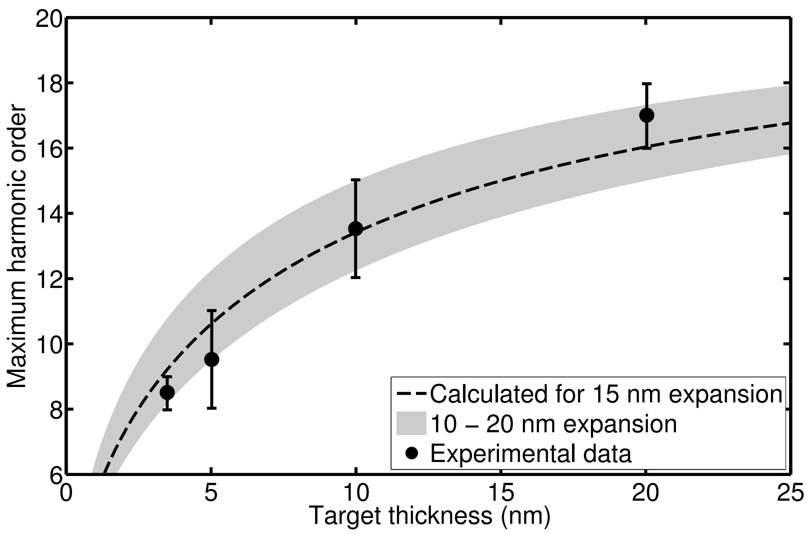

Figure 6.7: Measured maximum harmonic order and calculated values from the maximum plasma density of a pre-expanded target. The expected range for targets pre-expanded by 10–20 nm is shaded grey.

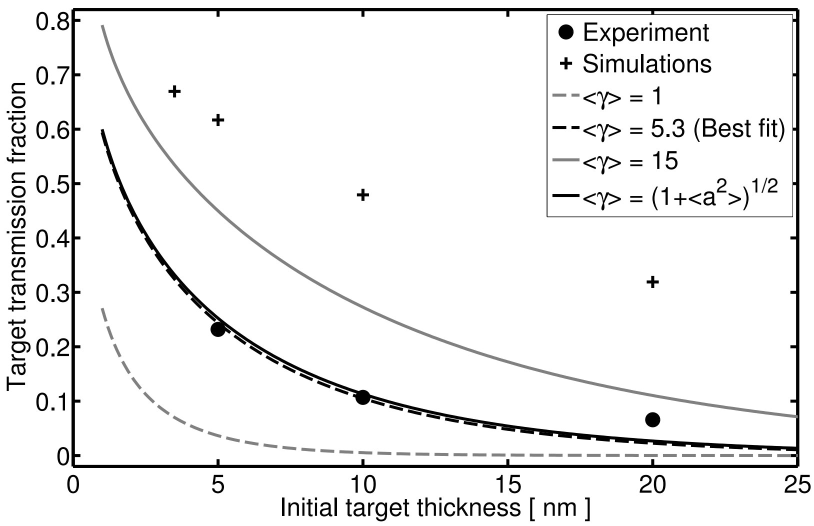

Figure 6.8: Measurements of transmitted laser energy fraction from experiment and 2D OSIRIS simulations, plotted against target thickness. The lines show the values calculated from the pre-expanded target thickness and density and for various values of $\langle\gamma\rangle$, as given in the legend. The solid black line is calculated for a gaussian approximation to the Gemini laser pulse and shows very close agreement with the best statistical fit for $\langle\gamma\rangle = 5.3$.

made using a time-varying $\langle\gamma\rangle$ defined as

$$\langle\gamma\rangle = \sqrt{1 + \langle a^2 \rangle}, \tag{6.2.3}$$

where the magnitude of the normalised vector potential, a was calculate for a 50 fs gaussian intensity profile with a peak intensity of 2×10^{20} Wcm^{-2}. The transmitted energy fraction was then calculated as,

$$\mathcal{E}/\mathcal{E}_0 = \left[\int_{-\infty}^{\infty} I(t)L(t)dt\right] / \left[\int_{-\infty}^{\infty} I(t)dt\right] , \tag{6.2.4}$$

$$L(t) = \exp\left[-\left(\frac{d}{\delta_{\mathbf{s}}(t)}\right)^2\right] . \tag{6.2.5}$$

This shows a very good agreement with the best fit to the experimental data (with a fixed $\langle\gamma\rangle = 5.3$), indicating that this rather simplified model can reproduce observations relatively accurately. A more physical model would require information as to the dynamic expansion of the target during the interaction, and a more rigorous calculation for the relativistic skin depth [Weng12].

Results from 2D PIC simulations (see section 6.3) are also plotted which show a much higher transmitted energy fraction than observed experimentally. This is caused by the dynamic expansion of the target during the interaction, which causes the plasma to go underdense in the case of the thinner targets

6.3 Simulations

For a plasma with a front surface density gradient, the laser reflects from all regions where $n_e > \langle\gamma\rangle n_c$. The proportion of energy reflected as the laser propagates is given by the complex index of refraction. So for a diagnostic measuring the Doppler shift of a laser reflecting from a complex plasma target there is a question over what surface is actually being tracked. 2D3V particle-in-cell (PIC) simulations were performed using the code OSIRIS [Fonseca02] to determine how the reflected laser is modified by the time-varying target density profile.

The simulation box covered an area of 25.5 μm by 25.5 μm divided into 32000 cells in the laser propagation direction and 3960 cells in the transverse direction. This gave a spatial resolution of 0.8 nm and 6.4 nm in the longitudinal and transverse directions respectively. The laser was modelled with a gaussian temporal envelope of 50 fs , a peak a_0 of 12 at a wavelength of 800 nm and a focal spot width (FWHM) of 2.5 μm. The laser entered the simulation from the $x = 0$ boundary propagating in the positive x direction with the electric field polarised in the 2D plane of the simulation. The DLC targets were modelled as fully ionised 90% carbon and and 10% hydrogen by number with an initial uniform electron density of 450 n_c with 400 particles per cell per species. Simulations were performed with initial thicknesses of 3.5, 5, 10, 20, 50 and 100 nm. Each target was assumed to have been pre-expanded by 15 nm (as taken from the experimental measurements of peak transmitted harmonic order), with the densities adjusted to conserve mass. The targets were initialised with zero temperature and the front surface was positioned at $x = 150\ c/\omega_0$. The spatial resolution of the simulation grid resolves the Debye length at the peak plasma density for a temperature of ≈ 7 keV. This temperature is much lower than expected for heating by the laser and so numerical heating is not expected to play a significant role.

The transmitted laser energy for each simulation was calculated by summing the Poynting vector ($E_y \times B_z$) in the region behind the target and dividing by that sum for the incident pulse. These values are plotted in figure **6.9** and show a considerably larger transmissivity for the targets than observed experimentally. Even for the thickest target simulated, 100 nm, 13% transmission was seen, similar to the experimental value for the 10 nm target. This indicates that the targets are not evolving as seen in experiments. This

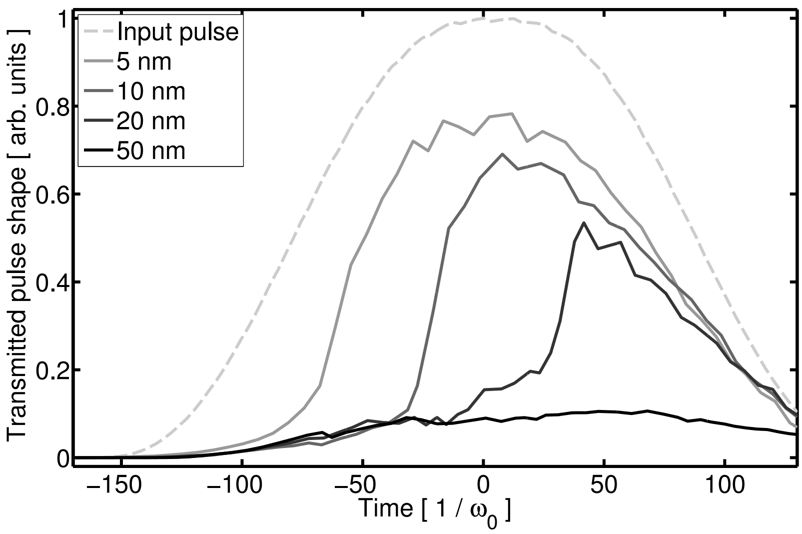

Figure 6.9: Transmitted pulse shapes from 2D Osiris simulations. The initial pulse shape is shown as the dashed line and the solid lines are the pulse shapes measured behind the target. The pre-expanded targets are used with initial target thicknesses (before pre-expansion) given in the legend.

could be an effect of the 2D geometry or perhaps that the targets are not initialised in the correct state to match the experiments. There may also be a significant contamination layer on the real targets, so that they are in fact thicker than the DLC thickness.

The dynamic expansion of the targets is seen by measuring the temporal profile of the laser pulse as it passes the $x = 200\ c/\omega_0$ boundary. In this case the Poynting vector is summed only in the y direction and built up over many data-dumps. The pulse profile was also measured at the $x = 0$ boundary to give the incident pulse profile. The profiles are displayed in figure **6.9** and show a decrease in the transmitted pulse length as the target thickness increases. A sharp rising edge is observed for the 10 and 20 nm targets which occurs as the laser bores through the target. For thicker targets this does not occur as the plasma density remains high in the region of the laser focus. The 3.5 and 5 nm targets become relativistically underdense during the rising edge of the pulse and so the transmitted pulses do not have such a sharp rising edge.

In order to study the laser-reflecting surface in the simulations, the reflected laser was measured at the $x = 0$ boundary, once the ingoing pulse left this area. The field of the reflected pulse was recorded by summing the electric field (E_y) of the laser in the transverse (y) dimension over $x = 0 - 25\ c/\omega_0$. This measurement was repeated at time intervals of $25/\omega_0$ and the reflected pulse was built up from combining each slice as shown in figure **6.10**. The time dependent intensity was taken as the values of the electric field

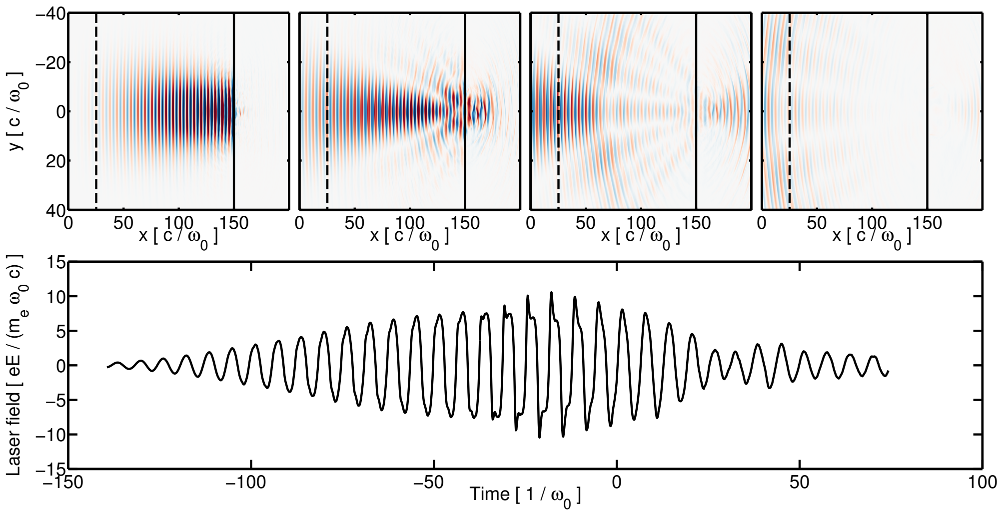

Figure 6.10: (Top row) Images of the laser field in a PIC simulation entering from the left boundary and reflecting from a 20 nm (pre-expanded to 35 nm) DLC target. The four pictures show the simulation at (from left to right) $t = 139, 160, 181$ and 203 fs. The reflected pulse (bottom) is measured by taking the reflected pulse to the left of the black dashed line at each time step and combining each section to reconstruct the entire reflected pulse.

at the turning points of the recorded pulse. The crossing points of the electric field were used to obtain the time dependent wavelength. This allowed the velocity of the laser-reflecting surface to be calculated from the Doppler shift of the laser. The position of the laser-reflecting surface was determined by integrating the time dependent surface velocity, in the same manner as for the experimental results.

For the 20 nm simulation, the target is seen to act as a mirror until the peak of the pulse arrives at the target at which point it is seen to 'hole-bore' through allowing a much higher proportion of the laser to propagate through the target. When this initially occurs, the plasma acts to focus the pulse to a smaller high intensity spot which then diffracts at a large angle. This is evident in the highly curved wavefronts seen in the $t = 160$ fs and $t = 181$ fs simulation E_y images (figure **6.10**). As a consequence the reflected laser pulse is shorter in duration than the incident pulse with a FWHM pulse duration of 29 fs. For thinner targets the target is penetrated at earlier times, while targets with thicknesses of 50 nm or greater survive the entire pulse.

Figure **6.11** illustrates the plasma expansion of an initially 35 nm target with $n_e = 257\, n_c$. Each line is an isopycnic (of constant density), which shows how the longitudinal position for a particular electron density surface changes with time. Also plotted is the line for the relativistic critical density surface with $\langle\gamma\rangle = \sqrt{\langle a^2\rangle + 1}$, where a is given by the intensity

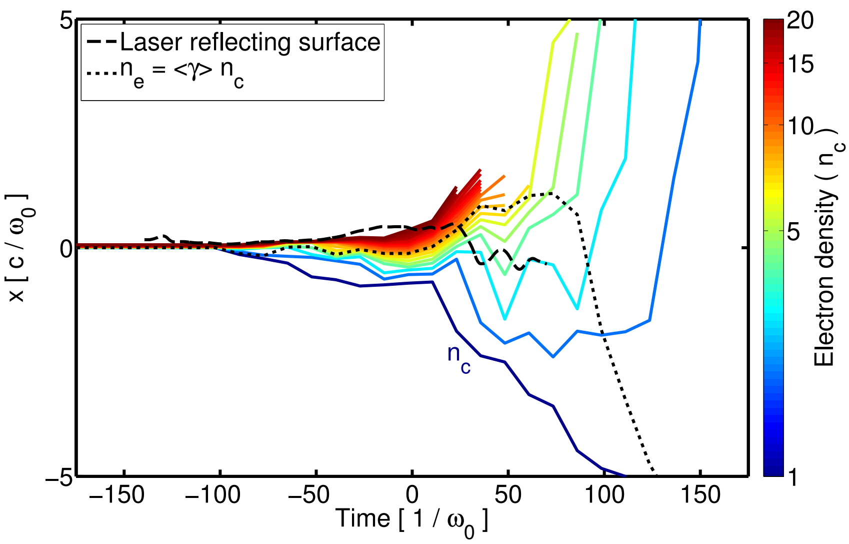

Figure 6.11: Longitudinal position of the surfaces with $n_e = 1 - 20\ n_c$ as a function of density (solid lines) for the simulation of a 20 nm target. The lines terminate where the peak density of the target drops below that of the surface being plotted. The surface with $n_e = \langle\gamma\rangle\, n_c$ (fine dashed line) and the laser-reflecting surface (long dashed line) are also plotted. Zero time is the time at which the peak of the laser pulse reaches the initial target plane. The positive x direction is away from the laser and positive time is later in the simulation.

of the laser pulse as it would be in vacuum at the target surface. The laser-reflecting surface is found from the frequency shifts of the reflected laser as described above. It is observed that the target expands from both the front and rear surfaces with the peak density position moving away from the laser and the critical density surface moving towards the laser. The laser-reflecting surface does not follow any of these surfaces, nor does it follow the relativistic critical density surface.

The laser-reflecting surfaces from the range of simulations performed are shown in figure **6.12**. They show a trend of a greater surface recession for thinner targets with the 50 nm and 100 nm targets expanding towards the laser. This qualitatively matches the experimental observations, although in the experiment outward expansion was only observed for thicker targets (392 nm and 1000 nm). In addition, in the simulations the 50 nm target was seen to expand further towards the laser than the 100 nm target and average accelerations of the targets calculated from the simulations do not match the experimental data.

For the simulations of thicker targets it is seen that, at late times, the apparent reflecting

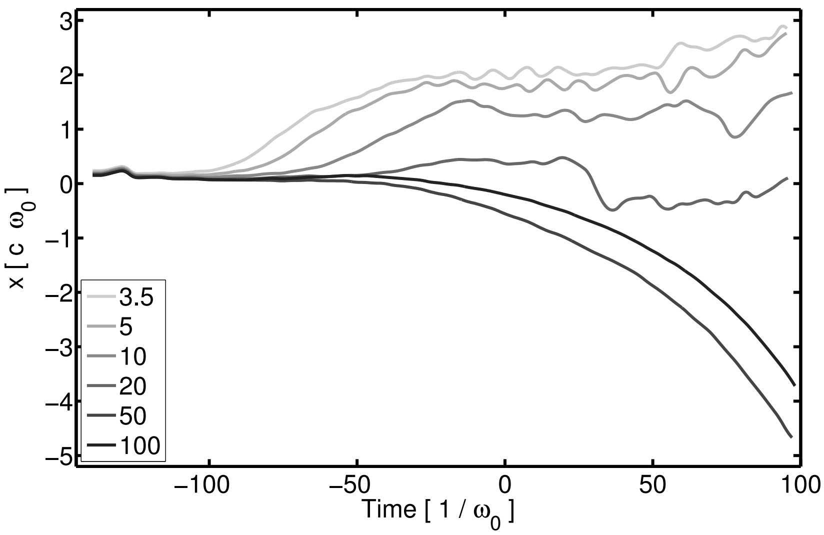

Figure 6.12: Laser-reflecting surface as a function of time for simulations of different target thicknesses. The initial target thickness in nm (before pre-expansion by 15 nm) is given in the legend. Axes follow same pattern as figure **6.11**.

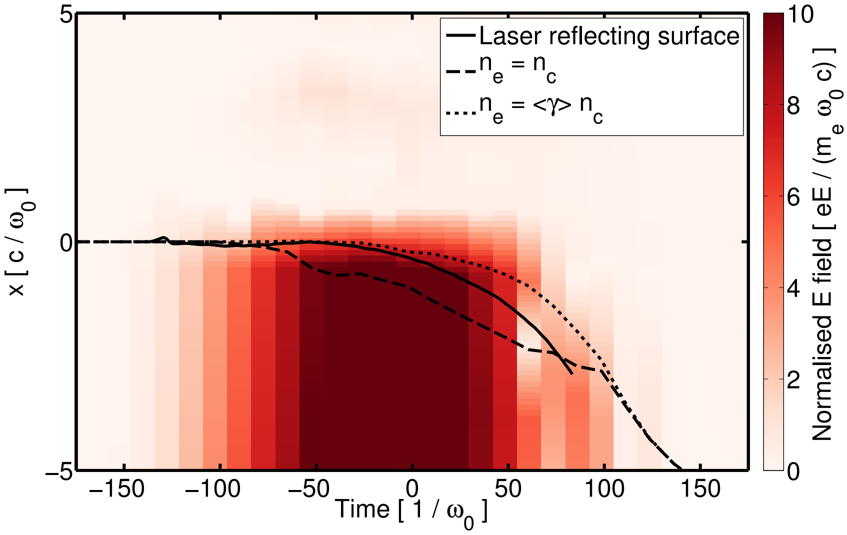

Figure 6.13: On-axis transverse electric field strength (E_y) as a function of time for an initially 100 nm target. Also plotted are the laser-reflecting surface (solid line) and the relativistic (fine dashed line) and non-relativistic (long dashed line) critical density isolines.

surface is before the critical density surface. This is illustrated in figure **6.13** which shows the surface positions plotted on an image of the normalised electric field as a function of time for the simulation of the 100 nm target. Here, it is seen that the position where the electric field of the laser is attenuated lies between the relativistic and non-relativistic critical surfaces whereas the the laser-reflecting surface, as calculated from the phase of the reflected pulse, is further towards the incident laser. This is also seen for the 50 nm target simulation. For both of these simulations there is a large amount of underdense plasma in front of the target at late times, as compared to the thinner targets, indicating that the plasma modifies the observed laser frequency. It has been previously seen that for interactions at an normal incidence onto a sharp plasma boundary the phase change to the reflected laser follows the Doppler relationship [Kingham01]. However, with the existence of a tenuous plasma in front of the reflecting surface, the propagation of the laser through this plasma becomes important. For a rapidly expanding plasma, the temporal dependence on the refractive index leads to a time varying phase velocity for the laser. This can modify the temporal phase of the laser pulse and cause an apparent frequency shift even for a static reflecting surface. Also the locally changing refractive index in the underdense plasma can cause photon acceleration (see section 2.7.7), as given by,

$$\frac{\mathrm{d}\omega}{\mathrm{d}t} = -\omega \frac{\partial}{\partial t} \ln \eta \, . \tag{6.3.1}$$

So, as the laser propagates to and from the reflecting surface, it picks up an additional frequency shift from the local rate of change in electron density. It is conceivable that this effect could blue-shift or red-shift the pulse depending on the particular dynamics of the underdense plasma. In the case of the 100 nm simulation, the underdense plasma density increases throughout the simulation, which would correspond to a blue-shift effect.

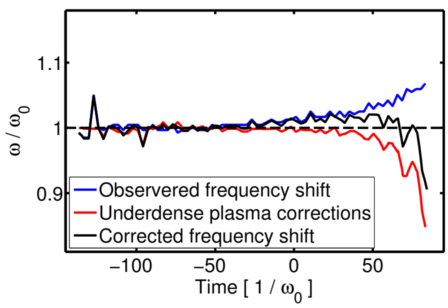

(a)

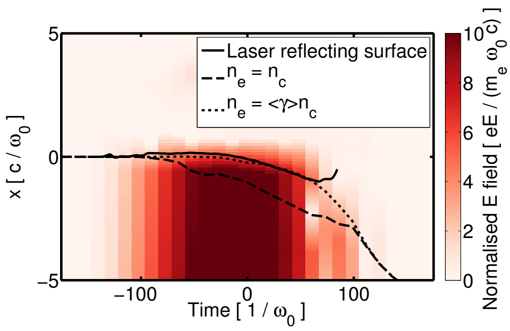

(b)

Figure 6.14: (a) Observed frequency shifts, calculated correction due to the effect of underdense plasma and the corrected frequency shifts. (b) Laser reflected surface after correcting for the underdense plasma.

The effect of photon acceleration on the reflected laser pulse in the simulations was calculated by following the paths of all the light rays of the observed reflected laser back through the simulation electron density data, interpolating between dumps. This was then used to calculate the change to the temporal phase of the laser due to the phase velocity in the underdense plasma. The frequency shifts caused by photon acceleration were also calculated and subtracted from the measured frequency shifts leaving only the relativistic Doppler effect, as shown in figure **6.14**. The calculated laser-reflecting surface position, after these corrections, lies close to the relativistic critical density surface up until late times. After $t = 50/\omega_0$ the frequency shifts appear to be over-corrected as the reflecting surface lies beyond the relativistic critical density surface. At this point the differences between consecutive data-dumps from the simulation are large and the linear interpolation between them becomes unrealistic.

Photon acceleration and time varying phase velocity will affect the instantaneous frequency of the observed laser pulse after a laser-plasma interaction in all cases where the laser propagates through regions with rapidly changing plasma densities. This has implications for using Doppler measurements to track the laser-plasma boundary, especially in the case of thicker targets (> 50 nm).

6.4 Conclusions

Experimental measurements of the laser-reflecting surface motion has shown accelerations of up to 0.6×10^{20} ms^{-2} during the interaction of high-intensity (2×10^{20} Wcm^{-2}) 50 fs pulses with nanometer-scale targets. An approximately linear dependence of acceleration on target thickness is observed, with thicker targets showing a reduced acceleration. The 392 nm and 1000 nm target interactions showed an increasing blue shift of the reflected pulse with time, indicating that the thermal plasma expansion dominated the radiation pressure of the laser.

The maximum observed surface recession velocity of 0.02 c would correspond to proton energies of 1.7 MeV if the acceleration was solely due to the hole-boring mechanism. This is considerably lower than observed in the experiment, demonstrating that hole-boring can only account for the lower energy portion of accelerated ion spectra. Therefore, an electrostatic sheath acceleration mechanism is most likely dominant in these interactions.

In 2D3V OSIRIS simulations, it was observed that targets that are initially 20 nm or thinner become transparent to the laser due to target expansion, whereas thicker targets survive the entire interaction. Thinner targets are also seen to be more easily 'pushed' by the target resulting in a redshift of the laser.

The presence of a large scale length pre-plasma, which was observed at later times in the interactions for the thicker targets, was seen to enhance the Doppler shift observed in the reflected laser pulse. This has the effect of exaggerating the surface velocity calculated from the reflected laser spectrum. This would have a significant effect on experimental observations of this type, especially for thick targets or for long (> 50 fs) pulse durations.

Chapter 7

Summary

In laser-plasma interactions the temporal, spectral and spatial characteristics of the laser pulse are critical to the nature of the interaction. Characterising the changes to the laser caused during the interaction can also be an invaluable diagnostic of the plasma conditions. The main work of this thesis has been the development of such diagnostics, and subsequent analysis of their use. This has resulted in an improved understanding of the interactions studied, as well as revealing methods by which a plasma can alter the driving laser in a way which is useful for further applications. The field of 'plasma optics' promises to provide methods of controlling electromagnetic radiation in ways that are not otherwise possible, and which may be required for further improvement of plasma based particle accelerators.

7.1 Evolution of the driving laser in a plasma accelerator

In order to generate high energy (> 1 GeV) electron beams from a laser-driven plasma-wakefield accelerator, it is necessary to have an acceleration length on the order of 1 cm. Although, this is very short compared to the length of a comparable conventional electron accelerator, it is much longer than the normal distance over which a focused laser diffracts. However, the work in this thesis has demonstrated that the laser can be well guided over 15 mm by the self-focusing effect of the plasma. This enabled acceleration of electrons to near-GeV energies, and also resulted in significant modification of the longitudinal properties of the laser pulse.

Temporal-spectral measurements of the transmitted laser pulse revealed a large red-shift at the leading edge after propagation through the plasma, due to photon-acceleration in the plasma-wakefield. Simultaneously, group velocity dispersion in the wakefield resulted in the temporal compression of the driving pulse, from an initial duration of 55 fs (FWHM) to 14($\pm$2) fs. Diagnostic limitations prevented measurements of shorter pulses, but simulations indicate that pulse durations as short as $\approx$ 6 fs may be generated.

Laser pulse depletion is a crucial factor in determining the length of the accelerating structure, and hence the maximum achievable electron energy. Transmitted energy measurements, as functions of plasma density and propagation length, gave the termination point of the acceleration process over this parameter space. Measuring the energy transmission, while varying the plasma density was seen to be equivalent to varying the propagation length, as the depletion rate was seen to scale equally with both. A good fit to a pulse-front etching model [Decker96] was observed with the assumption that the process starts where the laser power first exceeds $1/e$ of the peak value. However, a more physical description, using the critical power for self-focusing as the threshold value, significantly underestimated the pulse depletion. Potentially, including pulse compression in this model may result in a more accurate description of the data. In addition, PIC simulations have revealed that the pulse-front etching rates are dependent on the input pulse shape. A pulse with a gaussian power profile was seen to etch more rapidly than a numerical approximation to the measured Astra Gemini pulse profile. The Gemini pulse had a long slow rising edge, which may have acted to establish a guiding structure, subsequently reducing diffraction losses in the main pulse.

The peak power of the transmitted laser pulses, calculated from the energy and pulse shape measurements, demonstrated power amplification in a plasma for the first time. The peak power increased by $\approx$ 78%, from the input value of 180 TW to 320 TW, with a pulse length of $\approx$ 14 fs. This is far in excess of the peak powers available from conventional laser sources at this pulse length, and may provide a method of probing high energy plasmas, and laser-plasma interactions on a very short timescale, where self-emission or scattering of the driving pulse would prevent probing with a less energetic pulse.

PIC simulations have been shown to accurately reproduce the experimental measurements of pulse depletion and compression. They have also revealed how the plasma wakefield is affected as the driving laser pulse evolves. Rapid lengthening of the first period of the plasma wake was seen to result from the compression of the driving pulse. This increase enabled injection, due to the lowering of the phase velocity of the rear of the bubble, lowering the requirements for an electron to become trapped from $\gamma = 12$ to $\gamma = 5.5$. This only occurred over a short region, resulting in a narrow phase spread of the trapped electrons. This translates to a narrow energy spread of the final electron beam and offers a new explanation for the observation of quasi-monoenergetic electron beams from uniform density plasmas [Mangles04, Faure04, Geddes04]. A model based on this observation, and on the measured pulse depletion and compression rates, was used to estimate the acceleration length as function of nozzle diameter and electron density, and thereby predict the maximum electron energies achievable. Comparing these values to the experimentally observed maximum electron energies revealed a reasonable fit for the 10 mm nozzle but the maximum achieved energy for the 15 mm nozzle was somewhat less than predicted. This may be explained by estimates of the maximum guided pulse intensity, which indicated that a lower amplitude wakefield may have been driven towards the end of the 15 mm nozzle.

Red-shifting of the leading edge of the pulse was seen to continue to a point where the lowest frequency components slipped back into the ion cavity, due to group velocity dispersion. Enough energy was present at these wavelengths to significantly modify the trajectories of the electrons around the perimeter of the bubble, resulting in an oscillation within the bubble shape. This instability has a large effect on the injection processes at the back of the bubble, and the focusing electric fields within the ion cavity. This may significantly influence the properties of the accelerated bunch, such as increasing the amplitude of betatron oscillations, affecting the x-ray spectrum produced.

7.2 Surface dynamics of solid-density plasmas

The reflected laser beam, from interactions of ultra-intense ($a_0 > 10$) laser pulses with nanometer scale, solid-density plasmas, was characterised spectrally and temporally. This has revealed motion of the laser-reflecting surface, on time scales on the order of the pulse length, and oscillations at the frequency of the driving electric field.

The rapid oscillations resulted in surface harmonics being generated in the specular direction for oblique incidence and p-polarisation. The fundamental, and second harmonic reflected efficiencies were measured, showing that the total reflectivity only changed by $\approx 8\%$ over 5 orders of magnitude in laser intensity. This is indicative of a very high contrast interaction, as the plasma scale length (a major factor in determining laser absorption) remained relatively constant up to intensities in excess of 1×10^{20} Wcm^{-2}.

The second harmonic generation efficiency was seen to rise to a maximum of $22(\pm 8)\%$ for $I > 10^{20}$ Wcm^{-2}. This is comparable to that which can be achieved using a birefringent crystal (e.g. BBO), but does not suffer from beam degradation due to nonlinear optical effects, or pulse lengthening by group velocity dispersion. Therefore, this is a viable source of high intensity 400 nm short laser pulses. Calculations, based on a relativistically oscillating mirror model, were found to reproduce these results numerically, indicating that the laser-plasma surface oscillates like a forced harmonic oscillator at resonance. PIC simulations were used to visualise the electron density waves that propagate along the target surface, due to the driving field of the laser. The efficiency of harmonic generation, measured in the simulations, showed a general agreement with the relativistically oscillating mirror model, although numerical heating limited the intensity range over which the simulations were usable.

Motion of the laser-reflecting surface, averaged over the laser period, was measured by using the relativistic Doppler shift experienced by the driving laser pulse. This was achieved by using a FROG to measure the time-dependent frequency of the pulse, so that the target evolution could be observed, and the acceleration of the surface could be measured. The surface acceleration was seen to be dependent on target thickness, which was varied over 3.5–1000 nm. Thinner targets were observed to experience a more rapid acceleration away from the laser, than thicker targets. This is consistent with a thermal expansion of the plasma, resulting in a lower density for thinner targets, so that radiation pressure of the laser was able to bore into the plasma more easily.

The surface recession velocities of the targets were not consistent with 1D models of hole-boring or light sail acceleration. The ion energies measured from these interactions were far in excess of what could occur due to either of these mechanisms at the measured surface velocities. This indicates that the dominant mechanisms for the acceleration of ions in these experiments were electrostatically driven, such as sheath acceleration.

PIC simulations showed the same phenomenology as observed in the experiments, i.e. thicker targets expanded towards the laser, whereas thinner targets were pushed forwards by the radiation pressure as their density dropped. It was discovered that the underdense plasma in front of the laser-reflecting surface causes the phase velocity of the laser to vary with time and also leads to photon acceleration, due to the locally increasing electron density as the plasma expands. This modifies the time-dependent frequency of the reflected laser, such that the surface motion is not solely responsible from the frequency shifts of the laser. These effects need to be considered for all similar experiments, where a large amount of underdense front-surface plasma is generated. The simulations suggest that this is the case for target thicknesses above 50 nm, so results from thicker targets, and potentially longer pulse length interactions will be affected by underdense plasma dynamics.

7.3 Future work

The measurements of the pulse evolution in laser-driven wakefields has been shown to be very informative and could be extended to include other target types, such as longer plasmas, non-uniform density profiles and external guiding structures. The diagnostics themselves could be improved to provide an indication of how the pulse properties change spatially at the exit mode of the plasma. Also, extending the spectral range of these diagnostics, especially to long wavelengths, would provide a more complete picture of the photon acceleration and pulse shape modification of the wakefield. This could be particularly important in observing the far red-shifted components and the associated bubble instability that is seen in PIC simulations. 3D simulations would also enable a full comparison of the wakefield physics with experimental observations.

The two-FROG method for removing the time-direction ambiguity has been shown to work well, and could be used to retrieve the full pulse profiles beyond the density range observed in this thesis. Exploring the effect of pulse shape on pulse depletion and dephasing may help to increase the possible acceleration lengths, and maximum electron energies.

In order to determine the range of potential applications for the specularly reflected second harmonic beam from solid-density plasma surfaces, first the focusability must be tested. The pulses could then be used to probe plasmas to higher densities and overcome the background issues that occur when probing at the fundamental wavelength. The temporal properties of the SHG pulse could also be measured, perhaps by using a FROG, to determine how the surface oscillations change with time. This may also provide an indication of the changing plasma properties and scale-length during the interaction. In general the spectral reflectivity diagnostic is relatively simple, provides a large amount of information for solid target interactions, and could be easily used on many different experiments.

The Doppler measurements of reflecting surfaces could be performed over a wider range of laser and plasma conditions. Particularly, circular polarisation is of interest due to the suppression of target heating, therefore allowing the radiation pressure of the laser to dominate more easily. Combining this with target reflectivity/transmissivity diagnostics would give a more complete picture of the plasma evolution. Measuring the Doppler shift to a second beam, rather than the driving pulse, would allow measurement of the plasma evolution beyond the peak of the driving pulse. This could then build up a full picture of the laser-plasma interaction, and clearly show the influence of pre-pulses and the finite rise-time of the laser. Further work to study the photon acceleration effect is required to use this diagnostic reliably for thick targets. Perhaps, using two separate wavelengths to measure the frequency shifts upon reflection can be used to separate the Doppler shift and photon acceleration effects.

Appendix A

Appendix

A.1 Particle motion in an electromagnetic field

The motion of a charged particle in an electromagnetic field is given by the Lorentz force,

$$\frac{\mathrm{d}\mathbf{p}}{\mathrm{d}t} = q\left(\mathbf{E} + \mathbf{v} \times \mathbf{B}\right) \ .$$

Using the vector potential $\mathbf{A}$, defined by $\mathbf{E} = -\dfrac{\partial \mathbf{A}}{\partial t}$ and $\mathbf{B} = \nabla \times \mathbf{A}$, the motion of an electron in vacua is given by,

$$\frac{\mathrm{d}\mathbf{p}}{\mathrm{d}t} = e\left[\frac{\partial \mathbf{A}}{\partial t} - \mathbf{v} \times (\nabla \times \mathbf{A})\right] \ . \tag{A.1.1}$$

Using the vector identity,

$$\mathbf{v} \times (\nabla \times \mathbf{A}) = (\nabla \mathbf{A}) \cdot \mathbf{v} - (\mathbf{v} \cdot \nabla)\mathbf{A} \ ,$$

and the convective derivative $\left(\dfrac{\mathrm{d}}{\mathrm{d}t} = \dfrac{\partial}{\partial t} + \mathbf{v} \cdot \nabla\right)$, equation **A.1.1** becomes,

$$\frac{\mathrm{d}\mathbf{p}}{\mathrm{d}t} = e\left[\frac{\mathrm{d}\mathbf{A}}{\mathrm{d}t} - (\nabla \mathbf{A}) \cdot \mathbf{v}\right] \ . \tag{A.1.2}$$

Setting the vector potential as a infinite plane wave polarised in the $\mathbf{x}$ direction and propagating in the $\mathbf{z}$ direction allows equation **A.1.2** to be split into transverse and longitudinal terms,

$$\mathbf{p}_\perp = e\mathbf{A} \ , \tag{A.1.3}$$
$$\frac{\mathrm{d}\mathbf{p}_\parallel}{\mathrm{d}t} = -e(\nabla\mathbf{A}) \cdot \mathbf{v} \ . \tag{A.1.4}$$

Defining,

$$\mathbf{A} = A_0 \cos\phi \, \hat{\mathbf{i}} \ , \tag{A.1.5}$$

where $\phi = \omega_0 t - k_0 z$ and $\omega_0 = k_0 c$, we see that,

$$\frac{\partial\mathbf{A}}{\partial t} = -c\frac{\partial\mathbf{A}}{\partial z} \ . \tag{A.1.6}$$

Also equation **A.1.4** becomes,

$$\begin{aligned} \frac{\mathrm{d}\mathbf{p}_\parallel}{\mathrm{d}t} &= -e\mathbf{v}_\perp \cdot \frac{\partial\mathbf{A}}{\partial z}\,\hat{\mathbf{k}} \ , \\ \frac{\mathrm{d}\mathbf{p}_\parallel}{\mathrm{d}t} &= \frac{e}{c}\mathbf{v}_\perp \cdot \frac{\partial\mathbf{A}}{\partial t}\,\hat{\mathbf{k}} \ . \end{aligned} \tag{A.1.7}$$

Taking the dot product of $\mathbf{v}$ with equation **A.1.1** gives an expression for the particle energy.

$$\begin{aligned} \mathbf{v} \cdot \frac{\mathrm{d}\gamma m_e \mathbf{v}}{\mathrm{d}t} &= e\left[\mathbf{v} \cdot \frac{\partial\mathbf{A}}{\partial t} - \mathbf{v} \cdot (\mathbf{v} \times (\nabla \times \mathbf{A}))\right] \\ m_e c\frac{\mathrm{d}\gamma}{\mathrm{d}t} &= \frac{e}{c}\left[\mathbf{v}_\perp \cdot \frac{\partial\mathbf{A}}{\partial t}\right] \end{aligned} \tag{A.1.8}$$

Subtracting equation **A.1.8** from the magnitude of equation **A.1.7** gives

$$\begin{aligned} \frac{\mathrm{d}}{\mathrm{d}t}(p_\parallel - m_e c\gamma) &= 0, \\ p_\parallel &= m_e c(\gamma - \alpha) \end{aligned} \tag{A.1.9}$$

where α is the integration constant. The longitudinal momentum can also be expressed in terms of the perpendicular momentum by using ${m_e}^2c^2\gamma^2 = {m_e}^2c^2 + |\mathbf{p}_\perp|^2 + |p_\parallel|^2$ giving

$$\begin{aligned} p_\parallel &= \frac{|\mathbf{p}_\perp|^2 + {m_e}^2c^2\left(1-\alpha^2\right)}{2m_e c\alpha}, \\ p_\parallel &= \frac{m_e c(1 + a^2 - \alpha^2)}{2\alpha}, \end{aligned} \tag{A.1.10}$$

where

$$a = \frac{eA_0}{m_e c}\cos\phi. \tag{A.1.11}$$

γ is now given by

$$\gamma = \sqrt{1 + \frac{|\mathbf{p}_\perp|^2}{{m_e}^2c^2} + \frac{|\mathbf{p}_\parallel|^2}{{m_e}^2c^2}}$$

$$\gamma = \sqrt{\frac{2\alpha^2 + 2\alpha^2 a^2 + 1 + \alpha^4 + a^4 + 2a^2}{(2\alpha)^2}}$$

$$\gamma = \frac{a^2 + \alpha^2 + 1}{2\alpha} \tag{A.1.12}$$

So the velocity components are

$$v_\perp = \frac{p_\perp}{m\gamma}$$

$$v_\perp = \frac{2\alpha\, a\, c}{a^2 + \alpha^2 + 1} \tag{A.1.13}$$

$$v_\parallel = \frac{(1 + a^2 - \alpha^2)\, c}{a^2 + \alpha^2 + 1} \tag{A.1.14}$$

A.2 Relativistic self-focusing

The expansion of a defocusing laser pulse is determined by equation **2.1.13**. Differentiating twice with respect to z at $z = 0$ results in,

$$\frac{\partial^2 w}{\partial z^2} = \frac{4c^2}{{\omega_0}^2{\sigma_r}^3}\ . \tag{A.2.1}$$

For stable propagation of a pulse, with a spatial width of σ_r ($1/e^2$ intensity), then the focusing effect of the plasma has to balance equation **A.2.1**. For small θ, such that $\sin\theta \simeq \theta$,

$$\theta = \frac{\mathrm{d}w}{\mathrm{d}z} = \frac{\mathrm{d}v_\phi}{\mathrm{d}r}\Delta t\ . \tag{A.2.2}$$

Using $\mathrm{d}/\mathrm{d}z = c^{-1}\ \mathrm{d}/\mathrm{d}t$ leads to,

$$\frac{\mathrm{d}^2 w}{\mathrm{d}z^2} = \frac{1}{c}\frac{\mathrm{d}v_\phi}{\mathrm{d}r}\ ,$$

$$\frac{\mathrm{d}^2 w}{\mathrm{d}z^2} = \frac{\mathrm{d}}{\mathrm{d}r}\left(1 - \frac{n_e}{\gamma n_c}\right)^{-\frac{1}{2}}\ . \tag{A.2.3}$$

For $n_e \ll n_c$, $a_0 < 1$, and setting $n_e =$ constant, the binomial expansion can be used to give,

$$\frac{\mathrm{d}^2 w}{\mathrm{d}z^2} = -\frac{\mathrm{d}a^2}{\mathrm{d}r}\frac{n_e}{8n_c} \ . \tag{A.2.4}$$

Approximating $\mathrm{d}a^2/\mathrm{d}r \simeq -a_0^2/\sigma_r$ and equating to equation **A.2.1** gives,

$${a_0}^2{\sigma_r}^2 = \frac{32c^2}{{\omega_p}^2} \ . \tag{A.2.5}$$

This equates the power of the pulse (${a_0}^2{\sigma_r}^2$) to an expression dependent on the plasma density and is known as the critical power for relativistic self-focusing and is commonly expressed as,

$$P_{\mathrm{crit}} \simeq 17\frac{n_c}{n_e}\ [GW] \ , \tag{A.2.6}$$

with a laser spot size given by,

$$\sigma_r = \frac{4\sqrt{2}}{a_0}\frac{c}{\omega_p} \ . \tag{A.2.7}$$

A.3 Convergence testing of PIC simulations

The longitudinal spatial resolution effectively determines how well oscillations can be resolved during the interaction while the ratio of $\mathrm{d}t/\mathrm{d}x$ leads to numerical dispersion. For accurate simulation the laser pulse evolution in a plasma both of these parameters are important. Therefore, several 1D OSIRIS simulations were performed in order to determine the resolution requirements for adequately simulating the laser propagation over 15 mm of plasma. The major source of rapid oscillations is the laser frequency, so it is important to have many cells per wavelength to accurately describe it. Also any higher frequency terms, perhaps created by photon acceleration inside the plasma wave should also be well resolved. Simulations were run with both Δx and Δt varying in order to look for convergence at the limit of high resolution and $\Delta x = \Delta t$. The simulations were run for $n_e = 2.5 \times 10^{18}$ cm^{-3} and $a_0 = 3.5$. Figure **A.1** shows the laser spectrum as a function of propagation of an $a_0 = 3.5$ laser through 15 mm of plasma at $n_e = 2.5 \times 10^{18}$ Wcm^{-2}. Also shown are the laser spectra after exiting the plasma. The images show that the behaviour is almost identical up to 5 mm of plasma for all values of dx and dt used. However, after 5 mm the simulation for which d$x = 0.2$ and d$t = 0.1$ diverges from the others considerably, as the spectral fringes observed become blurred. Smaller differences between the simulations are more clearly seen in the plots of the laser spectra at the exit

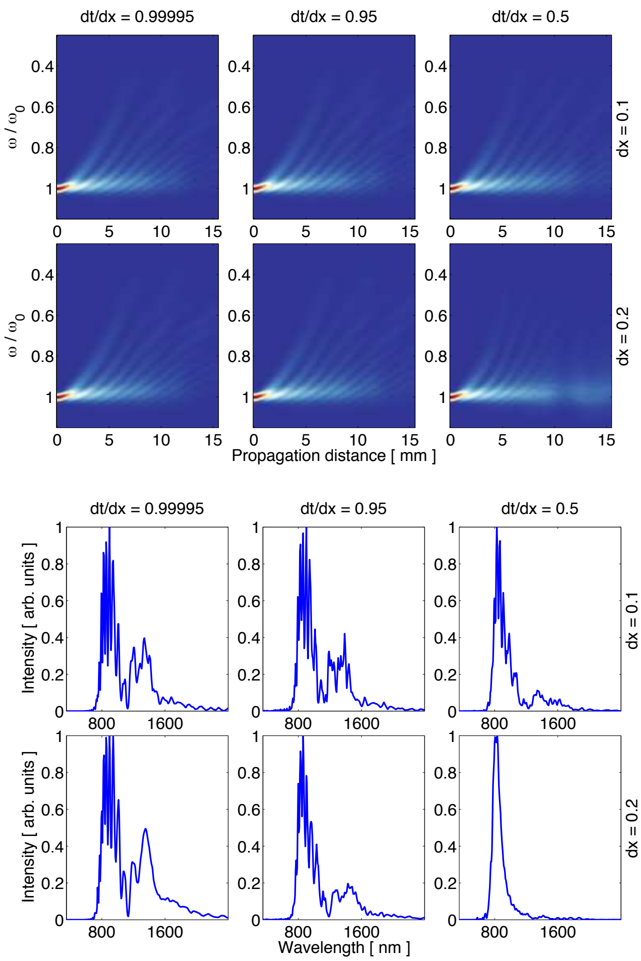

Figure A.1: Images of spectrum (vertical axis) against propagation distance (horizontal axis) in 1D OSIRIS simulations. For these simulations $\mathrm{d}x = 0.2\, c/\omega_0$.

of the plasma. It appears that the overall structure of the spectra are well represented for all simulations where $\mathrm{d}t/\mathrm{d}x > 0.95$ although the exact details vary. For the purpose of qualitative comparison with experiments $\mathrm{d}x = 0.2$ and $\mathrm{d}t = 0.1$ seems sufficient. A plot of relative error of the final laser spectra averaged over all simulations (figure **A.2**) indicates that the laser pulse error from these simulations will have an approximate error of 7%.

Another question remains over whether 1D simulations capture enough of the relevant processes to reproduce the longitudinal pulse modulation effects seen in experiments. In order to explore this, 1D and 2D simulations with otherwise identical parameters were performed with $\mathrm{d}x = 0.2$ and $\mathrm{d}t = 0.195$. The laser spectrum as a function of time and the plasma exit spectra are again plotted in figure **A.3**. Surprisingly, reasonable agree-

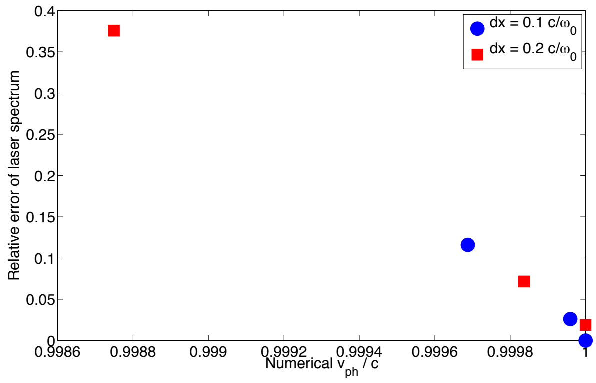

Figure A.2: Relative error of laser profiles for various values of dx and dt compared to the dx = dt = 0.2 c/ω_0 case.

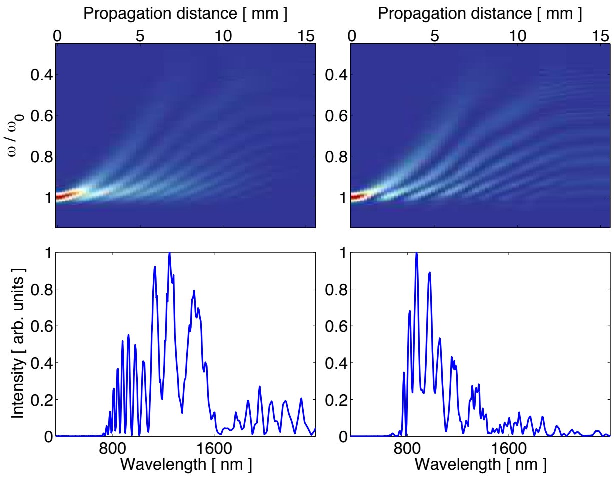

Figure A.3: Comparison of (Left) 1D and (Right) 2D simulations. For these simulations $dx = 0.2\,c/\omega_0$.

ment between the 1D and 2D simulations is observed. Both show significant red-shifting and generation of spectral fringes at a similar level showing that the majority of the longitudinal pulse modulation effects are well captured in a 1D simulations only. Obviously to observe self-guiding and diffraction losses of the pulse, 2D simulations are required and so these were performed in order to compare to the experimental data. However, a great deal of the phenomenology of the photon acceleration and pulse compression can be observed in 1D simulations.

Bibliography

[Agrawal01] G. Agrawal. *Nonlinear fiber optics.* Academic Press, San Diego, CA, third edition, 2001.

[Andreev92] N. Andreev, L. Gorbunov, and V. Kirsanov. *Resonant excitation of wakefields by a laser pulse in a plasma.* JETP lett, **55**:(1992), 571–576.

[ATLAS12] ATLAS. *Observation of a new particle in the search for the Standard Model Higgs boson with the ATLAS detector at the LHC.* Physics Letters B, **716**(1):(2012), 1–29.

[Augst89] S. Augst, D. Strickland, D. Meyerhofer, S. Chin, and J. Eberly. *Tunneling ionization of noble gases in a high-intensity laser field.* Physical Review Letters, **63**(20):(1989), 2212–2215.

[Baeva06] T. Baeva, S. Gordienko, and A. Pukhov. *Theory of high-order harmonic generation in relativistic laser interaction with overdense plasma.* Physical Review E, **74**(4):(2006), 46404.

[Bellei12] C. Bellei, J. R. Davies, P. K. Chauhan, and Z. Najmudin. *Coherent transition radiation in relativistic lasersolid interactions.* Plasma Physics and Controlled Fusion, **54**(3):(2012), 035011.

[Bin] J. Bin. *Personal communication.*

[Birdsall91] C. K. Birdsall and A. B. Langdon. *Plasma Physics via Computer Simulation.* Adam Hilger, Bristol, 1991.

[Brady11] C. S. Brady and T. D. Arber. *An ion acceleration mechanism in laser illuminated targets with internal electron density structure.* Plasma Physics and Controlled Fusion, **53**(1):(2011), 015001.

[Bulanov89] S. Bulanov, V. Kirsanov, and A. Sakharov. *Excitation of ultra-relativistic plasma waves by pulse of electromagnetic radiation.* JETP Lett, **50**(4):(1989), 198–201.

[Bulanov94] S. V. Bulanov, N. M. Naumova, and F. Pegoraro. *Interaction of an ultrashort, relativistically strong laser pulse with an overdense plasma.* Physics of Plasmas, **1**(3):(1994), 745.

[Butler02] A. Butler, D. Spence, and S. Hooker. *Guiding of High-Intensity Laser Pulses with a Hydrogen-Filled Capillary Discharge Waveguide.* Physical Review Letters, **89**(18):(2002), 185003.

[Carroll09] D. C. Carroll, D. Batani, R. G. Evans, Y. Glinec, C. Homann, R. Jafer, S. Kar, F. Lindau, O. Lundh, K. Markey, D. Neely, F. Nürnberg, A. Persson, M. N. Quinn, A. P. L. Robinson, M. Roth, C. G. Wahlström, X. Yuan, M. Zepf, and P. McKenna. *Dynamic control and enhancement of laser-accelerated protons using multiple laser pulses.* Comptes Rendus Physique, **10**(2-3):(2009), 188.

[Chen06] F. F. Chen. *Introduction to Plasma Physics and Controlled Fusion.* Springer, second edition, 2006.

[Clark00] E. L. Clark, K. Krushelnick, M. Zepf, F. N. Beg, M. Tatarakis, A. Machacek, M. I. K. Santala, I. Watts, P. A. Norreys, and A. E. Dangor. *Energetic Heavy-Ion and Proton Generation from Ultraintense Laser-Plasma Interactions with Solids.* Physical Review Letters, **85**(8):(2000), 1654–1657.

[Clayton93] C. E. Clayton, K. A. Marsh, A. Dyson, M. Everett, A. Lal, W. P. Leemans, R. Williams, and C. Joshi. *Ultrahigh-gradient acceleration of injected electrons by laser-excited relativistic electron plasma waves.* Physical Review Letters, **70**(1):(1993), 37–40.

[Clayton10] C. Clayton, J. Ralph, F. Albert, and R. Fonseca. *Self-guided laser wakefield acceleration beyond 1 GeV using ionization-induced injection.* Physical review letters, **056708**(2007).

[Corde13] S. Corde, K. Ta Phuoc, G. Lambert, R. Fitour, V. Malka, A. Rousse, A. Beck, and E. Lefebvre. *Femtosecond x rays from* *laser-plasma accelerators.* Reviews of Modern Physics, **85**(1):(2013), 1–48.

[Da Silva97] L. B. Da Silva, P. Celliers, G. W. Collins, K. S. Budil, N. C. Holmes, T. W. Barbee Jr., B. A. Hammel, J. D. Kilkenny, R. J. Wallace, M. Ross, and R. Cauble. *Absolute Equation of State Measurements on Shocked Liquid Deuterium up to 200 GPa (2 Mbar).* Physical Review Letters, **78**(3):(1997), 483–486.

[Davies09] J. R. Davies. *Laser absorption by overdense plasmas in the relativistic regime.* Plasma Physics and Controlled Fusion, **51**(1):(2009), 14006.

[Dawson59] J. Dawson. *Nonlinear Electron Oscillations in a Cold Plasma.* Physical Review, **113**(2):(1959), 383–387.

[Decker96] C. D. Decker, W. B. Mori, K.-C. Tzeng, and T. Katsouleas. *The evolution of ultra-intense, short-pulse lasers in underdense plasmas.* Physics of Plasmas, **3**(5):(1996), 2047.

[Dik08] J. Dik, K. Janssens, G. Van der Snickt, L. van der Loeff, K. Rickers, and M. Cotte. *Visualization of a lost painting by Vincent van Gogh using synchrotron radiation based X-ray fluorescence elemental mapping.* Analytical chemistry, **80**(16):(2008), 6436–42.

[Dromey06] B. Dromey, M. Zepf, A. Gopal, K. Lancaster, M. S. Wei, K. Krushelnick, M. Tatarakis, N. Vakakis, S. Moustaizis, R. Kodama, M. Tampo, C. Stoeckl, R. Clarke, H. Habara, D. Neely, S. Karsch, and P. Norreys. *High harmonic generation in the relativistic limit.* Nature Physics, **2**(7):(2006), 456–459.

[Elder47] F. Elder, A. Gurewitsch, R. Langmuir, and H. Pollock. *Radiation from Electrons in a Synchrotron.* Physical Review, **71**(11):(1947), 829–830.

[Esarey09] E. Esarey, C. Schroeder, and W. Leemans. *Physics of laser-driven plasma-based electron accelerators.* Reviews of Modern Physics, **81**(3):(2009), 1229–1285.

[Esirkepov04] T. Esirkepov, M. Borghesi, S. Bulanov, G. Mourou, and T. Tajima. *Highly Efficient Relativistic-Ion Generation in the Laser-Piston Regime.* Physical Review Letters, **92**(17):(2004), 175003.

[Everett94] M. Everett, A. Lal, D. Gordon, C. E. Clayton, K. A. Marsh, and C. Joshi. *Trapped electron acceleration by a laser-driven relativistic plasma wave*. Nature, **368**(6471):(1994), 527–529.

[Fang09] F. Fang, C. E. Clayton, K. A. Marsh, A. E. Pak, J. E. Ralph, N. C. Lopes, and C. Joshi. *Pump depletion limited evolution of the relativistic plasma wave-front in a forced laser-wakefield accelerator*. Plasma Physics and Controlled Fusion, **51**(2):(2009), 024003.

[Faure04] J. Faure, Y. Glinec, A. Pukhov, and S. Kiselev. *A laser-plasma accelerator producing monoenergetic electron beams*. Nature, **431**(September):(2004), 541–544.

[Faure05] J. Faure, Y. Glinec, J. Santos, F. Ewald, J.-P. Rousseau, S. Kiselev, A. Pukhov, T. Hosokai, and V. Malka. *Observation of Laser-Pulse Shortening in Nonlinear Plasma Waves*. Physical Review Letters, **95**(20):(2005), 205003.

[Fewster03] P. F. Fewster. *X-ray Scattering from Semiconductors*. Imperial College Press, London, 2nd edition, 2003.

[Fonseca02] R. A. Fonseca, L. O. Silva, F. S. Tsung, V. K. Decyk, W. Lu, C. Ren, W. B. Mori, S. Deng, S. Lee, T. Katsouleas, and J. C. Adam. *OSIRIS: A Three-Dimensional, Fully Relativistic Particle in Cell Code for Modeling Plasma Based Accelerators*. In P. Sloot, A. Hoekstra, C. Tan, and J. Dongarra (Editors) *Computational Science ICCS 2002 SE - 36*, volume 2331 of *Lecture Notes in Computer Science*, pages 342–351. Springer Berlin Heidelberg, 2002.

[Fuchs05] J. Fuchs, Y. Sentoku, S. Karsch, J. Cobble, P. Audebert, A. Kemp, A. Nikroo, P. Antici, E. Brambrink, A. Blazevic, E. Campbell, J. Fernández, J.-C. Gauthier, M. Geissel, M. Hegelich, H. Pépin, H. Popescu, N. Renard-LeGalloudec, M. Roth, J. Schreiber, R. Stephens, and T. Cowan. *Comparison of Laser Ion Acceleration from the Front and Rear Surfaces of Thin Foils*. Physical Review Letters, **94**(4):(2005), 045004.

[Geddes04] C. G. R. Geddes, C. S. Toth, J. Van Tilborg, E. Esarey, C. B. Schroeder, D. Bruhwiler, C. Nieter, J. Cary, and W. P. Leemans. *High-quality electron beams from a laser wakefield accelerator using plasma-channel guiding.* Nature, **431**(7008):(2004), 538–41.

[Geddes05] C. Geddes, C. Toth, J. van Tilborg, E. Esarey, C. Schroeder, J. Cary, and W. Leemans. *Guiding of Relativistic Laser Pulses by Preformed Plasma Channels.* Physical Review Letters, **95**(14):(2005), 145002.

[Geindre10] J. P. Geindre, R. S. Marjoribanks, and P. Audebert. *Electron Vacuum Acceleration in a Regime beyond Brunel Absorption.* Physical Review Letters, **104**(13):(2010), 135001.

[George09] H. George, F. Quéré, C. Thaury, G. Bonnaud, and P. Martin. *Mechanisms of forward laser harmonic emission from thin overdense plasmas.* New Journal of Physics, **11**(11):(2009), 113028.

[Gibbon96] P. Gibbon. *Harmonic Generation by Femtosecond Laser-Solid Interaction: A Coherent Water-Window Light Source?* Physical Review Letters, **76**(1):(1996), 50–53.

[Gibbon05a] P. Gibbon. *Resistively enhanced proton acceleration via high-intensity laser interactions with cold foil targets.* Physical Review E, **72**(2):(2005), 026411.

[Gibbon05b] P. Gibbon. *Short Pulse Interactions with Matter.* Imperial College Press, 2005.

[Giulietti89] A. Giulietti, D. Giulietti, D. Batani, V. Biancalana, L. Gizzi, L. Nocera, and E. Schifano. *Spectroscopic evidence for sum frequency of forward and backscattered light in laser plasmas.* Physical Review Letters, **63**(5):(1989), 524–527.

[Gold94] D. M. Gold. *Direct measurement of prepulse suppression by use of a plasma shutter.* Optics Letters, **19**(23):(1994), 2006.

[Gorbunov87] L. Gorbunov and V. Kirsanov. *Excitation of plasma waves by an electromagnetic wave packet.* Sov. Phys. JETP, **18**(October 1986):(1987), 290–294.

[Gordienko04] S. Gordienko, A. Pukhov, O. Shorokhov, and T. Baeva. *Relativistic Doppler Effect: Universal Spectra and Zeptosecond Pulses.* Physical Review Letters, **93**(11):(2004), 115002.

[Gordienko05] S. Gordienko and A. Pukhov. *Scalings for ultrarelativistic laser plasmas and quasimonoenergetic electrons.* Physics of Plasmas, **12**(4):(2005), 043109.

[Gordon03] D. Gordon, B. Hafizi, R. Hubbard, J. Peñano, P. Sprangle, and A. Ting. *Asymmetric Self-Phase Modulation and Compression of Short Laser Pulses in Plasma Channels.* Physical Review Letters, **90**(21):(2003), 215001.

[Haberberger11] D. Haberberger, S. Tochitsky, F. Fiuza, C. Gong, R. A. Fonseca, L. O. Silva, W. B. Mori, and C. Joshi. *Collisionless shocks in laser-produced plasma generate monoenergetic high-energy proton beams.* Nature Physics, **8**(1):(2011), 95–99.

[Haines09] M. Haines, M. Wei, F. Beg, and R. Stephens. *Hot-Electron Temperature and Laser-Light Absorption in Fast Ignition.* Physical Review Letters, **102**(4):(2009), 045008.

[Herrmann09] D. Herrmann, L. Veisz, R. Tautz, F. Tavella, K. Schmid, V. Pervak, and F. Krausz. *Generation of sub-three-cycle, 16 TW light pulses by using noncollinear optical parametric chirped-pulse amplification.* Optics Letters, **34**(16):(2009), 2459.

[Hidding06] B. Hidding, K. Amthor, B. Liesfeld, H. Schwoerer, S. Karsch, M. Geissler, L. Veisz, K. Schmid, J. Gallacher, S. Jamison, D. Jaroszynski, G. Pretzler, and R. Sauerbrey. *Generation of Quasimonoenergetic Electron Bunches with 80-fs Laser Pulses.* Physical Review Letters, **96**(10):(2006), 105004.

[Hooker06] C. J. J. Hooker, J. L. L. Collier, O. Chekhlov, R. Clarke, E. Divall, K. Ertel, B. Fell, P. Foster, S. Hancock, A. Langley, D. Neely, J. Smith, and B. Wyborn. *The Astra Gemini project - A dual-beam petawatt Ti:Sapphire laser system.* J. Phys. IV France, **133**:(2006), 673–677.

[Hörlein08] R. Hörlein, B. Dromey, D. Adams, Y. Nomura, S. Kar, K. Markey, P. Foster, D. Neely, F. Krausz, G. D. Tsakiris, and M. Zepf. *High contrast plasma mirror: spatial filtering and second harmonic generation at 10 19 W cm 2.* New Journal of Physics, **10**(8):(2008), 83002.

[Hörlein11] R. Hörlein, S. Steinke, A. Henig, S. G. Rykovanov, M. Schnürer, T. Sokollik, P. V. Nickles, M. Zepf, G. D. Tsakiris, W. Sandner, and D. Habs. *Dynamics of nanometer-scale foil targets irradiated with relativistically intense laser pulses.* Laser and Particle Beams, **29**(04):(2011), 383–388.

[Joshi84] C. Joshi, W. B. Mori, T. Katsouleas, J. M. Dawson, J. M. Kindel, and D. W. Forslund. *Ultrahigh gradient particle acceleration by intense laser-driven plasma density waves.* Nature, **311**(5986):(1984), 525–529.

[Kalmykov09] S. Kalmykov, S. Yi, V. Khudik, and G. Shvets. *Electron Self-Injection and Trapping into an Evolving Plasma Bubble.* Physical Review Letters, **103**(13):(2009), 135004.

[Kaluza04] M. Kaluza, J. Schreiber, M. I. K. Santala, G. D. Tsakiris, K. Eidmann, J. Meyer-ter Vehn, and K. J. Witte. *Influence of the Laser Prepulse on Proton Acceleration in Thin-Foil Experiments.* Physical Review Letters, **93**(4):(2004), 45003.

[Kane97] D. J. Kane, G. Rodriguez, A. J. Taylor, and T. S. Clement. *Simultaneous measurement of two ultrashort laser pulses from a single spectrogram in a single shot.* Journal of the Optical Society of America B, **14**(4):(1997), 935.

[Kane98] D. Kane. *Real-time measurement of ultrashort laser pulses using principal component generalized projections.* Selected Topics in Quantum Electronics, IEEE, **4**(2):(1998), 278–284.

[Kapteyn91] H. C. Kapteyn, M. M. Murnane, A. Szoke, and R. W. Falcone. *Prepulse energy suppression for high-energy ultrashort pulses using self-induced plasma shuttering.* Optics Letters, **16**(7):(1991), 490.

[Karsch07] S. Karsch, J. Osterhoff, A. Popp, T. P. Rowlands-Rees, Z. Major, M. Fuchs, B. Marx, R. Hörlein, K. Schmid, L. Veisz, S. Becker, U. Schramm, B. Hidding, G. Pretzler,

D. Habs, F. Grüner, F. Krausz, and S. M. Hooker. *GeV-scale electron acceleration in a gas-filled capillary discharge waveguide*. New Journal of Physics, **9**(11):(2007), 415–415.

[Katsouleas88] T. Katsouleas and W. B. Mori. *Wave-Breaking Amplitude of Relativistic Oscillations in a Thermal Plasma*. Physical Review Letters, **61**(1):(1988), 90–93.

[Kemp08] a. Kemp, Y. Sentoku, and M. Tabak. *Hot-Electron Energy Coupling in Ultraintense Laser-Matter Interaction*. Physical Review Letters, **101**(7):(2008), 8–11.

[Kingham01] R. Kingham, P. Gibbon, W. Theobald, L. Veisz, and R. Sauerbrey. *Phase Modulation of Intense Ultrashort Laser Pulses Reflected From Steep, Dense Plasmas*. Physical Review Letters, **86**(5):(2001), 810–813.

[Kneip08] S. Kneip, S. R. Nagel, C. Bellei, N. Bourgeois, A. E. Dangor, A. Gopal, R. Heathcote, S. P. D. Mangles, J. Marquès, A. Maksimchuk, P. M. Nilson, K. T. Phuoc, S. Reed, M. Tzoufras, F. S. Tsung, L. Willingale, W. B. Mori, A. Rousse, K. Krushelnick, and Z. Najmudin. *Observation of Synchrotron Radiation from Electrons Accelerated in a Petawatt-Laser-Generated Plasma Cavity*. Physical Review Letters, **100**(10):(2008), 105006.

[Kneip09] S. Kneip, S. R. Nagel, S. F. Martins, S. P. D. Mangles, C. Bellei, O. Chekhlov, R. J. Clarke, N. Delerue, E. J. Divall, G. Doucas, K. Ertel, F. Fiuza, R. Fonseca, P. Foster, S. J. Hawkes, C. J. Hooker, K. Krushelnick, W. B. Mori, C. A. J. Palmer, K. T. Phuoc, P. P. Rajeev, J. Schreiber, M. J. V. Streeter, D. Urner, J. Vieira, L. O. Silva, and Z. Najmudin. *Near-GeV Acceleration of Electrons by a Nonlinear Plasma Wave Driven by a Self-Guided Laser Pulse*. Physical Review Letters, **103**(3):(2009), 035002.

[Kneip10] S. Kneip. *Laser Plamsa Accelerator and Wiggler*. Ph.D. thesis, Imperial College London, 2010.

[Koenig95] M. Koenig, B. Faral, J. Boudenne, D. Batani, A. Benuzzi, S. Bossi, C. Rémond, J. Perrine, M. Temporal, and

S. Atzeni. *Relative Consistency of Equations of State by Laser Driven Shock Waves.* Physical Review Letters, **74**(12):(1995), 2260–2263.

[Kostyukov04] I. Kostyukov, A. Pukhov, and S. Kiselev. *Phenomenological theory of laser-plasma interaction in bubble regime.* Physics of Plasmas, **11**(11):(2004), 5256.

[Kostyukov09] I. Kostyukov and E. Nerush. *Electron Self-Injection in Multidimensional Relativistic-Plasma Wake Fields.* Physical Review Letters, **103**(17):(2009), 175003.

[Kramida11] A. Kramida, Y. Ralchenko, J. Reader, Team, and N. ASD. *NIST Atomic Spectra Database*, 2011.

[Kruer88] W. L. Kruer. *The Physics of laser plasma interactions.* New York: Addison Wesley, 1988.

[Landau75] L. D. Landau and E. M. Lifshits. *The classical theory of fields.* Butterworth-Heinemann, vol. 2 edition, 1975.

[Levin05] W. P. Levin, H. Kooy, J. S. Loeffler, and T. F. DeLaney. *Proton beam therapy.* British journal of cancer, **93**(8):(2005), 849–54.

[Lichters96] R. Lichters, J. Meyer-ter Vehn, and A. Pukhov. *Short-pulse laser harmonics from oscillating plasma surfaces driven at relativistic intensity.* Physics of Plasmas, **3**(9):(1996), 3425–3437.

[Linde95] D. von der Linde, T. Engers, G. Jenke, P. Agostini, G. Grillon, E. Nibbering, A. Mysyrowicz, and A. Antonetti. *Generation of high-order harmonics from solid surfaces by intense femtosecond laser pulses.* Physical Review A, **52**(1):(1995), R25–R27.

[Linde96] D. von der Linde and K. Rzàzewski. *High-order optical harmonic generation from solid surfaces.* Applied Physics B: Lasers and Optics, **63**(5):(1996), 499–506.

[Lu06] W. Lu, C. Huang, M. Zhou, M. Tzoufras, F. S. Tsung, W. B. Mori, and T. Katsouleas. *A nonlinear theory for multidimensional relativistic plasma wave wakefields.* Physics of Plasmas, **13**(5):(2006), 056709.

[Lu07] W. Lu, M. Tzoufras, C. Joshi, F. Tsung, W. Mori, J. Vieira, R. Fonseca, and L. Silva. *Generating multi-GeV electron bunches using single stage laser wakefield acceleration in a 3D nonlinear regime*. Physical Review Special Topics - Accelerators and Beams, **10**(6):(2007), 1–12.

[Lu11] H. Lu, M. Liu, W. Wang, C. Wang, J. Liu, A. Deng, J. Xu, C. Xia, W. Li, H. Zhang, X. Lu, J. Wang, X. Liang, Y. Leng, B. Shen, K. Nakajima, R. Li, and Z. Xu. *Laser wakefield acceleration of electron beams beyond 1 GeV from an ablative capillary discharge waveguide*. Applied Physics Letters, **99**(9):(2011), 091502.

[Ma11] W. Ma, V. Liechtenstein, J. Szerypo, D. Jung, P. Hilz, B. Hegelich, H. Maier, J. Schreiber, and D. Habs. *Preparation of self-supporting diamond-like carbon nanofoils with thickness less than 5nm for laser-driven ion acceleration*. Nuclear Instruments and Methods in Physics Research Section A: Accelerators, Spectrometers, Detectors and Associated Equipment, **655**(1):(2011), 53–56.

[Macchi05] A. Macchi, F. Cattani, T. Liseykina, and F. Cornolti. *Laser Acceleration of Ion Bunches at the Front Surface of Overdense Plasmas*. Physical Review Letters, **94**(16):(2005), 165003.

[Mackinnon01] A. J. Mackinnon, M. Borghesi, S. Hatchett, M. H. Key, P. K. Patel, H. Campbell, A. Schiavi, R. Snavely, S. C. Wilks, and O. Willi. *Effect of Plasma Scale Length on Multi-MeV Proton Production by Intense Laser Pulses*. Physical Review Letters, **86**(9):(2001), 1769.

[Mangles04] S. P. D. Mangles, C. D. Murphy, Z. Najmudin, A. G. R. Thomas, J. L. Collier, A. E. Dangor, E. J. Divall, P. S. Foster, J. G. Gallacher, C. J. Hooker, D. A. Jaroszynski, A. J. Langley, W. B. Mori, P. A. Norreys, F. S. Tsung, R. Viskup, B. R. Walton, and K. Krushelnick. *Monoenergetic beams of relativistic electrons from intense laser-plasma interactions*. Nature, **431**(7008):(2004), 535–538.

[Marcinkevicius04] A. Marcinkevicius, R. Tommasini, G. D. Tsakiris, K. J. Witte, E. Gaizauskas, and U. Teubner. *Frequency doubling* *of multi-terawatt femtosecond pulses.* Applied Physics B: Lasers and Optics, **79**(5):(2004), 547–554.

[Marx66] G. Marx. *Interstellar Vehicle Propelled By Terrestrial Laser Beam.* Nature, **211**(5044):(1966), 22–23.

[Mironov09] S. Mironov, V. Lozhkarev, V. Ginzburg, and E. Khazanov. *High-efficiency second-harmonic generation of superintense ultrashort laser pulses.* Appl. Opt., **48**(11):(2009), 2051–2057.

[Modena95] A. Modena, Z. Najmudin, A. E. Dangor, C. E. Clayton, K. A. Marsh, C. Joshi, V. Malka, C. B. Darrow, C. Danson, D. Neely, and F. N. Walsh. *Electron acceleration from the breaking of relativistic plasma waves.* Nature, **377**(6550):(1995), 606–608.

[Momose96] A. Momose, T. Takeda, Y. Itai, and K. Hirano. *Phasecontrast Xray computed tomography for observing biological soft tissues.* Nature Medicine, **2**(4):(1996), 473–475.

[Mora03] P. Mora. *Plasma Expansion into a Vacuum.* Physical Review Letters, **90**(18):(2003), 185002.

[Murphy06] C. D. Murphy, R. Trines, J. Vieira, A. J. W. Reitsma, R. Bingham, J. L. Collier, E. J. Divall, P. S. Foster, C. J. Hooker, A. J. Langley, P. A. Norreys, R. A. Fonseca, F. Fiuza, L. O. Silva, J. T. Mendonca, W. B. Mori, J. G. Gallacher, R. Viskup, D. A. Jaroszynski, S. P. D. Mangles, A. G. R. Thomas, K. Krushelnick, and Z. Najmudin. *Evidence of photon acceleration by laser wake fields.* Physics of Plasmas, **13**(3):(2006), 33108.

[Neutze00] R. Neutze, R. Wouts, D. van der Spoel, E. Weckert, and J. Hajdu. *Potential for biomolecular imaging with femtosecond X-ray pulses.* Nature, **406**(6797):(2000), 752–7.

[Norreys96] P. Norreys, M. Zepf, S. Moustaizis, A. Fews, J. Zhang, P. Lee, M. Bakarezos, C. Danson, A. Dyson, P. Gibbon, P. Loukakos, D. Neely, F. Walsh, J. Wark, and A. Dangor. *Efficient Extreme UV Harmonics Generated from Picosecond Laser Pulse Interactions with Solid Targets.* Physical Review Letters, **76**(11):(1996), 1832–1835.

[Osterhoff08] J. Osterhoff, A. Popp, Z. Major, B. Marx, T. Rowlands-Rees, M. Fuchs, M. Geissler, R. Hörlein, B. Hidding, S. Becker, E. Peralta, U. Schramm, F. Grüner, D. Habs, F. Krausz, S. Hooker, and S. Karsch. *Generation of Stable, Low-Divergence Electron Beams by Laser-Wakefield Acceleration in a Steady-State-Flow Gas Cell*. Physical Review Letters, **101**(8):(2008), 085002.

[Palmer11] C. A. J. Palmer, N. P. Dover, I. Pogorelsky, M. Babzien, G. I. Dudnikova, M. Ispiriyan, M. N. Polyanskiy, J. Schreiber, P. Shkolnikov, V. Yakimenko, and Z. Najmudin. *Monoenergetic Proton Beams Accelerated by a Radiation Pressure Driven Shock*. Physical Review Letters, **106**(1):(2011), 014801.

[Ping08] Y. Ping, R. Shepherd, B. Lasinski, M. Tabak, H. Chen, H. Chung, K. Fournier, S. Hansen, A. Kemp, D. Liedahl, K. Widmann, S. Wilks, W. Rozmus, and M. Sherlock. *Absorption of Short Laser Pulses on Solid Targets in the Ultrarelativistic Regime*. Physical Review Letters, **100**(8):(2008), 085004.

[Ping12] Y. Ping, A. J. Kemp, L. Divol, M. H. Key, P. K. Patel, K. U. Akli, F. N. Beg, S. Chawla, C. D. Chen, R. R. Freeman, D. Hey, D. P. Higginson, L. C. Jarrott, G. E. Kemp, A. Link, H. S. McLean, H. Sawada, R. B. Stephens, D. Turnbull, B. Westover, and S. C. Wilks. *Dynamics of Relativistic Laser-Plasma Interaction on Solid Targets*. Physical Review Letters, **109**(14):(2012), 145006.

[Pirozhkov09] A. S. Pirozhkov, I. W. Choi, J. H. Sung, S. K. Lee, T. J. Yu, T. M. Jeong, I. J. Kim, N. Hafz, C. M. Kim, K. H. Pae, Y.-C. Noh, D.-K. Ko, J. Lee, A. P. L. Robinson, P. Foster, S. Hawkes, M. Streeter, C. Spindloe, P. McKenna, D. C. Carroll, C.-G. Wahlstrom, M. Zepf, D. Adams, B. Dromey, K. Markey, S. Kar, Y. T. Li, M. H. Xu, H. Nagatomo, M. Mori, A. Yogo, H. Kiriyama, K. Ogura, A. Sagisaka, S. Orimo, M. Nishiuchi, H. Sugiyama, T. Z. Esirkepov, H. Okada, S. Kondo, S. Kanazawa, Y. Nakai, A. Akutsu, T. Motomura, M. Tanoue, T. Shimomura, M. Ikegami,

I. Daito, M. Kando, T. Kameshima, P. Bolton, S. V. Bulanov, H. Daido, and D. Neely. *Diagnostic of laser contrast using target reflectivity.* Applied Physics Letters, **94**(24):(2009), 241102.

[Plaja98] L. Plaja, L. Roso, K. Rzazewski, and M. Lewenstein. *Generation of attosecond pulse trains during the reflection of a very intense laser on a solid surface.* J. Opt. Soc. Am. B, **15**(7):(1998), 1904–1911.

[Pukhov02] A. Pukhov and J. Meyer-ter Vehn. *Laser wake field acceleration: the highly non-linear broken-wave regime.* Applied Physics B: Lasers and Optics, **74**(4-5):(2002), 355–361.

[Pukhov08] A. Pukhov. *Control of laser-wakefield acceleration by the plasma-density profile.* Physical Review E, **77**(2):(2008), 025401.

[Quéré06] F. Quéré, C. Thaury, P. Monot, S. Dobosz, P. Martin, J.-P. Geindre, and P. Audebert. *Coherent Wake Emission of High-Order Harmonics from Overdense Plasmas.* Physical Review Letters, **96**(12):(2006), 125004.

[Quesnel98] B. Quesnel and P. Mora. *Theory and simulation of the interaction of ultraintense laser pulses with electrons in vacuum.* Physical Review E, **58**(3):(1998), 3719–3732.

[Robinson08] a. P. L. Robinson, M. Zepf, S. Kar, R. G. Evans, and C. Bellei. *Radiation pressure acceleration of thin foils with circularly polarized laser pulses.* New Journal of Physics, **10**(1):(2008), 013021.

[Robinson09] a. P. L. Robinson, P. Gibbon, M. Zepf, S. Kar, R. G. Evans, and C. Bellei. *Relativistically correct hole-boring and ion acceleration by circularly polarized laser pulses.* Plasma Physics and Controlled Fusion, **51**(2):(2009), 024004.

[Rödel12] C. Rödel, D. an der Brügge, J. Bierbach, M. Yeung, T. Hahn, B. Dromey, S. Herzer, S. Fuchs, A. G. Pour, E. Eckner, M. Behmke, M. Cerchez, O. Jäckel, D. Hemmers, T. Toncian, M. C. Kaluza, A. Belyanin, G. Pretzler, O. Willi, A. Pukhov, M. Zepf, and G. G. Paulus. *Harmonic Generation from Relativistic Plasma Surfaces in Ultrasteep Plasma Density Gradients.* Physical Review Letters, **109**(12):(2012), 125002.

[Rousse04] A. Rousse, K. Phuoc, R. Shah, A. Pukhov, E. Lefebvre, V. Malka, S. Kiselev, F. Burgy, J.-P. Rousseau, D. Umstadter, and D. Hulin. *Production of a keV X-Ray Beam from Synchrotron Radiation in Relativistic Laser-Plasma Interaction.* Physical Review Letters, **93**(13):(2004), 135005.

[Rowlands-Rees08] T. P. Rowlands-Rees, C. Kamperidis, S. Kneip, A. J. Gonsalves, S. P. D. Mangles, J. G. Gallacher, E. Brunetti, T. Ibbotson, C. D. Murphy, P. S. Foster, M. J. V. Streeter, F. Budde, P. A. Norreys, D. A. Jaroszynski, K. Krushelnick, Z. Najmudin, and S. M. Hooker. *Laser-driven acceleration of electrons in a partially ionized plasma channel.* Physical Review Letters, **100**(10):(2008), 105005.

[Rutherford11] E. Rutherford. *The Scattering of α and β Particles by Matter and the Structure of the Atom.* Phil. Mag, **495**(1909):(1911), 1–24.

[Santala00] M. I. K. Santala, M. Zepf, I. Watts, F. N. Beg, E. Clark, M. Tatarakis, K. Krushelnick, A. E. Dangor, T. McCanny, I. Spencer, R. P. Singhal, K. W. D. Ledingham, S. C. Wilks, A. C. Machacek, J. S. Wark, R. Allott, R. J. Clarke, and P. A. Norreys. *Effect of the Plasma Density Scale Length on the Direction of Fast Electrons in Relativistic Laser-Solid Interactions.* Physical Review Letters, **84**(7):(2000), 1459.

[Sauerbrey96] R. Sauerbrey. *Acceleration in femtosecond laser-produced plasmas.* Physics of Plasmas, **3**(12):(1996), 4712.

[Schreiber10] J. Schreiber, C. Bellei, S. P. D. Mangles, C. Kamperidis, S. Kneip, S. R. Nagel, C. A. J. Palmer, P. P. Rajeev, M. J. V. Streeter, and Z. Najmudin. *Complete Temporal Characterization of Asymmetric Pulse Compression in a Laser Wakefield.* Physical Review Letters, **105**(23):(2010), 235003.

[Schroeder04] C. Schroeder, E. Esarey, J. van Tilborg, and W. Leemans. *Theory of coherent transition radiation generated at a plasma-vacuum interface.* Physical Review E, **69**(1):(2004), 016501.

[Shadwick09] B. Shadwick and C. Schroeder. *Nonlinear laser energy depletion in laser-plasma accelerators.* Physics of Plasmas, **056704**(2009).

[Sheng05] Z.-M. Sheng, K. Mima, J. Zhang, and H. Sanuki. *Emission of Electromagnetic Pulses from Laser Wakefields through Linear Mode Conversion.* Physical Review Letters, **94**(9):(2005), 095003.

[Siegman86] A. E. Siegman. *Lasers.* University Science Books, 1986.

[Silva04] L. O. Silva, M. Marti, J. R. Davies, and R. A. Fonseca. *Proton Shock Acceleration in Laser-Plasma Interactions.* Physical Review Letters, **92**(1):(2004), 015002.

[Snavely00] R. Snavely, M. Key, S. Hatchett, T. Cowan, M. Roth, T. Phillips, M. Stoyer, E. Henry, T. Sangster, M. Singh, S. Wilks, A. MacKinnon, A. Offenberger, D. Pennington, K. Yasuike, A. Langdon, B. Lasinski, J. Johnson, M. Perry, and E. Campbell. *Intense High-Energy Proton Beams from Petawatt-Laser Irradiation of Solids.* Physical Review Letters, **85**(14):(2000), 2945–2948.

[Spindloe07] C. Spindloe and H. F. Lowe. *White light interferometric profiling of ultra-thin foil high power laser targets.* Technical report, Central Laser Facility, 2007.

[Sprangle88] P. Sprangle, E. Esarey, A. Ting, and G. Joyce. *Laser wakefield acceleration and relativistic optical guiding.* Applied Physics Letters, **53**(22):(1988), 2146.

[Sprangle90] P. Sprangle, E. Esarey, and A. Ting. *Nonlinear interaction of intense laser pulses in plasmas.* Physical Review A, **41**(8):(1990), 4463–4469.

[Sprangle92] P. Sprangle, E. Esarey, J. Krall, and G. Joyce. *Propagation and guiding of intense laser pulses in plasmas.* Physical Review Letters, **69**(15):(1992), 2200–2203.

[Strickland85] D. Strickland and G. Mourou. *Compression of amplified chirped optical pulses.* Optics Communications, **55**(6):(1985), 447–449.

[Sun87] G.-Z. Sun, E. Ott, Y. C. Lee, and P. Guzdar. *Self-focusing of short intense pulses in plasmas.* Physics of Fluids, **30**(2):(1987), 526.

[Tajima79] T. Tajima and J. Dawson. *Laser electron accelerator.* Physical Review Letters, **43**(4):(1979), 267–270.

[Tarasevitch00] A. Tarasevitch, A. Orisch, D. von der Linde, P. Balcou, G. Rey, J.-P. Chambaret, U. Teubner, D. Klöpfel, and W. Theobald. *Generation of high-order spatially coherent harmonics from solid targets by femtosecond laser pulses.* Physical Review A, **62**(2):(2000), 023816.

[Tarasevitch07] A. Tarasevitch, K. Lobov, C. Wünsche, and D. von der Linde. *Transition to the Relativistic Regime in High Order Harmonic Generation.* Physical Review Letters, **98**(10):(2007), 103902.

[Teychenne94] D. Teychenne, G. Bonnaud, and J.-L. Bobin. *Electrostatic and kinetic energies in the wake wave of a short laser pulse.* Physics of Plasmas, **1**(6):(1994), 1771.

[Thomas07] A. G. Thomas, Z. Najmudin, S. P. Mangles, C. D. Murphy, A. E. Dangor, C. Kamperidis, K. L. Lancaster, W. B. Mori, P. A. Norreys, W. Rozmus, and K. Krushelnick. *Effect of laser-focusing conditions on propagation and monoenergetic electron production in laser-wakefield accelerators.* Physical Review Letters, **98**(9):(2007), 95004.

[Thomas10] A. G. R. Thomas. *Scalings for radiation from plasma bubbles.* Physics of Plasmas, **17**(5):(2010), 056708.

[Trebino00] R. Trebino. *Frequency-Resolved Optical Gating: The Measurement of Ultrashort Laser Pulses.* Springer US, Boston, MA, 2000.

[Wei04] M. S. Wei, S. P. D. Mangles, Z. Najmudin, B. Walton, A. Gopal, M. Tatarakis, A. E. Dangor, E. L. Clark, R. G. Evans, S. Fritzler, R. J. Clarke, C. Hernandez-Gomez, D. Neely, W. Mori, M. Tzoufras, and K. Krushelnick. *Ion acceleration by collisionless shocks in high-intensity-laser-underdense-plasma interaction.* Physical Review Letters, **93**(15):(2004), 155003.

[Weng12] S. M. Weng, P. Mulser, and Z. M. Sheng. *Relativistic critical density increase and relaxation and high-power pulse propagation.* Physics of Plasmas, **19**(2):(2012), 022705.

[Wigner32] E. Wigner. *On the Quantum Correction For Thermodynamic Equilibrium.* Physical Review, **40**(5):(1932), 749–759.

[Wilks89] S. Wilks, J. Dawson, W. Mori, T. Katsouleas, and M. Jones. *Photon accelerator.* Physical Review Letters, **62**(22):(1989), 2600–2603.

[Wilks92] S. Wilks, W. Kruer, M. Tabak, and A. Langdon. *Absorption of ultra-intense laser pulses.* Physical Review Letters, **69**(9):(1992), 1383–1386.

[Wilks01] S. C. Wilks, A. B. Langdon, T. E. Cowan, M. Roth, M. Singh, S. Hatchett, M. H. Key, D. Pennington, A. MacKinnon, and R. A. Snavely. *Energetic proton generation in ultra-intense lasersolid interactions.* Physics of Plasmas, **8**(2):(2001), 542.

[Zepf98] M. Zepf, G. D. Tsakiris, G. Pretzler, I. Watts, D. M. Chambers, P. A. Norreys, U. Andiel, A. E. Dangor, K. Eidmann, C. Gahn, A. Machacek, J. S. Wark, and K. Witte. *Role of the plasma scale length in the harmonic generation from solid targets.* Physical Review E, **58**(5):(1998), R5253.

[Zheng03] J. Zheng, K. A. Tanaka, T. Miyakoshi, Y. Kitagawa, R. Kodama, T. Kurahashi, and T. Yamanaka. *Theoretical study of transition radiation from hot electrons generated in the lasersolid interaction.* Physics of Plasmas, **10**(7):(2003), 2994.

[Ziener03] C. Ziener, P. S. Foster, E. J. Divall, C. J. Hooker, M. H. R. Hutchinson, A. J. Langley, and D. Neely. *Specular reflectivity of plasma mirrors as a function of intensity, pulse duration, and angle of incidence.* Journal of Applied Physics, **93**(1):(2003), 768–770.

[Zigler96] A. Zigler, Y. Ehrlich, C. Cohen, J. Krall, and P. Sprangle. *Optical guiding of high-intensity laser pulses in a long plasma channel formed by a slow capillary discharge.* Journal of the Optical Society of America B, **13**(1):(1996), 68.